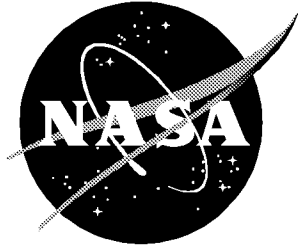


NASA/CR-1999-209556



Development, Analysis and Testing of the High Speed Research Flexible Semispan Model

*David M. Schuster, Charles V. Spain, David L. Turnock, Russ D. Rausch, M-Nabil Hamouda,
William A. Vogler, and Alan E. Stockwell
Lockheed Martin Engineering and Sciences Company, Hampton, Virginia*

September 1999

The NASA STI Program Office . . . in Profile

Since its founding, NASA has been dedicated to the advancement of aeronautics and space science. The NASA Scientific and Technical Information (STI) Program Office plays a key part in helping NASA maintain this important role.

The NASA STI Program Office is operated by Langley Research Center, the lead center for NASA's scientific and technical information. The NASA STI Program Office provides access to the NASA STI Database, the largest collection of aeronautical and space science STI in the world. The Program Office is also NASA's institutional mechanism for disseminating the results of its research and development activities. These results are published by NASA in the NASA STI Report Series, which includes the following report types:

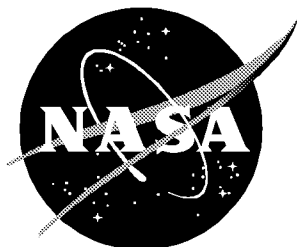
- **TECHNICAL PUBLICATION.** Reports of completed research or a major significant phase of research that present the results of NASA programs and include extensive data or theoretical analysis. Includes compilations of significant scientific and technical data and information deemed to be of continuing reference value. NASA counterpart or peer-reviewed formal professional papers, but having less stringent limitations on manuscript length and extent of graphic presentations.
- **TECHNICAL MEMORANDUM.** Scientific and technical findings that are preliminary or of specialized interest, e.g., quick release reports, working papers, and bibliographies that contain minimal annotation. Does not contain extensive analysis.
- **CONTRACTOR REPORT.** Scientific and technical findings by NASA-sponsored contractors and grantees.
- **CONFERENCE PUBLICATION.** Collected papers from scientific and technical conferences, symposia, seminars, or other meetings sponsored or co-sponsored by NASA.
- **SPECIAL PUBLICATION.** Scientific, technical, or historical information from NASA programs, projects, and missions, often concerned with subjects having substantial public interest.
- **TECHNICAL TRANSLATION.** English-language translations of foreign scientific and technical material pertinent to NASA's mission.

Specialized services that complement the STI Program Office's diverse offerings include creating custom thesauri, building customized databases, organizing and publishing research results . . . even providing videos.

For more information about the NASA STI Program Office, see the following:

- Access the NASA STI Program Home Page at <http://www.sti.nasa.gov>
- Email your question via the Internet to help@sti.nasa.gov
- Fax your question to the NASA STI Help Desk at (301) 621-0134
- Telephone the NASA STI Help Desk at (301) 621-0390
- Write to:
NASA STI Help Desk
NASA Center for AeroSpace Information
7121 Standard Drive
Hanover, MD 21076-1320

NASA/CR-1999-209556



Development, Analysis and Testing of the High Speed Research Flexible Semispan Model

*David M. Schuster, Charles V. Spain, David L. Turnock, Russ D. Rausch, M-Nabil Hamouda,
William A. Vogler, and Alan E. Stockwell
Lockheed Martin Engineering and Sciences Company, Hampton, Virginia*

National Aeronautics and
Space Administration

Langley Research Center
Hampton, Virginia 23681-2199

Prepared for Langley Research Center
under Contract NAS1-96014

September 1999

Available from:

NASA Center for AeroSpace Information (CASI)
7121 Standard Drive
Hanover, MD 21076-1320
(301) 621-0390

National Technical Information Service (NTIS)
5285 Port Royal Road
Springfield, VA 22161-2171
(703) 605-6000

TABLE OF CONTENTS

1.0	INTRODUCTION	1-1
2.0	HSR-FSM WIND TUNNEL MODEL	2-1
2.1	Aeroelastic Scaling	2-1
2.2	Model Description	2-1
2.2.1	Wing Model and Instrumentation	2-3
2.3	Fuselage Model and Instrumentation.....	2-5
3.0	FINITE ELEMENT MODELING	3-1
3.1	Chronology of FEM Development	3-1
3.2	Baseline FEM Development and Dynamic Analysis.....	3-4
3.3	FEM Refinement and Mass Tuning.....	3-8
3.3.1	Modeling Issues	3-8
3.3.2	Mass Properties	3-11
3.3.3	Dynamic Characteristics	3-15
3.4	Final Flutter Configuration FEM Development.	3-17
4.0	GROUND VIBRATION TESTING	4-1
4.1	Instrumentation and data acquisition	4-2
4.2	Test Procedure	4-4
4.3	Results and Comparison with Analysis	4-4
4.4	Test and Analysis.....	4-6
4.5	GVT Summary.....	4-8
5.0	MAXIMUM AERODYNAMIC LOAD ESTIMATION	5-1
5.1	Aerodynamic Load Transfer Strategy.....	5-2
5.2	Load Transfer Methodology	5-3
5.3	Application to the HSR-FSM	5-5
6.0	STATIC LOADS TEST	6-1
6.1	Stiffness Nonlinearity and FEM Tuning.....	6-4
6.2	Point Loads Test	6-5
6.3	Torsion Loads Test	6-8
6.4	Distributed Loads Test.....	6-10
7.0	FLUTTER ANALYSIS	7-1
7.1	Aeroelastic Models	7-1
7.2	Pretest Analysis.....	7-2
7.3	Post-test Analysis.....	7-3
7.4	Flutter Analysis Summary	7-5
8.0	WIND TUNNEL TESTING ON LOADS BALANCE	8-1
8.1	Test Conditions and Data Summary	8-1
8.2	Loads Data Acquisition and Reduction	8-1
8.3	Loads Data Analysis	8-7

8.3.1	Effect of Variation of Dynamic Pressure	8-7
8.3.2	Loads Data as a Function of Mach Number	8-9
8.3.3	Impact of Nacelles on Wing Aerodynamics	8-10
8.3.4	Aerodynamic Response to Control Surface Deflection	8-11
8.3.5	Comparison of Flexible and Rigid Force Data	8-13
8.4	Pressure Data Acquisition and Reduction.....	8-16
8.4.1	Clean Wing Flexible/Rigid Pressure Comparison	8-25
8.4.2	Flexible/Rigid Pressure Comparison with Nacelles On	8-34
8.5	Aerodynamic Test Data Summary.....	8-39
9.0	CONCLUSIONS AND RECOMMENDATIONS	9-1
9.1	Finite Element Modeling and Pretest Experiments and Analyses	9-1
9.2	Aerodynamics	9-1
9.3	Flutter	9-3
10.0	REFERENCES	10-1

LIST OF FIGURES

1-1.	High Speed Research Flexible Semispan Model mounted in the NASA Langley Transonic Dynamics Tunnel.	1-1
2-1	HSRFlexible Semispan Model wing planform.	2-3
2-2.	Fuselage geometry and pressure port locations.	2-6
3-1.	HSR-FSM configuration 18-5 finite element model.	3-3
3-2.	Model 16-4 mode shapes and frequencies.	3-5
3-3.	Model 16-4 mode shapes and frequencies.	3-7
3-4.	Model 16-5 flutter boundary.	3-8
3-5.	HSR-FSM model 16-6 foam core.	3-9
3-6.	HSR-FSM model 17-5 foam core.	3-9
3-7.	Comparison of dynamic characteristics of models 16-6 and 17-6.	3-16
4-1.	Sketch of FSM and support system.	4-1
4-2.	FSM prepared for vibration testing in the calibration laboratory.	4-2
4-3.	Sketch of accelerometer locations.	4-4
4-4.	Experimental vibration frequencies and node lines for the laboratory configuration.	4-6
4-5.	Analytical frequencies and mode shapes for the laboratory configuration.	4-7
4-6.	Experimental frequencies and node lines for flutter configuration.	4-9
4-7.	Analytical frequencies and mode shapes for flutter configuration.	4-10
5-1.	Aerodynamic and structural models for the HSR-FSM exhibit significantly different grid resolutions	5-2
5-2.	The aerodynamic load is spread over a group of structural panels according to a user variable defining the number of layers surrounding the “nearest” structural panel.	5-4
5-3.	Surface aerodynamic pressure distribution used to simulate loads on the HSR-FSM. ...	5-5
5-4.	Aerodynamic load magnitude contours on the structural model.	5-6
6-1.	FSM loads test hardware.	6-3
6-2.	Static loads test arrangement.	6-4
6-3.	Displacements for loads at point 11503.	6-6
6-4.	Creep ratios for loads at point 11503.	6-7
6-5.	Displacements for torsion loads.	6-8
6-6.	Differential displacements of leading and trailing edge points for torsion loads.	6-10
6-7.	Displacements for 3° AOA distributed load.	6-13
6-8.	Creep for 3° AOA distributed load.	6-14
7-1.	ISAC Doublet Lattice model with superimposed FEM grid points.	7-2
7-2.	Pretest flutter analyses.	7-3
7-3.	Post-test flutter analyses for the wind-tunnel flutter configuration.	7-4

7-4.	STABCAR modal frequency and stability plots based on analytical frequencies and nominal damping.	7-6
7-5.	STABCAR modal frequency and stability plots based on experimental frequencies and damping.....	7-10
8-1.	Reference diagram for calculation of HSR-RSM aerodynamic loads.....	8-4
8-2.	Sample tabular output from force data post processing program.	8-6
8-3.	Sample plot from force data post processing program.	8-7
8-4.	Aerodynamic data for various values of dynamic pressure.....	8-8
8-5.	Aerodynamic data as a function of Mach number.	8-9
8-6.	Comparison of clean-wing and nacelles-on data at $M=0.95$	8-10
8-7.	Comparison of clean-wing and nacelles-on data at $M=1.15$	8-11
8-8.	HSR-FSM clean-wing steady flap deflection data.....	8-12
8-9.	HSR-FSM wing-with-nacelles steady flap deflection data.....	8-13
8-10.	Comparison of clean wing rigid (HSR-RSM) and flexible (HSR-FSM) lift curve slopes as a function of Mach number.	8-14
8-11.	Comparison of clean wing rigid (HSR-RSM) and flexible (HSR-FSM) pitching moment curve slope as a function of Mach number.	8-15
8-12.	Comparison of clean wing rigid (HSR-RSM) and flexible (HSR-FSM) drag coefficient at $CL = 0.1$ as a function of Mach number.	8-16
8-13.	Output from the wing pressure package macro.	8-18
8-14.	Output from the fuselage pressure package macro.....	8-23
8-15.	Comparison of clean wing flexible and rigid pressure distributions at $M=0.95$, $\alpha=2.0^\circ$	8-26
8-16.	Comparison of clean wing flexible and rigid pressure distributions at $M=1.15$, $\alpha=2.0^\circ$	8-30
8-17.	Comparison of flexible and rigid pressure distributions for wing with nacelles at $M=0.95$, $\alpha=2.0^\circ$	8-35

LIST OF TABLES

2-1.	Aeroelastic scale factors	2-2
2-2.	Wing surface pressure transducer locations	2-4
2-3.	HSR-FSM fuselage pressure port locations	2-7
3-1.	Chronology of FEM development supporting the HSR-FSM analysis	3-2
3-2.	Frequency and C.G. comparison between model with original mass locations and modified mass locations	3-10
3-3.	Physical and analytical model component weight comparison	3-12
3-4.	Tuned and original FEM component weight and C.G. locations	3-13
3-5.	Weight and C.G. locations for the HSR-FSM free-free GVT configuration.....	3-14
3-6.	Pitch and yaw moments of inertia for the HSR-FSM free-free GVT configuration	3-15
3-7.	Analytical weight and C.G. locations for the HSR-FSM.....	3-15
4-1.	Coordinates for accelerometer locations.....	4-3
4-2.	Key laboratory and TDT GVT configurations.....	4-5
4-3.	Measured frequencies and damping for selected configurations.....	4-5
4-4.	Comparison of test and analysis modes shapes	4-8
6-1.	Data files for static loads test	6-1
6-2.	Calculated and applied test loads.....	6-11
6-3.	Distributed load cycle for three degrees AOA.....	6-12
8-1.	HSR-FSM polar summary	8-2
8-2.	Balance load limits and assumed measurement resolution.....	8-3

1.0 Introduction

This report presents the work performed by Lockheed Martin Langley Program Office (LPO) in support of the High Speed Research (HSR) Flexible Semispan Model (FSM). Although the genesis of the FSM goes back several years, the activities described here occurred primarily in 1995 and 1996. During that period, the level of activity steadily increased until the program culminated in Test 521 conducted in LaRC's Transonics Dynamics Tunnel, 8 April to 6 May, 1996. Figure 1-1 shows the FSM prepared for testing in the TDT. The program was led by LaRC's Aeroelasticity Branch with participation by the HSR industry partners (Boeing and McDonnell Douglas) as well as LPO.

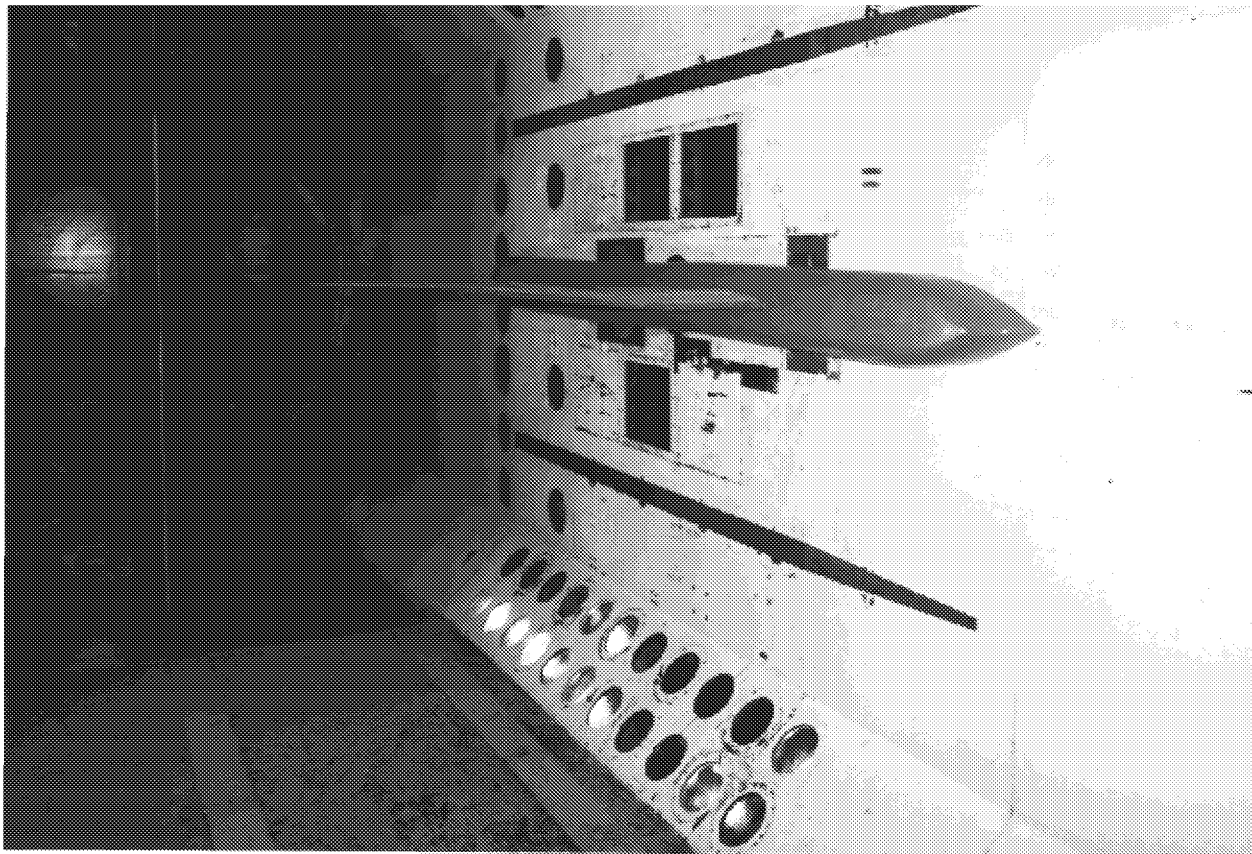


Figure 1-1. High Speed Research Flexible Semispan Model mounted in the NASA Langley Transonic Dynamics Tunnel.

The test was conducted in order to assess the aerodynamic and aeroelastic character of a flexible high speed civil transport wing. Although the wing was roughly based on the HSR Reference H concept, data was acquired for the purpose of code validation and trend evaluation for this type of wing, and was not intended to be a flutter clearance or detailed analysis of a specific full-scale airplane.

The wind-tunnel test consisted of an aerodynamics/loads phase and a flutter phase. In order to acquire unsteady aerodynamics and loads data, the wing was fitted with a trailing edge control

surface which was both steadily deflected and oscillated during the test to investigate the response of the aerodynamic data to steady and unsteady control motion. Angle-of-attack and control surface deflection polars at subsonic, transonic and low-supersonic Mach numbers were obtained in the tunnel's heavy gas configuration. Unsteady pressure and steady loads data were acquired on the wing, while steady pressures were measured on the fuselage. These data were reduced using a variety of methods, programs and computer systems.

With minor exceptions, the flutter portion of the test was conducted with the same basic configuration as the aerodynamics/loads phase. The emphasis was on identifying transonic and subsonic flutter points with minimum static loads on the wing. While valuable transonic dynamics and flutter data were obtained, unfortunately, the model was destroyed during transonic flutter and a complete experimental flutter boundary could not be mapped out.

LPO was responsible for a number of activities in preparing for and conducting the wind-tunnel test. These included coordination of the design and fabrication, development of analytical models, analysis/hardware correlation, performance of laboratory tests, monitoring of model safety issues, and wind-tunnel data acquisition and reduction. A great deal of the data obtained prior to the wind-tunnel test, along with analyses, were used for test planning and model safety purposes. For example, wing loads predicted via aerodynamic analyses were used for both the safety stress analysis and the laboratory distributed proof load. Just prior to the wind-tunnel test, vibration, static loads and mass/inertia tests were conducted. Vibration tests were also conducted in the TDT between wind-tunnel runs. Selected portions of these data along with the wind-tunnel loads and aerodynamics data were ultimately compiled onto a CD-ROM volume which was distributed to HSR industry team members in August, 1996. This report complements the stored data by documenting the methods used to acquire and reduce the data, and provides an assessment of the quality, repeatability, and overall character of the data. The descriptions and discussions included are those which the authors believe to be of greatest value to future HSR efforts.

Descriptions and relevant evaluations associated with the pretest data are given in sections 1 through 6, followed by pre- and post-test flutter analysis in section 7, and the results of the aerodynamics/loads test in section 8. Finally, section 9 provides some recommendations based on lessons learned throughout the FSM program.

2.0 HSR-FSM Wind Tunnel Model

In 1991, work was begun on an “HSCT-like” model to be instrumented with a full suite of pressure transducers and accelerometers. The aim of the program was to obtain steady and unsteady pressure data for a flexible wing undergoing flutter for code validation. This effort was later incorporated into the HSR program (with the same objective).

Although the planform is based on the Reference H concept, the thickness is uniformly four percent of the local chord length. This resulted in a model which was proportionately thicker than the Reference H near the tip, but thinner near the root. This was to allow sufficient instrumentation space in the outer wing.

In early 1995, the effort to size the “stressed skin” design for flutter in the TDT began in earnest. The TDT flutter mechanism was to be a wing-alone mechanism which was not the critical mechanism predicted for the Reference H. An experimental study of the critical fuselage/wing coupling mechanism was to be postponed until the full-span, cable-mounted model was developed. Because of this decision and the tight time schedule, further work on designing a flexible mounting rail as an attempt to simulate the fuselage wing coupling was terminated. At that point, the focus was on identifying and obtaining a skin material which was sufficiently flexible to allow flutter in the TDT, yet strong enough for the anticipated worst-case loads. Because of the need to acquire aeroelastic loads data, loading was to be higher for the FSM than for many flutter models. This led to the design involving laid-up Fiberglass 108, which was the most flexible material identified which could sustain anticipated loads. The results of this design decision are discussed in subsequent sections.

2.1 Aeroelastic Scaling

Given the overall dimensions of the FSM, stiffness and mass sizing of the wind-tunnel model were initially based on aeroelastic scaling of the Reference H configuration. Table 2-1 gives the full-scale and model-scale aeroelastic parameters. These factors served as a guide in the design and analysis of the model. However, final flutter sizing was based on flutter analyses using the planned TDT test envelope and the Finite Element Model (FEM) which continually underwent revision based on the most recent information available.

2.2 Model Description

The design, construction and instrumentation of the HSR-FSM is discussed in this section. The wing was designed for aeroelastic testing at subsonic, transonic and low supersonic speeds in the TDT. The wing was instrumented with surface pressure, accelerometer and strain gages, and for the aerodynamic loads portion of the test, it was mounted on a five-component force balance. The model included a fuselage which serves primarily as a fairing for the wing mounting hardware and the extensive instrumentation wiring and reference pressure tubes. The fuselage was instrumented with static surface pressures.

The model was aeroelastically scaled to flutter at dynamic pressures around 200 psf, but it was also designed to be stable at lower dynamic pressures so that static aeroelastic data could be obtained in the 100 - 150 psf range. The model was fitted with a hydraulically actuated inboard wing trailing edge control surface. This surface was statically and dynamically deflected during the low dynamic pressure testing to obtain steady and unsteady aerodynamic data.

Table 2-1. Aeroelastic scale factors

Parameter	Symbol	Formula	Value
Full-scale Airplane Design Point			
Mach No.	M		0.9
Speed of Sound	a_A (fps)		1077
Dynamic Pressure	q_A (psf)		825
Velocity	V_A	$M a_A$	969.30
Atmospheric Density	ρ_A (slugs/ft ³)	$2 q_A / V_A^2$	0.001756
Length (Wing Semispan)	L_A (ft.)		64.82
Airplane Weight	W_A (lb.)		257,857
Airplane Flutter Frequency	f_A (Hz.)		4.36
Model Design Point			
Length (Wing Semispan)	L_M (ft.)		5.4
Dynamic pressure	q_M (psf)		200
Tunnel Speed of Sound	a_M (fps)		505
Model Weight	W_M (lb.)		164.38
Model Flutter Frequency	f_M (Hz.)		16.36
Scale Factors			
Dynamic Pressure	q_{SF}	q_M / q_A	0.242
Velocity	V_{SF}	a_M / a_A	0.469
Density	ρ_{SF}	q_{SF} / V_{SF}^2	1.102
Length	L_{SF}	L_M / L_A	0.083
Mass	M_{SF}	$\rho_{SF} L_{SF}^3$	0.000637
Reduced Frequency Factor	c	k_A/k_M	1.50
Frequency	f_{SF}	$1/c (V_{SF} / L_{SF})$	3.752

2.2.1 Wing Model and Instrumentation

The HSR-FSM wing was a modified 1/12 scale model of the Boeing Reference HSCT Configuration (Reference H). The HSR-FSM wing planform is shown in Figure 2-1. Modifications to the basic Reference H configuration included removal of the inboard trailing edge extension, and the scaling of the airfoil sections so that a constant 4% thick section was maintained over the entire wing planform. The thickness scaling was performed to provide sufficient outboard wing volume

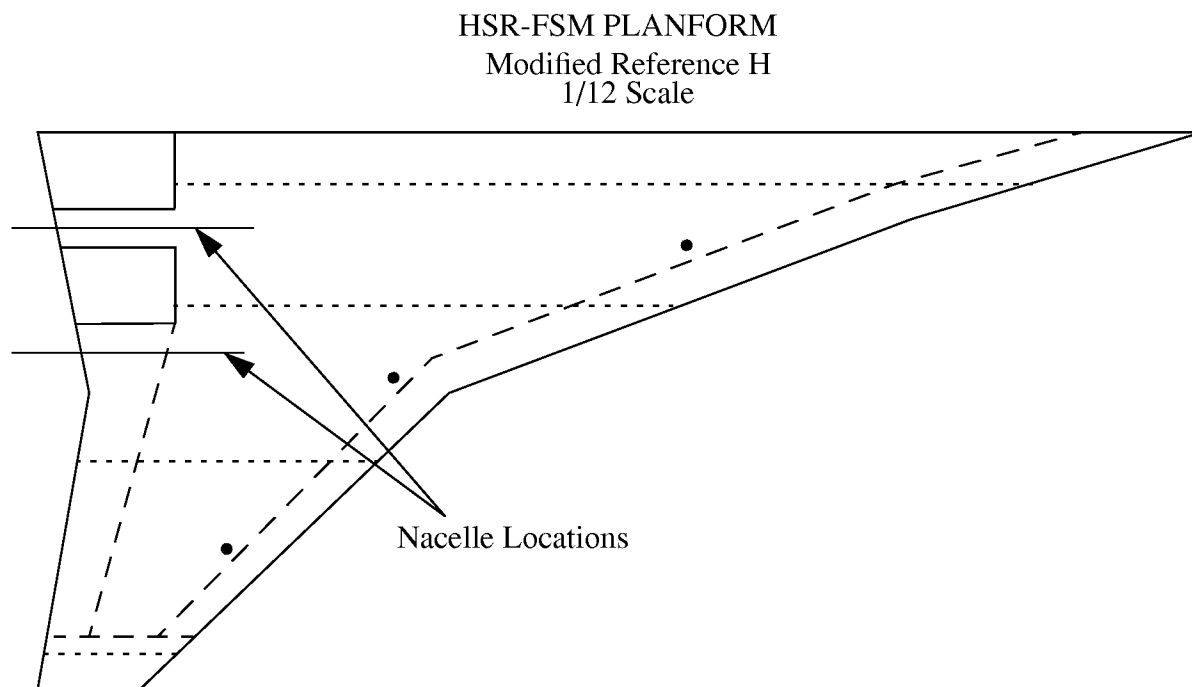


Figure 2-1. HSR Flexible Semispan Model wing planform.

for the pressure instrumentation. The trailing edge flap employed on the HSR-FSM was not designed to be representative of control systems to be used on HSCT flight vehicles, but rather as a mechanical artifact for exciting the flowfield about the wing for unsteady aerodynamic observations. A pair of flow-through nacelles were also fabricated to determine the impact of these components on the aerodynamics of the wing. As shown in Figure 2-1, the nacelles were attached to short pylons along the lower surface inboard trailing edge of the wing. The flap employed on this model differs from that used on the HSR-RSM in that it was split to allow it to be deflected with the nacelles attached. Both flap sections were driven by a common shaft.

The wing was constructed primarily of fiberglass and foam. It consisted of five major components, the main wing box, leading and trailing edge fairings, a wing tip cap and instrumentation holder, and the trailing edge flap. The largest section of the wing, the wing box, consisted of a two-piece foam core bonded to fiberglass external skins. The heavy dashed lines in Figure 2-1 represent seams between the main wing box and the removable leading edge, trailing edge and wing tip sections. These fairings provided access to instrumentation in these areas and also served as routing paths for wiring and pressure reference tubes. Instrumentation was also routed through conduit in the main wing foam core.

The chordwise dotted lines in Figure 2-1 represent the locations of the primary pressure instrumentation on the wing. Pressure transducers were located at 10, 30, 60 and 95 percent span. There were a total of 137 wing pressure transducers. As shown in the figure, the 10 and 30 percent span locations contained pressure instrumentation only as far back as the leading edge of the flaps. The 60 and 95 percent span locations contained instrumentation all of the way to the wing trailing edge. Table 2-2 lists the fractional chordwise location of each pressure transducer at these four span stations. In addition to these 131 transducers there are six transducers located on the upper and lower surfaces at 20 percent chord and 20, 45 and 75 percent span, shown by the solid circles in the figure.

Table 2-2. Wing surface pressure transducer locations

Upper Surface							
10% Span		30% Span		60% Span		95% Span	
X/C	Channel Number	X/C	Channel Number	X/C	Channel Number	X/C	Channel Number
0.0	151	0.0	111	0.0	65	0.0	31
0.025	186	0.025	145	0.05	66	0.10	32
0.05	152	0.05	112	0.10	67	0.20	33
0.10	153	0.10	113	0.15	68	0.30	34
0.15	154	0.15	114	0.20	69	0.40	35
0.20	155	0.20	115	0.25	70	0.50	36
0.25	156	0.25	116	0.30	71	0.60	37
0.30	157	0.30	117	0.35	72	0.70	38
0.35	158	0.35	118	0.40	73	0.80	39
0.40	159	0.40	119	0.45	74	0.90	40
0.45	160	0.45	120	0.50	75		
0.50	161	0.50	121	0.55	76		
0.55	162	0.55	122	0.60	77		
0.60	163	0.60	123	0.65	78		
0.65	164	0.65	124	0.70	79		
0.70	165	0.70	125	0.75	80		
0.75	166	0.75	126	0.80	81		
0.80	167	0.80	127	0.85	82		
0.85	168			0.90	83		
				0.95	84		
				1.0	85		

Table 2-2. Wing surface pressure transducer locations

Lower Surface							
10% Span		30% Span		60% Span		95% Span	
X/C	Channel Number	X/C	Channel Number	X/C	Channel Number	X/C	Channel Number
0.025	187	0.025	146	0.05	86	0.10	42
0.05	169	0.050	129	0.10	87	0.20	43
0.10	170	0.10	130	0.15	88	0.30	44
0.15	171	0.15	131	0.20	89	0.40	45
0.20	172	0.20	132	0.25	90	0.50	46
0.25	173	0.25	133	0.30	91	0.60	47
0.30	174	0.30	134	0.35	92	0.70	48
0.35	175	0.35	135	0.40	93	0.80	49
0.40	176	0.40	136	0.45	94	0.90	50
0.45	177	0.45	137	0.50	95		
0.50	178	0.50	138	0.55	96		
0.55	179	0.55	139	0.60	97		
0.60	180	0.6	140	0.65	98		
0.65	181	0.65	141	0.70	99		
0.70	182	0.70	142	0.75	100		
0.75	183	0.75	143	0.80	101		
0.80	184	0.80	144	0.85	102		
0.85	185			0.90	103		
				0.95	104		

The wing was mounted on a five-component force balance located at the wing root. The balance measures normal and axial loads along with pitch, yaw and roll moments. The fuselage is mounted so that it does not transfer load to the balance, thus in the test configuration described in this report, only wing loads were monitored by the balance.

2.3 Fuselage Model and Instrumentation

A schematic of the HSR-FSM fuselage is shown in Figure 2-2. The fuselage serves primarily as a fairing for the wing mounting hardware, instrumentation wiring, and pressure reference tubes. It also serves as a spacer to displace the wing away from the wind tunnel wall and out of its boundary layer. However, since it is in close proximity to the wing, it provides aerodynamic interference which must be accounted for in theoretical models. Therefore, it is also equipped with pressure

measurement instrumentation. Steady pressure measurements are made at seven stations along the fuselage. Pressure ports are spaced in the circumferential direction at each constant fuselage station. In total, there are 119 ports on the fuselage surface. The location and corresponding data channel number for each of these ports is presented in Table 2-3.

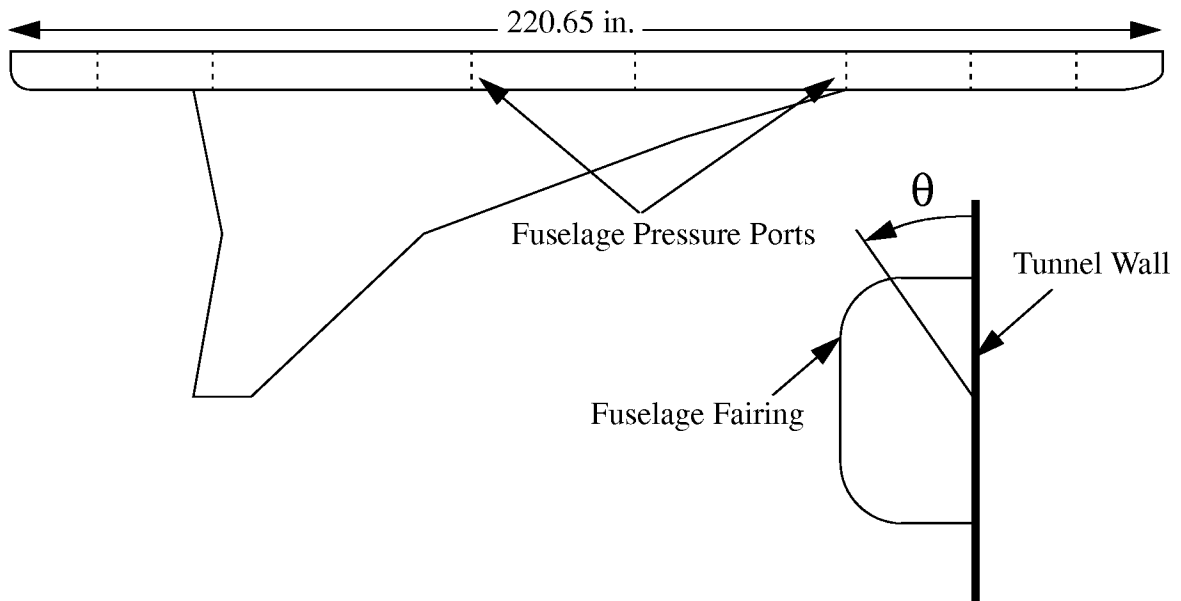


Figure 2-2. Fuselage geometry and pressure port locations.

Table 2-3. HSR-FSM fuselage pressure port locations.

Fuselage Pressure Port Locations							
θ measured from upper fuselage symmetry plane, X measured from fuselage nose.							
X = 16 in.		X = 36 in.		X = 60 in.		X = 102 in.	
θ (°)	Channel	θ (°)	Channel	θ (°)	Channel	θ (°)	Channel
9.23	1	7.97	17	7.97	33	54.00	49
13.78	2	15.64	18	15.64	34	57.13	50
18.22	3	22.78	19	22.78	35	60.23	51
26.56	4	35.26	20	35.26	36	63.30	52
40.71	5	54.00	21	54.00	37	66.36	53
47.33	6	66.36	22	66.36	38	67.93	54
80.99	7	79.81	23	79.81	39	69.53	55
90.00	8	90.00	24	90.00	40	71.17	56
99.01	9	100.19	25	100.19	41	108.83	57
132.67	10	113.64	26	113.64	42	110.47	58
139.29	11	126.00	27	126.00	43	112.07	59
153.44	12	144.74	28	144.74	44	113.64	60
161.78	13	157.22	29	157.22	45	119.77	61
166.22	14	164.36	30	164.36	46	122.87	62
170.77	15	172.03	31	172.03	47	126.00	63
X = 132 in. (Upper)		X = 132 in. (Lower)		X = 182 in.		X = 204 in.	
θ (°)	Channel	θ (°)	Channel	θ (°)	Channel	θ (°)	Channel
7.97	65	107.16	81	7.97	97	7.97	113
15.64	66	108.83	82	15.64	98	15.64	114
22.78	67	110.47	83	22.78	99	22.78	115
29.24	68	112.07	84	35.26	100	35.26	116
35.26	69	113.64	85	54.00	101	54.00	117
41.43	70	116.70	86	66.36	102	66.36	118
54.00	71	119.77	87	79.81	103	79.81	119
57.13	72	122.87	88	90.00	104	90.00	120
60.23	73	126.00	89	100.19	105	100.19	121
63.30	74	138.57	90	113.64	106	113.64	122
66.36	75	144.74	91	126.00	107	126.00	123
67.93	76	150.76	92	144.74	108	144.74	124
69.53	77	157.22	93	157.22	109	157.22	125
71.17	78	164.36	94	164.36	110	164.36	126
		172.03	95	172.03	111	172.03	127

3.0 Finite Element Modeling

A series of MSC/NASTRAN¹ finite element models (FEMs) were developed and analyzed to support the development, construction, and testing of the HSR-FSM. These models served primarily as dynamic models for analysis of the flutter characteristics of the HSR-FSM. Structural dynamic characteristics computed using these models were correlated with ground vibration tests (GVTs) conducted in the laboratory and in the TDT test section. The results of these comparisons are presented in Section 4.0 Ground Vibration Testing. Pretest flutter analyses were used to set the preferred configuration for flutter testing, and to predict the dynamic behavior of the model during the test. The flutter analysis is described in Section 7.0 Flutter Analysis.

In addition, a NASTRAN model was developed by LaRC Systems Engineering for stress analysis. This analysis was used to define operating limits and safety margins for wind tunnel testing of the HSR-FSM. The stress model is described in a NASA internal report (NASA LaRC EAB Report 96-02, June, 1996). This section describes only the dynamics models.

3.1 Chronology of FEM Development

Table 3-1 lists the primary models developed prior to and during the construction and testing of the HSR-FSM. The table begins in July, 1995 with model 15-4, which is the last of the preliminary models developed prior to initiation of the physical model construction. There are four series of dynamics models. The 15-series can be characterized as preconstruction models, and typically have estimated geometric and material properties. The 16-series of models were developed as the physical model was constructed. This series of models typically has more accurate material properties, and the geometry of the wing is very close to that of the final physical model. The 17-series models was developed following model construction, but prior to wind-tunnel testing. This group of models includes the actual masses of the physical model components, and further improved material properties obtained from coupon tests and data obtained from stiffness measurements and the pretest GVT. The 18-series of models was developed during the actual wind tunnel testing of the HSR-FSM. During this period, most of the pretest wing and support structure stiffness data were finalized and incorporated into the FEM. Figure 3-1 shows the FEM for model 18-5, which is the final flutter configuration for the FSM.

During the entire course of the FEM development, the dynamic character of the model was monitored by performing NASTRAN dynamic and linear flutter analyses. These analyses further guided the development of the physical and analytical models and were also used to set the configuration of the model for flutter testing in the TDT. There are several points in the development of the FEM which had a significant impact on the dynamic performance of the model. These milestones will be highlighted in this section, while details surrounding much of the analysis supporting these points will be covered in other sections.

**Table 3-1. Chronology of FEM development supporting the
HSR-FSM analysis**

Model Number	Date	Description
15-Series - Pretest Analysis Models Based on Theoretical Structural Properties		
15 - 4	July, 1995	Skewed CQUAD4 elements corrected, initial model of flexible balance and support structure, engine masses modeled, flaperon modeled, 108 fiberglass properties replaced with preliminary test values.
16-Series - Pretest/Preassembly Analysis Models with Updated Geometric, Mass and Structural Properties.		
16-2	November, 1995	Wing surface splining errors near primary wing break corrected, split flaperon modeled.
16-3	November, 1995	Simulated fuel ballast weight added.
16-4	November, 1995	Material properties from coupon test averages, split flap geometry updated to proper butt line locations.
16-5	January, 1996	Flutter analysis model to investigate the sensitivity of the flutter characteristics to additional wing masses.
16-6	February, 1996	Improved nacelle mount modeling, corrected modeling of the flap actuator and shaft.
17-Series - Pretest Models Developed During Assembly and Evaluation of Physical Model		
17-1	February, 1996	Measured Nacelle Weights, C.G., and Inertias added to model.
17-2	February, 1996	Fiberglass lay-up and material properties updated for skins, L.E., T.E., and spars.
17-3	February, 1996	Model component weights updated to known physical component weights. Model used during pretest GVT analyses.
17-4	February, 1996	Nacelle masses updated.
17-5	February, 1996	Improved mounting foot modeling.
17-6	March, 1996	Wiring and instrumentation mass added.
17-7	March, 1996	Simplified mounting hardware stiffness model from cal-lab measurements.
17-8	March, 1996	Support structure masses approximated.
17-9	March, 1996	Detailed mounting hardware stiffness model from cal-lab measurements.
17-10	March, 1996	Measured fuselage beam areas and moments of inertia added to model.

**Table 3-1. Chronology of FEM development supporting the
HSR-FSM analysis**

Model Number	Date	Description
18-Series - Models Developed During Testing of the HSR-FSM in the TDT		
18-1	April, 1996	Further refined balance/strut model.
18-2	April, 1996	Fiberglass 108 material properties updated using static load bending test data.
18-3	April, 1996	Adjusted fiberglass 108 shear modulus based on static load torsional test data. Added fuselage weight connected directly to top of rigid strut.
18-4	April, 1996	Fuselage weight connected to top of rigid strut via sprung mount.
18-5 18-5eotm	April, 1996	Final balance/strut model. Flutter test configuration, engine-off, 2.5 lb. tip mass.

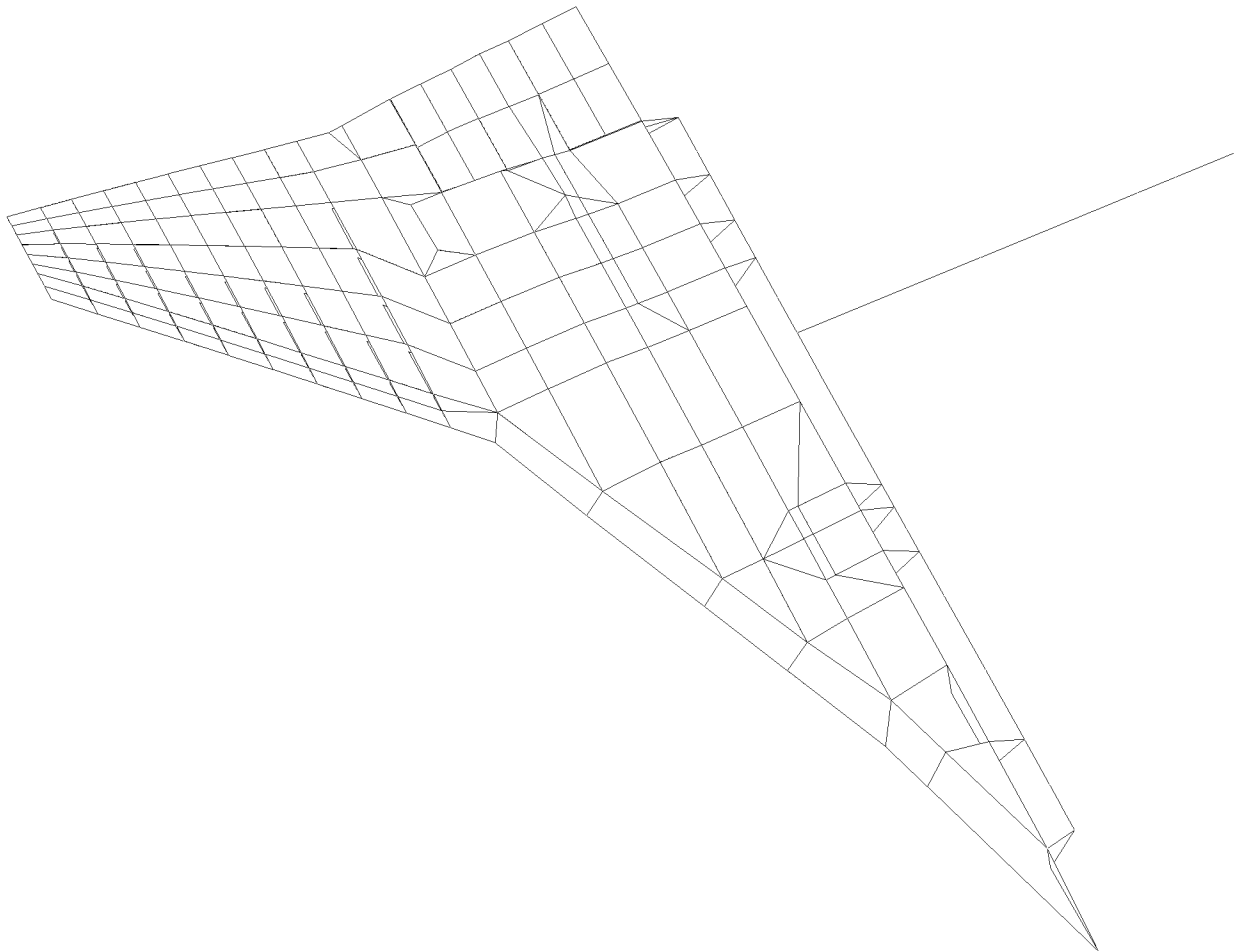


Figure 3-1. HSR-FSM configuration 18-5 finite element model.

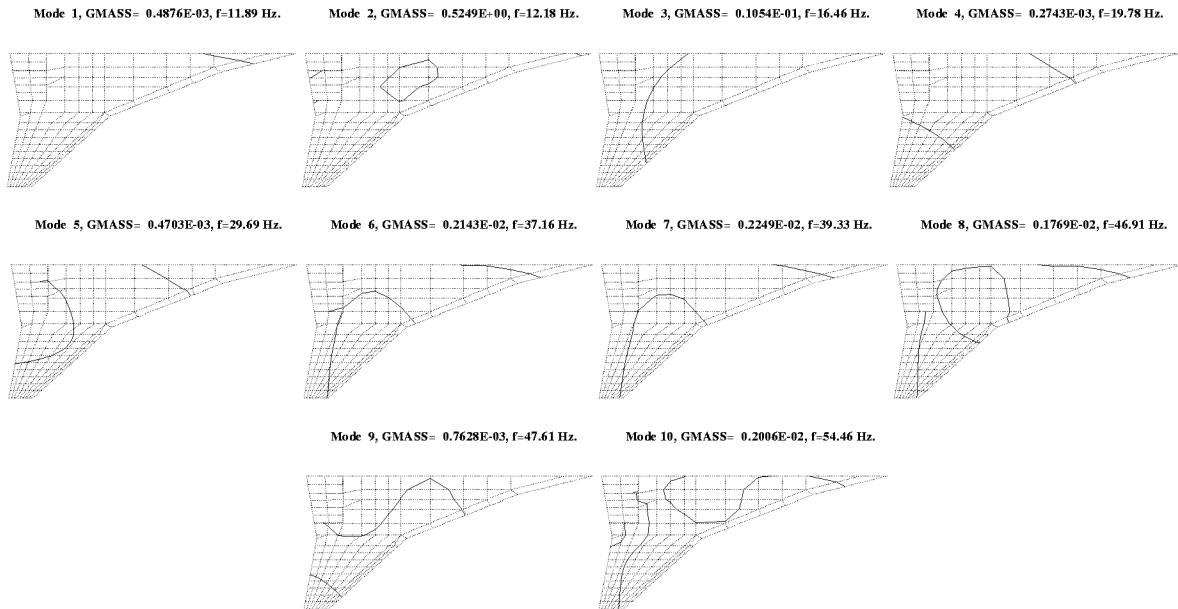
3.2 Baseline FEM Development and Dynamic Analysis.

Preliminary analyses using models 15-4 and earlier indicated an acceptable flutter mechanism involving a bending/torsion coupling of the outer wing. For these models, flutter occurred at a dynamic pressure of approximately 170 psf, and a frequency of approximately 20 Hz. As the model progressed into the 16-series, an error in the splining of the wing which created a streamwise trough in the surface near the primary planform break was discovered and corrected. Material properties derived from coupon tests of the fiberglass used in the construction of the model were also included in the FEM as were the ballast weights simulating the wing fuel load. This brought the configuration to model 16-4, which represents the first configuration which could be considered a reasonable approximation to the physical model.

Figure 3-2 shows both the node lines and an isometric view of the mode shapes for the first 10 modes of configuration 16-4. There are several characteristics of this model which are important to the dynamic behavior of the FSM, and the subsequent development of the flutter configuration tested in the TDT. First, it should be noted that mode 2 is a yaw mode that is always present, but does not play a significant role in the wing's flutter mechanism. Modes 1 and 4 are outer wing bending modes, and they are almost always involved in the flutter mechanisms of interest. Rigid body pitch characterizes mode 3, which ultimately becomes problematic in the flutter analysis of this wing. Modes 6 and 7 are primarily torsion modes that also play a role in the flutter analysis. The modes beyond 40 Hz do not have a major effect on the principal flutter modes.

Flutter analyses of this model unfortunately did not produce flutter at dynamic pressures less than 400 psf. To investigate this problem and identify a configuration which would produce flutter at reasonable dynamic pressures, a series of parametric analyses were initiated which added mass to various portions of the wing. It had already been determined that the addition of the nacelles would not produce flutter, and adding weight to one or both of the nacelles also did not solve the problem. Mass was finally added along the leading and/or trailing edge of the outer wing panel, and it was found that this technique was effective in producing a flutter boundary at dynamic pressures and frequencies suitable for TDT testing. The results of a parametric study of weight size and location showed that adding 2.0 lb. to the wing tip trailing edge of the model, and 2.4 lb. to the mid-span of the outer wing leading edge produced a flutter mechanism in the 175 psf dynamic pressure range at a frequency of approximately 15 Hz.

NASTRAN Node Lines HSR-FSM Model 16-4



NASTRAN Mode Shapes HSR-FSM Model 16-4

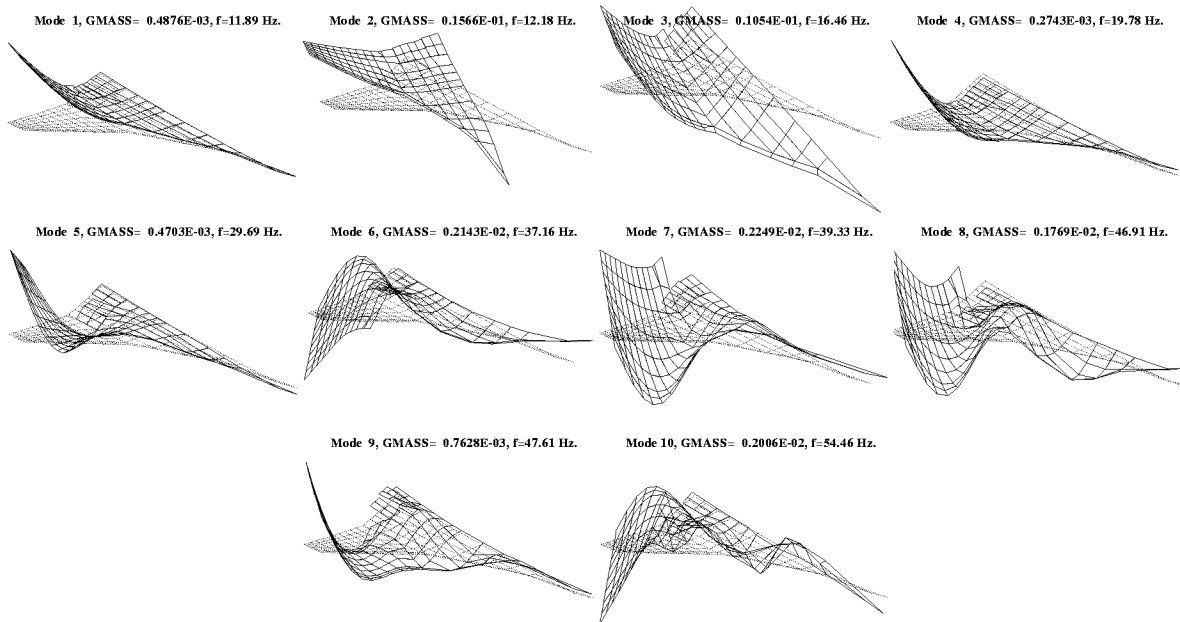


Figure 3-2. Model 16-4 mode shapes and frequencies.

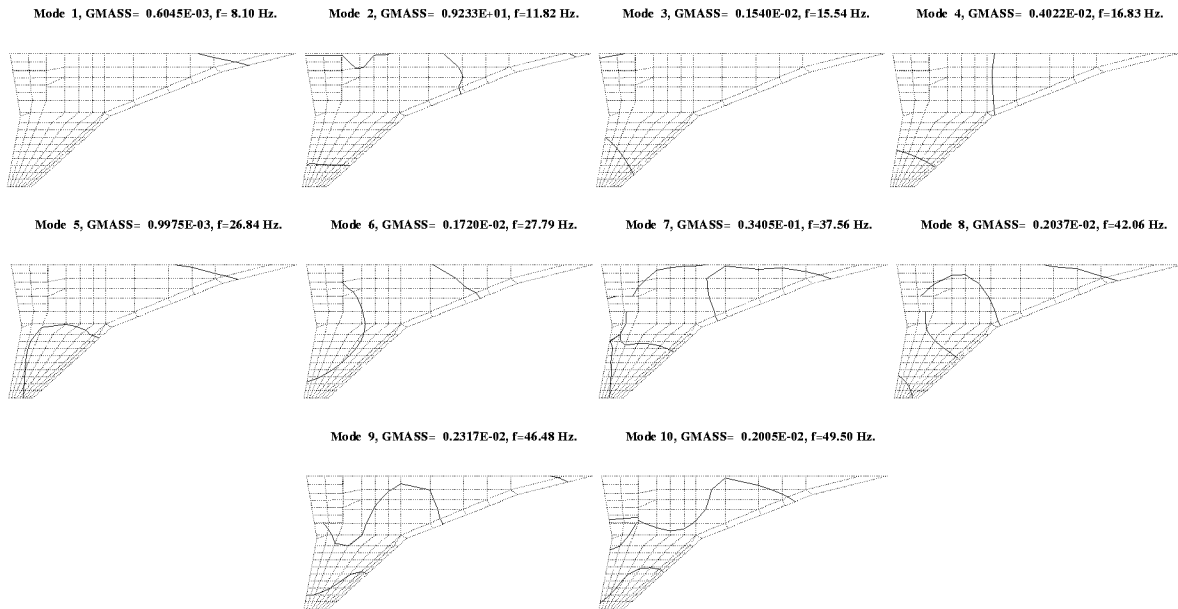
The node lines and mode shapes for this model, designated 16-5w, are shown in Figure 3-2. The addition of the weight in the outer wing significantly reduced the natural frequencies of the first and second bending modes, as well as the torsion modes. The flutter boundary for this configuration is shown in Figure 3-2. While this configuration produces flutter at reasonable conditions, the rigid body pitch mode plays a significant role in the flutter mechanism, which is not physically realistic for this vehicle. To remove this participation, the wing root was constrained in translation and rotation. The impact of this constraint is shown as the triangles in the figure. The flutter dynamic pressure was raised to approximately 200 psf, and the frequency was also slightly higher. However, the flutter mechanism involved only outer wing modes, which was the desired physical mechanism. It should also be noted, that during the parametric analysis, a second flutter mode sporadically appeared at dynamic pressures on the order of 300 psf, and frequencies of about 30 Hz. This mode was typically a hump mode instability. Although the mode was present on model 16-5, it did not cause an instability.

A great deal of the model instrumentation passes through the mid-span leading edge portion of the wing, and it was difficult to add weight in this area due to volume constraints. We were able to demonstrate that flutter could be obtained using only the trailing edge tip weight. In addition, removable trailing edge weights made of tungsten could be easily manufactured to fit in the removable trailing edge section, out of the way of instrumentation. This provided an added safety benefit since the wing could be configured without the weights during the static aeroelastic portion of the test, reducing the risk of encountering unanticipated flutter. Thus the final wind tunnel configuration included the wing tip trailing edge weight. In addition, a forward support for the fuselage beam was fabricated to remove the rigid body pitch mode from the wind tunnel model. Unfortunately, this support posed a number of mechanical problems in itself, and questions surrounding its ability to effectively constrain the wing resulted in it being abandoned as a viable alternative for the final test configuration.

The remainder of the 16-series development involved refinement of the geometric and mechanical properties of the FEM. This included improving the modeling of the nacelle attachment, the nacelle mass, and the flap shaft and actuator mechanics. Model 16-6 is the last of the 16-series of the FEM, and it is the baseline model for incorporation of the physical model measured properties.

NASTRAN Node Lines

Model 16-5w, 2.4 lb. MLE, 2.0 lb. TTE, Unconstrained Root.



NASTRAN Mode Shapes

Model 16-5w, 2.4 lb. MLE, 2.0 lb. TTE, Unconstrained Root.

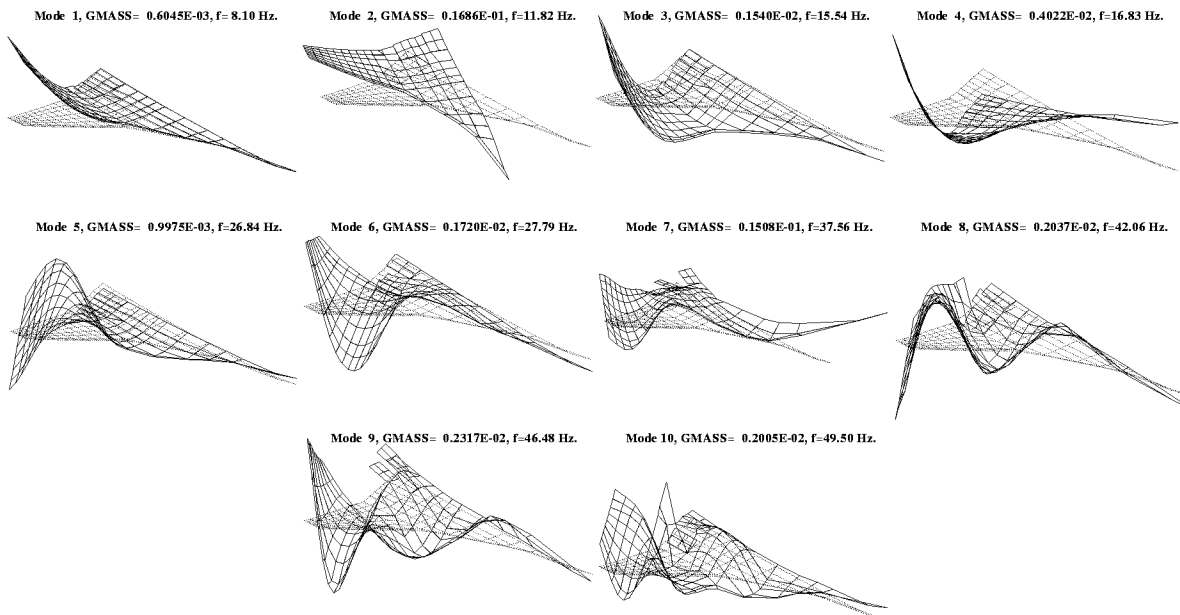


Figure 3-3. Model 16-4 mode shapes and frequencies.

HSR-FSM Analytical Flutter Boundary Kernel Function Aerodynamics

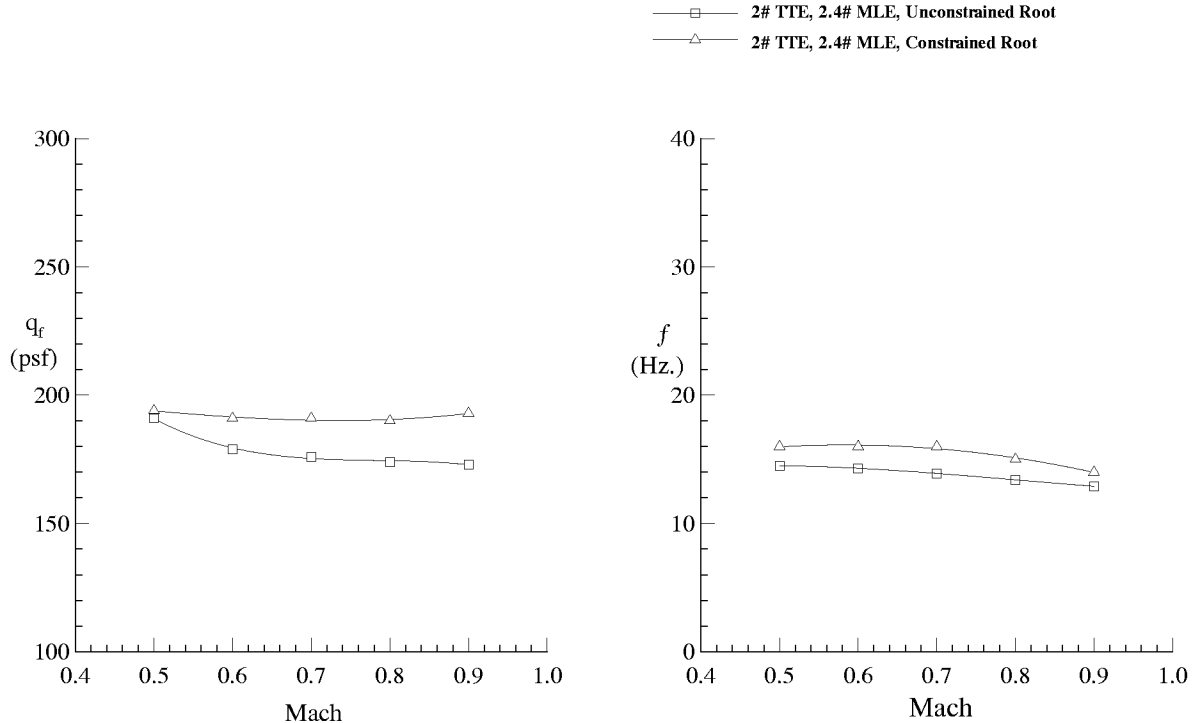


Figure 3-4. Model 16-5 flutter boundary.

3.3 FEM Refinement and Mass Tuning

The FEM for the HSR-FSM was updated to include various measured mass and material properties. As the physical model was constructed in the NASA Composite Model Shop, LPO and NASA personnel carefully weighed and measured the various model components. Similar analytical “weighings” of the FEM were also performed using NASTRAN, and the FEM was subsequently tuned to more accurately represent the physical model. This section summarizes the tuning of the FEM, and compares the mass properties of the FEM with the physical model.

3.3.1 Modeling Issues

A significant modification to the FEM was performed to improve the modeling of the fuselage beam mounting feet which are bonded into the wing. In model 16-6, only the aft foot was modeled with any detail, and many of the properties of this component were in error. The original aft foot was modeled by a series of 0.05 inch thick aluminum plates that were located just beneath the fiberglass skin. These plates were too thin and did not extend far enough into the wing core. The plates which were bonded into the wing for the forward and middle foot were not modeled. To correct this situation, a series of grid points were added to the model, and new elements were developed to model the forward, middle and aft mounting plates. Aluminum plates with a thickness of 0.375 in. were placed directly beneath the upper and lower surface wing skins to simulate the

mounting feet. Rigid bars between the upper and lower plates were used to tie the plates together and simulate the shear webbing used in these components on the physical model.

The foam core was also modified. Originally the foam core was not removed in the vicinity of the feet, as shown in Figure 3-5. Figure 3-6 shows a planform view of the core of model 17-5 which has the foam removed where the foot plates are bonded to the wing skins. This is a more accurate representation of the physical model, and removing the foam core from the FEM redistributes a significant portion of the foam core mass outboard on the wing.

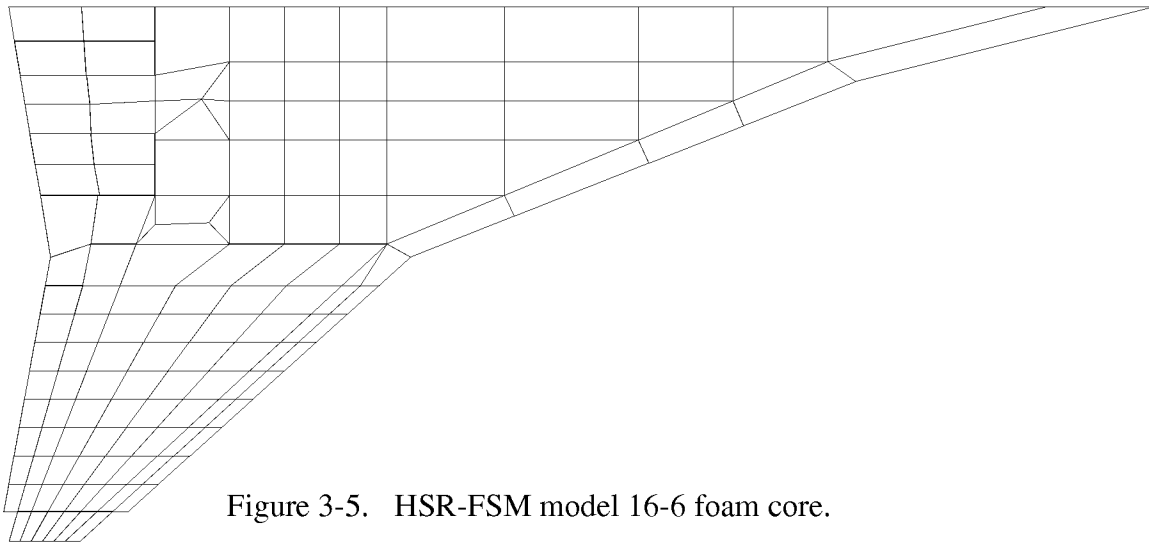


Figure 3-5. HSR-FSM model 16-6 foam core.

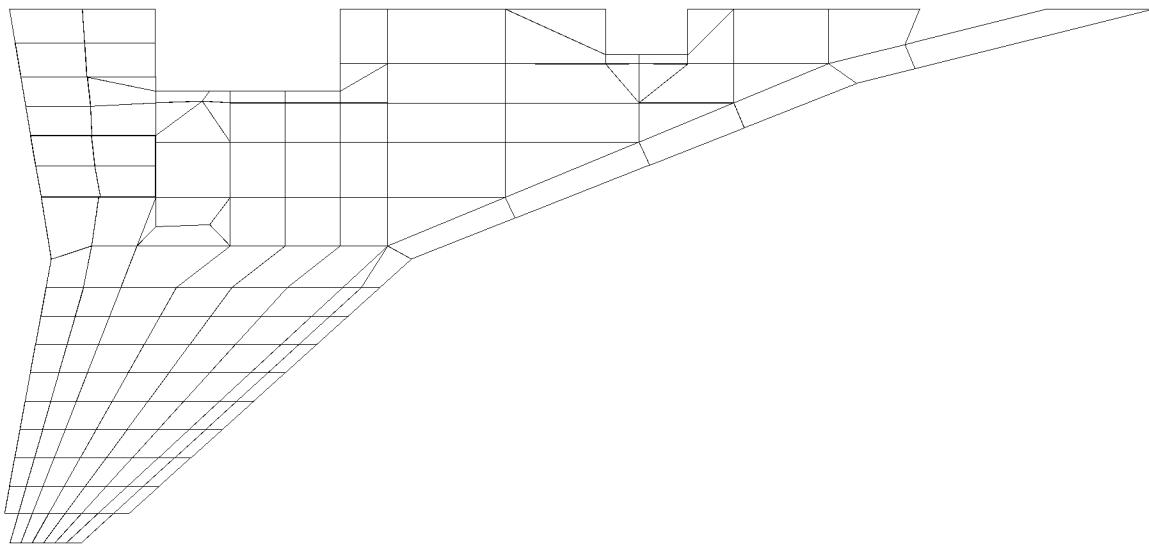


Figure 3-6. HSR-FSM model 17-5 foam core.

A large amount of work on the FEM was performed by Boeing to move the ballast weights embedded in the wing to the physical locations in the model. As the model was constructed, personnel in the NASA Composite Model Shop realized that the lead ballast weights could not be placed exactly where we had asked for them. After some coordination, the weights were placed as close to the NASTRAN model grid points as possible, but some of the weights were still not installed close to the desired locations. Boeing moved the weights in the FEM to the correct physical locations, and computed moments of inertia for each of the weights. Unfortunately, the movement of the weights introduced a number of local modes, most of which were removed by tying the weights to other parts of the structure. We incorporated Boeing's model into the LPO FEM and compared it to the FEM with the original mass locations. Results of that comparison are summarized in Table 3-2. Up to a frequency of approximately 50 Hz., the comparison is reasonable. However, there were nine modes between 48 and 62 Hz. for the modified configuration, indicating that the masses were still adding local modes to the analysis. The table also presents the C.G locations for the two models. The fuselage station and butt line locations for the C.G agreed to within 0.15 in. The waterline location had a slightly larger difference due to the fact that in the original mass distribution each mass was evenly divided between the upper and lower surface grid points, while the entire mass was located along the upper surface for the modified ballast location model.

Table 3-2. Frequency and C.G. comparison between model with original mass locations and modified mass locations.

Mode	Frequency	
	Original Ballast Location	Modified Ballast Location*
1	13.34	13.35
2	16.64	16.70
3	28.85	28.98
4	35.32	36.49
5	40.01	39.57
6	44.23	43.81
7	48.89	48.34
8	52.52	50.95
9	59.74	52.84
10	61.81	54.59
* Local modes between 48 and 62 Hz are not listed.		
X _{C.G.}	175.41	175.56
Y _{C.G.}	17.02	16.89
Z _{C.G.}	18.22	18.72

The data shown in Table 3-2 is for the so-called “free-free” configuration used in the initial GVT analysis. Even though the closely spaced modes are fairly high in frequency, they appear in the frequency range considered for comparison of the GVT and analysis and they cause difficulties in the correlation. However, for the baseline configuration, as mounted in the TDT, they fall outside the frequency range of interest and there is not a great deal of difference in the dynamic characteristics of the two mass distribution models at the lower frequencies. Therefore, to eliminate complication and possible confusion, the original ballast locations were retained in all subsequent FEM revisions.

3.3.2 Mass Properties

Initial estimates of the engine nacelle masses and moments of inertia, developed by Boeing using solid modeling tools, were incorporated into the working FEM for the HSR-FSM. Subsequent weighings and experiments verified that the Boeing inertias were accurate, and this information was included in the FEM as a permanent update to the model. These data actually served as the initiation of a significant update of the FEM to include as much information as possible about the known mass properties of the physical model into the working FEM.

As the model was constructed in the NASA Composite Model Shop, each component was carefully weighed before being integrated into the model. These measured weights are shown in Table 3-3. In addition, each component was systematically removed from the FEM and run through the NASTRAN mass properties analysis module. The results of these analyses are also shown in the table. As can be seen, the largest discrepancy in the experimental and theoretical weights are in the fuselage beam, mounting feet, the nacelle hard points, the flap drive and the foam cores. Each of the components in Table 3-3 were corrected in the FEM to correspond to the weight of the physical model. In the case of the foam cores, the density of the foam was modified to result in a core weight that was the same as the experimental weight. The weight of the remaining components was tuned by adding a nonstructural mass, positive or negative, to the component.

Table 3-4 shows the FEM tuned mass and C.G locations for each of the components in Model 17-5. For completeness, the original weight and C.G. locations for Model 16-6 are also displayed. Each component weight in model 17-5 is now very close to its corresponding experimental value. The largest change in mass was for the fuselage beam. This beam was originally modeled after the beam used in the HSR Rigid Semispan Model (HSR-RSM). Significant material was removed from the physical FSM beam to facilitate improved routing of instrumentation wiring, thus explaining the large discrepancy in weight. In addition to tuning the beam for weight, its streamwise C.G. location was measured, and the FEM was also tuned to this value.

Table 3-3. Physical and analytical model component weight comparison

Component	Measured Weight (lb.)	Model 16-6 NASTRAN Weight (lb.)	ΔW (NASTRAN-Meas.)
Fuselage Beam	92.5	104.6	12.1
Aft Mounting Foot	21.32	27.29	5.97
Mid Mounting Foot	9.00	10.15	1.15
Forward Mounting Foot	6.50	5.62	-0.88
Nacelle Hard Points	1.65	0.0	-1.65
Flap Drive Hardware	3.25	0.0	-3.25
Foam Cores	21.975	25.99	4.02
Inboard Nacelle	7.2	7.3	-0.1
Outboard Nacelle	6.31	7.3	-0.99
Skins	-	9.97	-
Ballast Masses	86.21	86.21	0.00
Inboard Flap	0.96	1.11	.15
Outboard Flap	0.72	0.79	0.07
Wing Tip Cap	~ 0.6	0.18	-0.42
Spars and Root Rib	1.31	1.42	0.11

Table 3-4. Tuned and original FEM component weight and C.G. locations

Component	Tuned FEM (Model 17-5)				Original FEM (Model 16-6)			
	Weight (lb.)	X _{C.G.} (FS)	Y _{C.G.} (BL)	Z _{C.G.} (WL)	Weight (lb.)	X _{C.G.} (FS)	Y _{C.G.} (BL)	Z _{C.G.} (WL)
Fuselage Beam	92.50	165.29	3.0	18.25	104.60	160.61	3.0	18.41
Aft Foot	21.32	193.78	8.74	17.66	27.29	193.29	4.74	17.52
Mid Foot	9.00	150.77	6.35	18.62	10.15	150.19	4.74	18.65
Forward Foot	6.50	114.85	5.72	19.88	5.62	107.74	4.74	20.11
Nacelle Hard Pts.	1.65	201.10	22.82	18.74	0.00	-	-	-
Flap Drive Hdw.	3.25	204.17	15.08	18.07	0.00	-	-	-
Foam Cores	21.98	171.99	20.02	18.69	25.99	172.48	18.57	18.61
Inboard Nacelle	7.20	210.92	16.55	14.00	7.30	210.92	16.55	14.00
Outboard Nacelle	6.31	209.56	30.05	15.56	7.30	209.56	30.05	15.56
Skins	11.46	180.25	24.26	18.77	9.97	178.94	23.68	18.75
Ballast Masses	86.21	171.85	19.12	18.57	86.21	171.85	19.12	18.57
Inboard Flap	0.98	210.05	10.05	17.57	1.11	210.17	10.06	17.57
Outboard Flap	0.69	209.24	23.56	19.06	0.79	209.35	23.57	19.06
Wing Tip Cap	0.60	214.82	63.10	19.25	0.18	214.72	63.05	19.25
Spars and Root Rib	1.32	160.88	17.60	18.82	1.42	157.24	12.7	18.75

The skins were not weighed prior to assembly of the model due to the fact that they could not be removed from their aluminum molds without risk of damage. The skin densities for the various lay-ups were computed using coupon samples of known area, thickness and weight representative of each section of the wing. Three layer, six layer and seven layer samples for the wing skins are available, as well as a four layer sample of the material used to construct the leading and trailing edges, and the wing tip cap. The adhesive used to bond the foam core halves, the skins to the core and the lead weights to the core was also weighed and evenly distributed over the area of the wing. These values were used to correct the skin density applied in the FEM.

The wing tip cap was originally modeled simply as part of the outer wing panel. In reality, it was composed of the same shop glass used to construct the leading and trailing edge components. There was also a phenolic instrumentation holder embedded in the tip cap that added weight. Unfortunately the tip cap was not weighed before it was instrumented and installed on the model.

However the tip cap for the Rigid Semispan Model (RSM) was very similar in construction to the FSM tip cap, and it weighed approximately 0.6 lb. Therefore this weight was used for the FSM tip cap. The tip cap representation in the FEM was chosen as the most outboard chordwise row of elements, and the material properties for these elements were changed to that of the shop glass used in the construction of the leading and trailing edges. This resulted in a tip cap that was slightly light, so a small nonstructural mass was distributed over the tip cap elements to bring the weight up to the approximate measured weight of the cap. The weight of the skins and the wing tip cap, along with the impact of instrumenting the model are the only areas where significant questions can be raised concerning the mass of the FEM.

The weight and balance of the physical model was checked immediately before the initiation of the free-free GVT. The configuration during these tests did not include the flaps, shaft and actuator hardware, the fuselage beam or the engine nacelles. A NASTRAN model for this configuration was developed and named 17-5ff. Table 3-5 compares the weight and C.G. locations for this analytical model with those of the physical model. Model 17-5ff is 5.8 lb. lighter than the physical model which can be attributed to the weight of the instrumentation and wiring in the physical wing. The fuselage stations of the C.G. compare very well between the two models as do the butt line stations.

Table 3-5. Weight and C.G. locations for the HSR-FSM free-free GVT configuration

Configuration	Weight	X _{C.G.}	Y _{C.G.}	Z _{C.G.}
Physical Model	165.85	172.33	17.35	-
Model 17-5ff	160.05	172.27	17.16	18.54
Model 17-6ff	165.81	172.37	17.32	18.55

The instrumentation and wiring was not modeled in the FEM, and it was difficult to develop accurate strategies for including its mass into the model. For this reason, the density of the foam core and the wing skins was uniformly increased to force the FEM weight to match that of the physical model. This spread the weight of the wiring over virtually the entire wing surface, which was a reasonable approximation to the actual physical distribution of weight. These results are displayed as Model 17-6ff in the table. In addition to improving the weight correlation of the FEM, the fuselage station and butt line for the analytical C.G. matched the physical model C.G. well within the laboratory measurement tolerances.

The physical model pitch and yaw moments of inertia were also estimated in the laboratory. These values are compared to analytical values in Table 3-6. The analytical model slightly over predicts both the pitch and yaw inertias. The analytical pitch inertia is 3.3% higher than the experimental value while the yaw inertia is 9.3% higher. Given the experimental setup and the conversions and corrections which were required to obtain the experimental values, these differences were viewed as acceptable, and no further corrections to the mass distribution in the analytical model were performed.

**Table 3-6. Pitch and yaw moments of inertia for the HSR-FSM
free-free GVT configuration**

Configuration	I_{yy} (lb.-in. ²)	I_{zz} (lb.-in. ²)
Physical Model	1.003×10^5	1.098×10^5
Model 17-6ff	1.036×10^5	1.200×10^5

The analytical weight and C.G. location for the assembled model is shown as configuration 17-6 in Table 3-7. This model includes all components from the fuselage beam outboard, as well as the balance, L-bracket and pedestal which are currently modeled as weightless elements. Model 16-6 was the last fully analytical configuration. In other words, configuration 16-6 contains no measured mass properties. Significant changes were made to the mass of the model and its distribution. Model 17-6 was 11 lb. lighter than model 16-6 and the C.G. moved aft and outboard on the wing. The outboard shift of the C.G. is especially important since this had a direct impact on the wing first bending frequency.

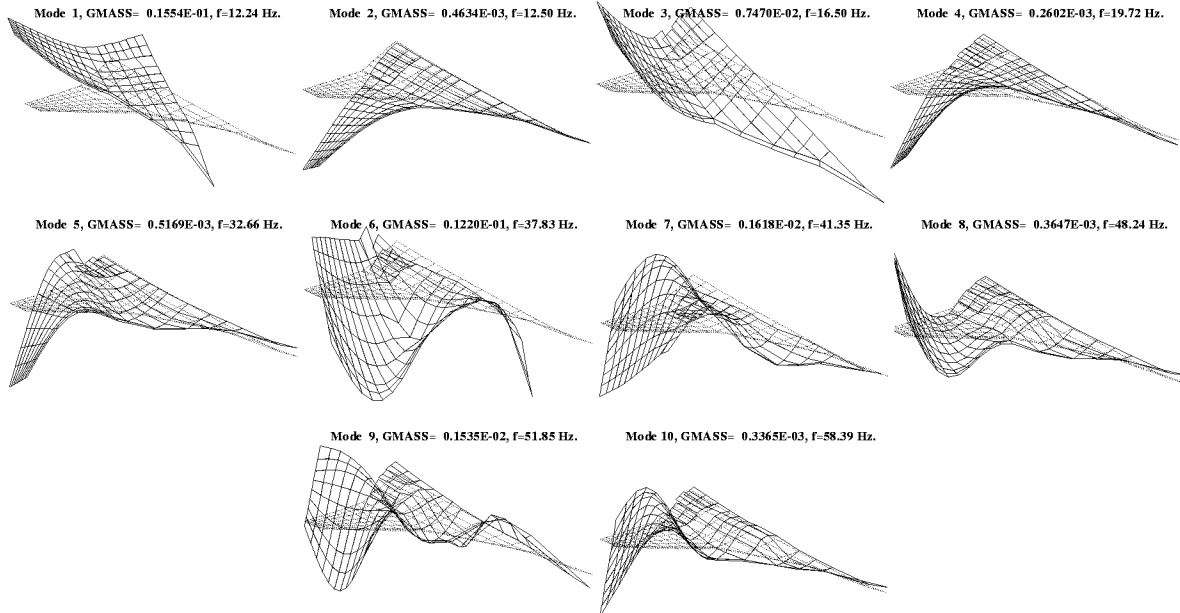
Table 3-7. Analytical weight and C.G. locations for the HSR-FSM

Configuration	Weight	$X_{C.G.}$	$Y_{C.G.}$	$Z_{C.G.}$
Model 16-6	287.93	169.91	11.38	18.26
Model 17-6	276.91	172.48	12.77	18.25

3.3.3 Dynamic Characteristics

Ultimately we were most interested in the effect of these mass changes on the dynamics of the wing. A final comparison between the natural mode shapes and frequencies of models 16-6 and 17-6 provides insight into this subject. Figure 3-7 compares the mode shapes and frequencies for these two models. In model 17-6, the lowest frequency mode is the wing first bending mode, and its frequency was reduced by more than 1.6 Hz., from 12.68 Hz. for model 16-6 to 11.01 Hz. for model 17-6. The rigid body pitch mode frequency also changed significantly. This is due to the aft shift in the C.G location of the fuselage beam, making its C.G. closer to the balance mounting point. Modes 4 through 6 are the remaining modes which participated heavily in previous flutter analyses. In general, the frequencies for these modes decreased due to the modeling changes discussed above, with mode 4 much closer to the balance pitch mode.

NASTRAN Mode Shapes HSR-FSM Model 16-6



NASTRAN Mode Shapes HSR-FSM Model 17-6

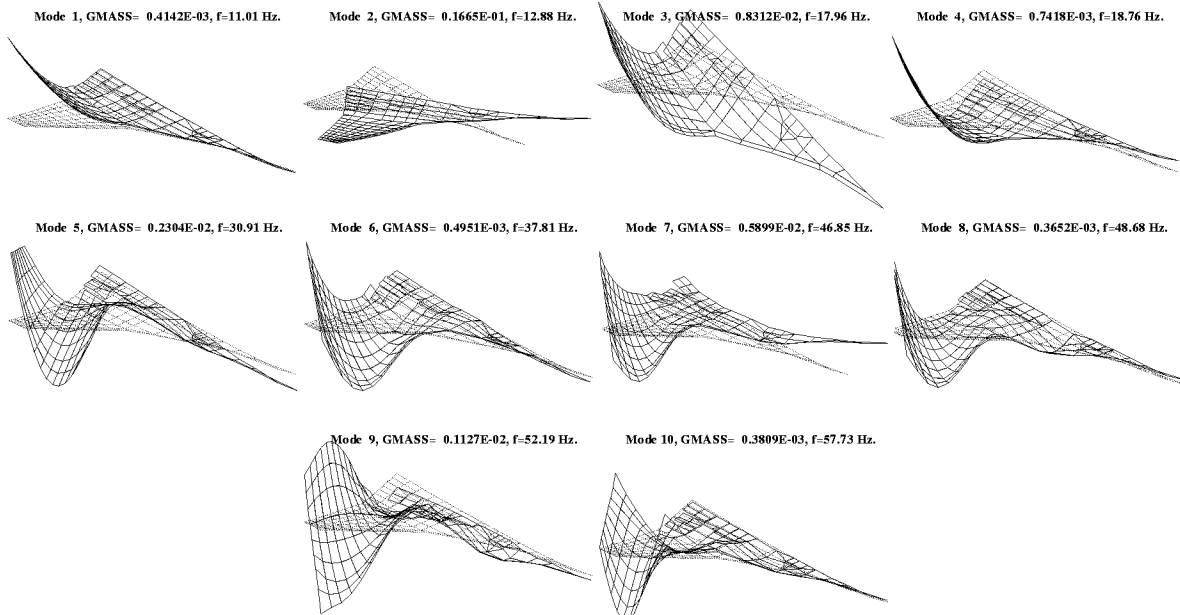


Figure 3-7. Comparison of dynamic characteristics of models 16-6 and 17-6.

3.4 Final Flutter Configuration FEM Development.

Once construction of the HSR-FSM physical model was completed, several laboratory tests of the model were performed before its installation in the TDT. Both a free-free GVT and a GVT with the model support structure mounted to a strong-back were accomplished. In addition, static load tests on the model were also performed. Results of these tests are summarized in subsequent sections of this report.

The static loads testing allowed us to evaluate the FEM stiffness by correlating structural deflections due to known loads with those measured in the laboratory. The bending and torsional stiffness properties of models 18-2 and 18-3 were updated based on data obtained from these static load tests. The outboard wing of the FEM was found to be too flexible in bending as compared to the test data. To correct this, the skin's composite elastic modulus (E_{11} and E_{22}) and shear modulus (G_{12}) in model 18-2 were both increased by 35% on the outboard section of the wing. Torsional loads data showed that these values made the wing too stiff in torsion, and therefore, the shear modulus was reduced back to its original value in model 18-3. The bending and torsional deflections computed using model 18-3 compare very well with the bending and torsional laboratory data.

Finally, static loads data taken on the model support structure were used to update the support structure modeled in the FEM. Preliminary data was used to correct the support structure approximation in model 18-1, and these values were finalized in model 18-5. The final configuration used to predict the flutter of the model in the TDT is model 18-5eotm which is the 18-5 configuration with the engines removed and a 2.5 lb. weight embedded in the wing tip trailing edge. The dynamic and flutter characteristics of this configuration are discussed in section 7.0 Flutter Analysis.

4.0 Ground Vibration Testing

The objective of the ground vibration test (GVT) was to measure the modal characteristics of the FSM. The measured mode shapes and frequencies were then used to tune the NASTRAN FEM which in turn formed the basis for flutter analyses for the TDT wind-tunnel test. Vibration testing was first conducted in a free-free configuration suspended on bungee cords. Then tests were conducted with the model mounted to a backstop, and final tests were performed in the TDT flutter-test configuration.

A sketch of the wind-tunnel model and support system is shown in Figure 4-1. A photo of the wing and the support system mounted to a backstop in the calibration lab is shown in Figure 4-2.

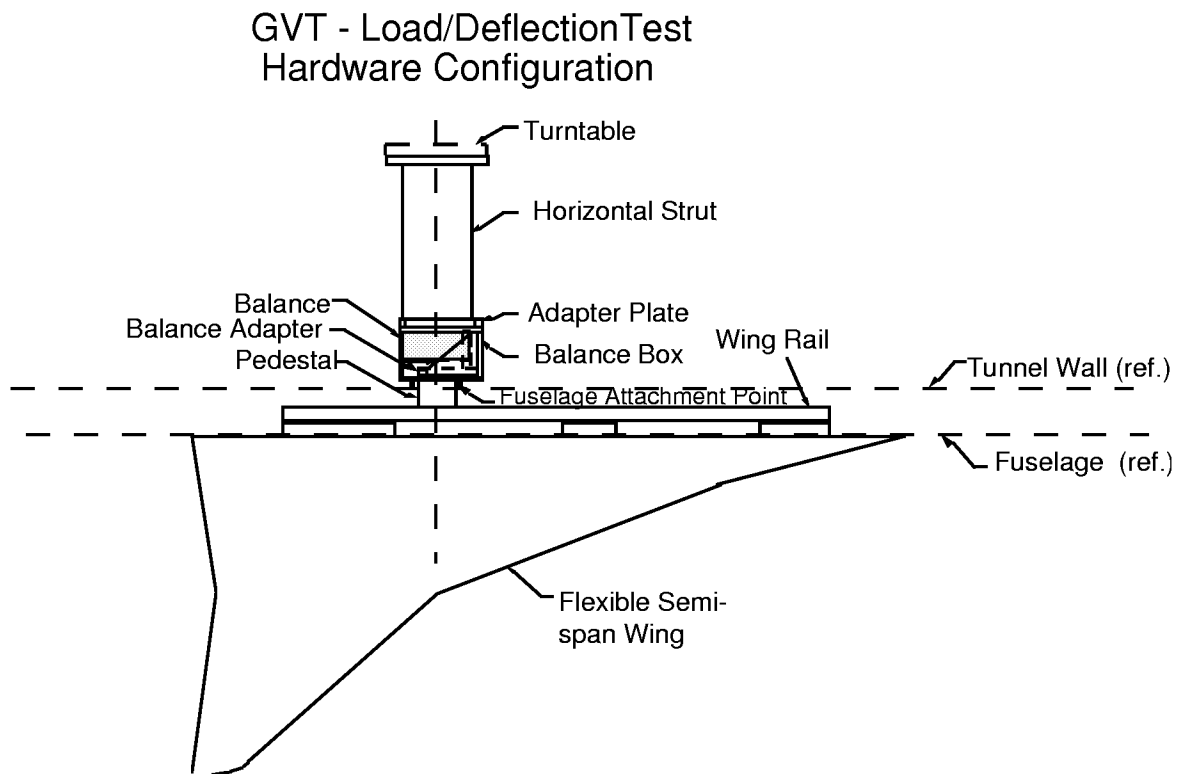


Figure 4-1. Sketch of FSM and support system.

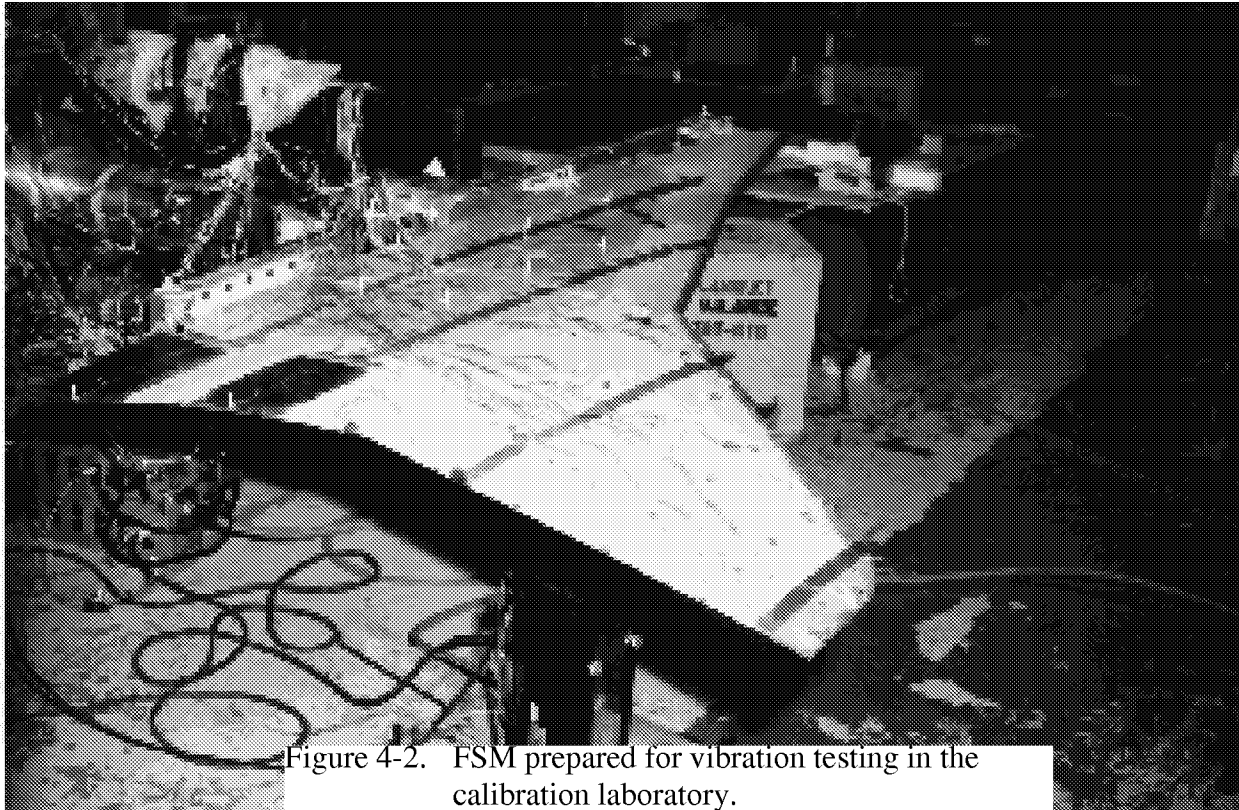


Figure 4-2. FSM prepared for vibration testing in the calibration laboratory.

Listed below are the configurations for which electronic data was previously furnished to NASA and the HSR industry partners. The filenames of the corresponding SDRC/I-DEAS Universal files are in parenthesis. These files contain modal frequencies, damping and mode shapes.

a. Calibration Lab Configurations:

Wing and support system including the balance mounted to a backstop:

1. Engine nacelles off (engoffn.unv).
2. Engine nacelles off plus 2.2 lb. tip weight (engoffwn.unv).
3. Engine nacelles on (engonn.unv).
4. Engine nacelles off plus fuselage (fengoffn.unv).

b. TDT Configuration:

Wing and support system including the fuselage and dummy balance mounted to the retractable turntable (flutter-test configuration):

1. Engine nacelles off plus 2.5 LB tip weight (tdtzn.unv).

4.1 Instrumentation and data acquisition

The excitation system consisted of a single 76-pound electromagnetic shaker and a power amplifier. The primary instrumentation consisted of a force transducer in the excitation drive line and accelerometers. Accelerometer locations are defined in Table 4-1 and shown in Figure 4-3. Accelerometers were placed at the finite element nodes with the exception of the driving point location (point 1, lower surface) and the fuselage accelerometers (points 958 & 975). The grid numbers and coordinates were taken directly from the FEM. An HP front end and SDRC I-DEAS² software package were used to generate the forcing excitation signals, acquire data, and perform the modal analysis.

Table 4-1. Coordinates for accelerometer locations

Grid Point	x (in.)	y (in.)	z (in.)	Remarks
1	198	40	18.8	Drive point
112	108.7	3	20.081	Wing rail
132	203.74	3	17.4	Wing rail
1241	175.306	3	17.835	Wing rail
1245	175.306	-24	17.835	Strut base
10102	106.789	6.49	21.73	
10105	151.362	6.49	21.132	
10107	178.799	6.49	20.083	
10111	204.11	6.49	18.602	
10201	127.619	14.628	17.563	
10202	130.669	12.47	19.909	
10204	151.362	12.47	20.374	
10205	165.987	12.47	20.291	
10206	178.799	12.47	19.99	
10208	190	12.47	19.488	
10210	204.11	13.95	18.637	
10212	218.85	13.95	18.087	
10310	204.11	20.3	19.457	
10314	217.798	20.3	18.894	
10402	151.362	21.03	19.415	
10403	165.987	21.03	20.101	
10404	178.799	21.03	20.255	
10406	190	21.03	20.206	
10501	164.882	29.341	18.137	
10502	165.987	27.08	19.253	
10602	178.799	32.38	19.487	
10604	190	32.38	19.971	
10606	206.175	32.38	20.308	
10608	215.737	32.38	20.054	
10801	183.102	40.02	18.948	
10803	187.072	40.02	19.389	
10805	198.115	40.02	20.085	
10807	209.158	40.02	20.162	
10809	216.682	40.02	19.926	
11001	189.987	46.22	19.085	
11003	193.789	46.22	19.411	
11005	202.688	46.22	20.025	
11007	211.587	46.22	20.088	
11009	217.822	46.22	19.873	
11201	196.872	52.42	19.172	
11203	200.506	52.42	19.557	
11205	207.261	52.42	19.916	
11207	214.015	52.42	19.974	
11209	218.961	52.42	19.772	
11401	203.757	58.62	19.127	
11403	207.223	58.62	19.507	
11405	211.834	58.62	19.68	
11407	216.444	58.62	19.746	
11409	220.101	58.62	19.577	
11603	213.94	64.82	19.191	
11607	218.872	64.82	19.292	
40219	219.479	10.22	17.677	Flaperon
40519	217.239	23.65	19.349	Flaperon

Table 4-2. Key laboratory and TDT GVT configurations

Feature	Laboratory Configuration	TDT Flutter Configuration
Engines	Off	Off
Tip mass	2.2 lb. external	2.5 lb. installed
Fuselage	Off	Installed
Mounting Hardware	Balance	Dummy balance
Mounting Base	Lab. strongback	Retractable turntable

Table 4-3. Measured frequencies and damping for selected configurations

Cal. lab. configuration with 2.2 lb. tip mass		TDT configuration with 2.5 lb. tip mass	
Frequency, Hz	Critical Damping	Frequency, Hz	Critical Damping
8.06E+00	1.52E-02	8.51E+00	1.07E-02
9.70E+00	1.32E-02	1.05E+01	1.20E-02
1.53E+01	1.05E-02	1.41E+01	2.26E-02
1.89E+01	8.63E-03	1.77E+01	1.67E-02
3.22E+01	6.79E-03	1.85E+01	2.35E-02
3.44E+01	1.06E-02	1.96E+01	9.75E-03
4.24E+01	1.32E-02	2.44E+01	1.91E-02
4.93E+01	1.20E-02	3.12E+01	1.59E-02
5.38E+01	9.27E-03	3.95E+01	1.72E-02
5.95E+01	1.39E-02	4.23E+01	9.38E-03
		5.05E+01	1.44E-02
		6.19E+01	1.43E-02

4.4 Test and Analysis

Corresponding to these hardware configurations are two FEM versions. For the laboratory FEM, the elastic and shear moduli of the outer wing skins were increased by 35% over the original coupon values for reasons discussed previously. Also, the mounting structure mass and stiffness were based on a laboratory test of that structure.

For the TDT flutter FEM, an additional adjustment was made to the outer skins: the skin shear moduli were returned to the coupon values, leaving only the elastic moduli values “stiffened” as in the laboratory configuration. In addition, the modeling of the mounting structure was further refined. Finally, mass properties of the fuselage were added to the FEM. The retractable turntable was not modeled and assumed rigid in the FEM.

Figure 4-4 gives frequencies and node line plots of the test vibration modes for the laboratory configuration. Figure 4-5 shows both node line and perspective plots for the corresponding FEM. Despite the complexities, nonlinearities and uncertainties of the wing and mounting hardware, these plots indicate very good agreement through the 42 Hertz range.

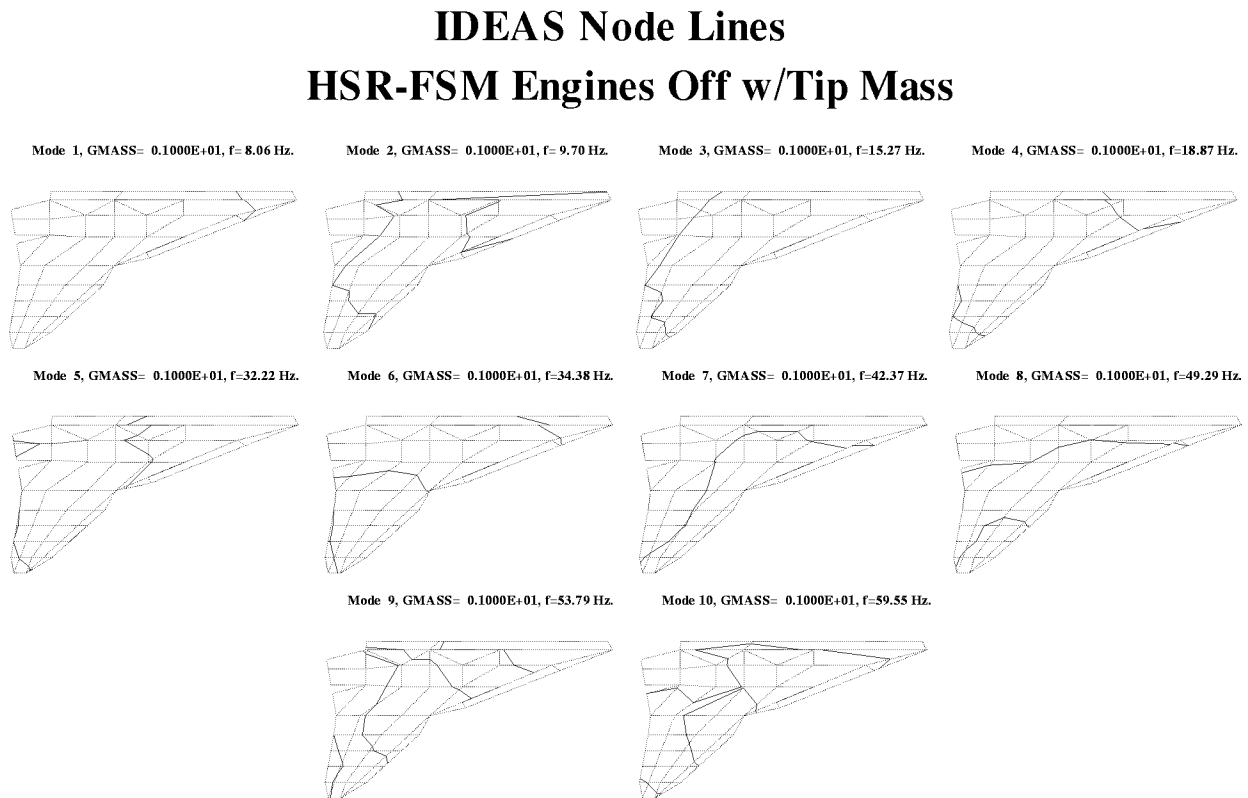
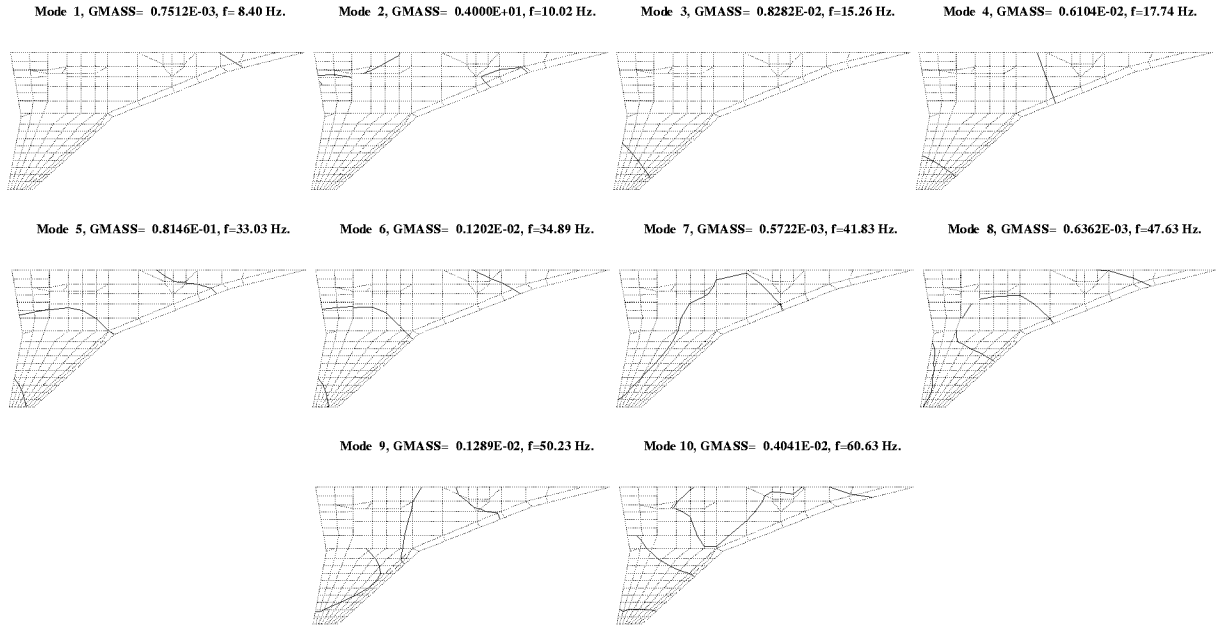


Figure 4-4. Experimental vibration frequencies and node lines for the laboratory configuration.

NASTRAN Node Lines HSR-FSM Model 18-2WNE



NASTRAN Mode Shapes HSR-FSM Model 18-2WNE

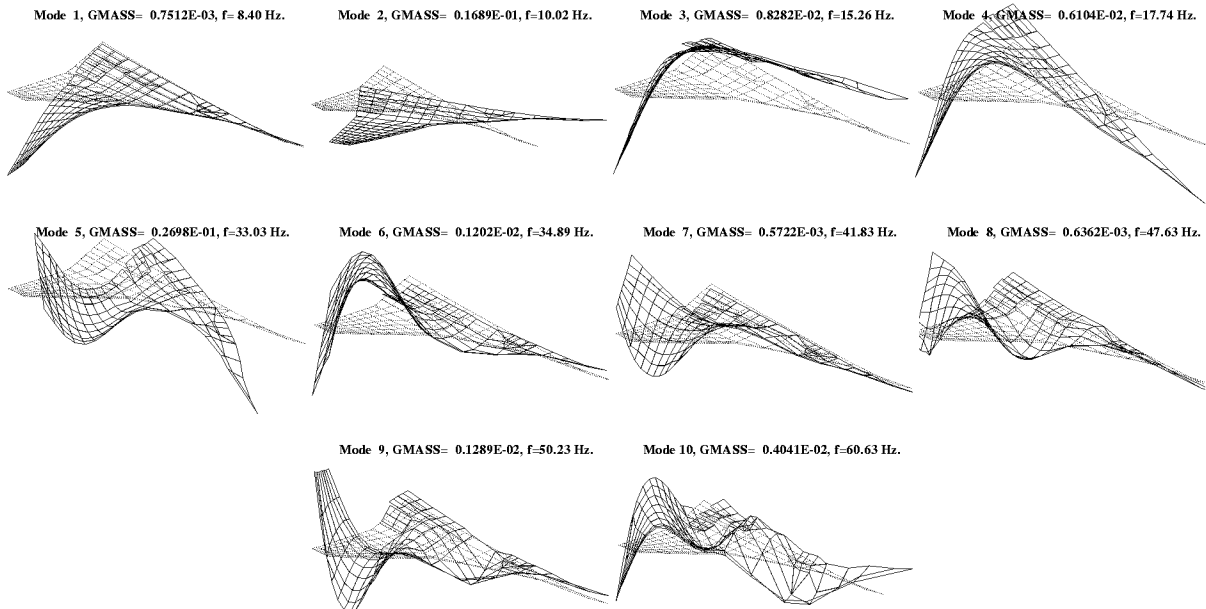


Figure 4-5. Analytical frequencies and mode shapes for the laboratory configuration.

Similarly, Figure 4-6 and Figure 4-7 provide comparison information for the TDT flutter configuration. The more complex TDT configuration (i.e. with the addition of the dummy balance, fuselage and retractable turntable) have rendered mode comparisons more difficult. A list of modal frequencies and comments pertaining to comparisons of test and FEM results is presented in Table 4-4.

Table 4-4. Comparison of test and analysis modes shapes

Test, Hz.	FEM, Hz.	Comment on comparison
8.51	8.42	Good.
10.48	10.2	In-plane mode, good.
14.14	14.18	More in-plane motion in test than FEM. Probably due to retractable turntable.
17.68	None	Could be due to fuselage, turntable or dummy balance.
18.5	None	Could be due to fuselage, turntable or dummy balance.
19.56	18.28	Good.
24.38	None	Could be due to fuselage, turntable or dummy balance.
31.23	29.8	Less in-plane motion in test than FEM.
39.53	34.46	Similar shape, large difference in frequency.
42.31	38.23	Similar shape, large difference in frequency.

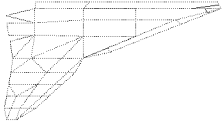
4.5 GVT Summary

The laboratory GVT data described above represented the best information available when preparing for flutter testing. However, the TDT set up imposed necessary changes that were not fully understood or modeled mathematically. These changes were 1) addition of the fuselage, 2) replacement of the actual balance used in the loads portion of the wind-tunnel test with a stiffer dummy balance, and 3) mounting of the entire structure on the retractable turntable. Even so, for modes likely to participate in flutter, the finite element model still gave reasonable results. Section 9 (flutter analysis) describes how the GVT data was used in the pre- and post-test flutter analyses.

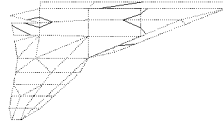
IDEAS Node Lines

TDT Flutter Configuration

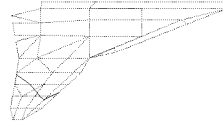
Mode 1, GMASS= 0.1764E-05, f= 8.51 Hz.



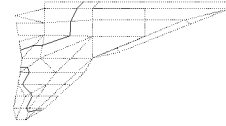
Mode 2, GMASS= 0.1264E-04, f=10.48 Hz.



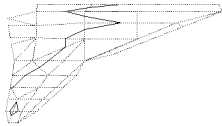
Mode 3, GMASS= 0.1793E-04, f=14.14 Hz.



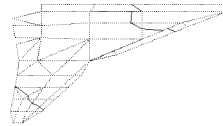
Mode 4, GMASS= 0.5569E-04, f=17.68 Hz.



Mode 5, GMASS= 0.1976E-04, f=18.50 Hz.



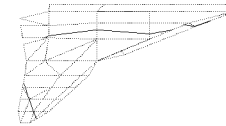
Mode 6, GMASS= 0.5257E-04, f=19.56 Hz.



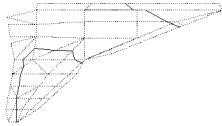
Mode 7, GMASS= 0.2000E-03, f=24.38 Hz.



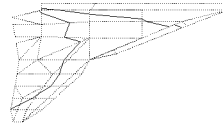
Mode 8, GMASS= 0.8477E-05, f=31.23 Hz.



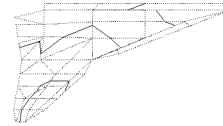
Mode 9, GMASS= 0.2472E-05, f=39.53 Hz.



Mode 10, GMASS= 0.5260E-06, f=42.31 Hz.



Mode 11, GMASS= 0.4885E-04, f=50.53 Hz.



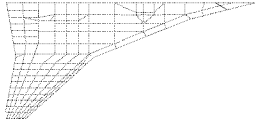
Mode 12, GMASS= 0.3523E-05, f=61.90 Hz.



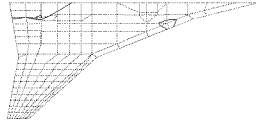
Figure 4-6. Experimental frequencies and node lines for flutter configuration.

NASTRAN Node Lines
TDT Flutter FEM

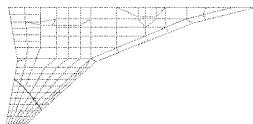
Mode 1, GMASS= 0.7462E-03, f= 8.42 Hz



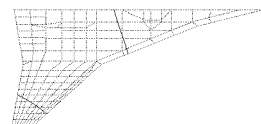
Mode 2, GMASS= 0.8097E+01, f=10.20 Hz



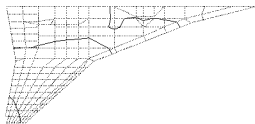
Mode 3, GMASS= 0.6687E-02, f=14.18 Hz



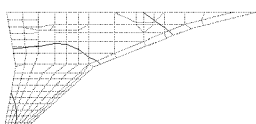
Mode 4, GMASS= 0.5426E-02, f=18.28 Hz



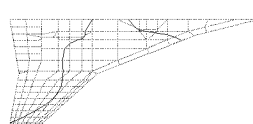
Mode 5, GMASS= 0.1868E+01, f=29.80 Hz



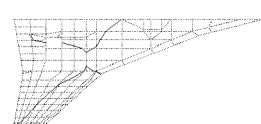
Mode 6, GMASS= 0.9391E-03, f=34.46 Hz



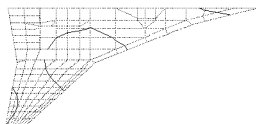
Mode 7, GMASS= 0.1343E-02, f=38.23 Hz



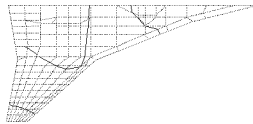
Mode 8, GMASS= 0.4411E-03, f=40.07 Hz



Mode 9, GMASS= 0.1213E-02, f=47.27 Hz

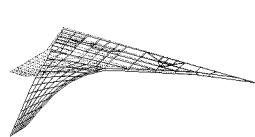


Mode 10, GMASS= 0.7270E-03, f=49.57 Hz

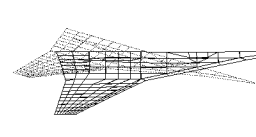


NASTRAN Node Lines
TDT Flutter FEM

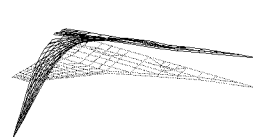
Mode 1, GMASS= 0.7462E-03, f= 8.42 Hz.



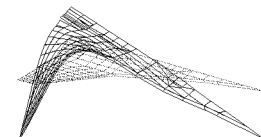
Mode 2, GMASS= 0.1773E-01, f=10.20 Hz.



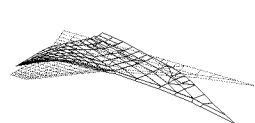
Mode 3, GMASS= 0.6687E-02, f=14.18 Hz.



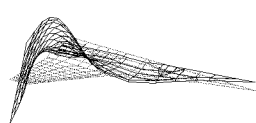
Mode 4, GMASS= 0.5426E-02, f=18.28 Hz.



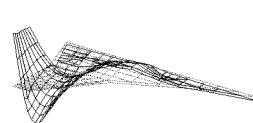
Mode 5, GMASS= 0.3397E-01, f=29.80 Hz



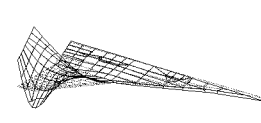
Mode 6, GMASS= 0.9391E-03, f=34.46 Hz



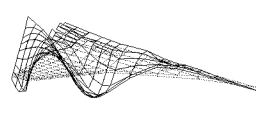
Mode 7, GMASS= 0.1343E-02, f=38.23 Hz



Mode 8, GMASS= 0.4411E-03, f=40.07 Hz



Mode 9, GMASS= 0.1213E-02, f=47.27 Hz



Mode 10, GMASS= 0.7270E-03, f=49.57 Hz

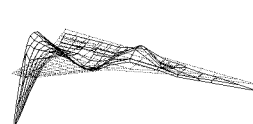


Figure 4-7. Analytical frequencies and mode shapes for flutter configuration.

5.0 Maximum Aerodynamic Load Estimation

An innovative load transferring technique was implemented to apply aerodynamic loads from a CFD model to the FEM structural model of the HSR-FSM. Aerodynamic loads were provided to NASA LaRC Systems Engineering enabling them to perform stress analysis on the proposed wind tunnel model design. This section describes the data and procedures used to simulate aerodynamic loads on the HSR-FSM. Realistic simulations of the maximum anticipated aerodynamic load on this model were required to verify and refine predicted factors of safety. Accurate aerodynamic load prediction allowed a more realistic set of operating limits to be developed before testing, and reduced the test time required to verify these limits. Realistic aerodynamic loads also assisted in avoiding the tendency to be overly conservative when defining operational limits for the tunnel, since we applied an accurate, detailed set of loads on the wing surface rather than an ad hoc, “worst case” loading. Computational Fluid Dynamics (CFD) provided us with the tool to compute these accurate, detailed descriptions of the wing loading at the most extreme test conditions.

Aerodynamic calculations were performed by NASA Langley’s Aeroelasticity Branch using the CFL3D computational aerodynamics code. These calculations were performed on the HSR Rigid Semispan Model (HSR-RSM), which has the same external wing geometry as the HSR-FSM. The HSR-RSM has been previously tested in the TDT, and pressure distributions computed using CFL3D compare well with pressure distributions measured in the TDT. This provided us with a high degree of confidence that the code is capable of accurately predicting the detailed aerodynamic loads on the wing.

From testing and computational experience for the HSR-RSM, we expected the most severe static loading on the wing to occur at a Mach number of 0.95, an angle-of-attack of 6 degrees, and a dynamic pressure of 200 psf in the TDT heavy gas. These were the maximum test conditions for the HSR-RSM in the TDT due to restrictions on the maximum load the force balance could sustain without damage. Obviously, higher angles-of-attack, and dynamic pressures, as well as dynamic testing, would generate higher loads than at these conditions. However, for this series of tests, these parameters represented the most extreme conditions at which we planned to operate the wing. It should also be noted that the computed aerodynamic loads for the HSR-RSM at these operating conditions were somewhat conservative, since they were generated for an effectively rigid wing structure. Static aeroelastic deflection of the HSR-FSM wing was expected to relieve the overall wing loading at these flight conditions.

A CFL3D aerodynamic model and solution file for the HSR-RSM operating at $M=0.95$, and $\alpha=6.0^\circ$ in heavy gas were used to simulate the aerodynamic loading. A NASTRAN finite element model consisting of the external structure grid points and element connectivity was obtained from NASA Langley’s Analysis and Test Engineering Branch. The aerodynamic data consisted of nondimensional density, Cartesian velocity components and total energy at each point in the aerodynamic grid. These data were converted from their nondimensional form into dimensional pressures using the relation:

$$p = 2 \frac{q_\infty}{M_\infty^2} (\gamma - 1) \left(e - \frac{\rho}{2} (u^2 + v^2 + w^2) \right) \quad (5-1)$$

Where ρ , u , v , w , and e are the nondimensional density, Cartesian velocity components and total energy, respectively, q_∞ is the dynamic pressure in psi, M_∞ is the freestream Mach number, and

γ is the ratio of specific heats, which is 1.133 for TDT heavy gas. These pressures were integrated over the wing surface to provide the aerodynamic load on the aerodynamic model.

5.1 Aerodynamic Load Transfer Strategy

At this point, the problem was how to accurately and efficiently transfer the aerodynamic load from its geometric model to the structural model. In general, the aerodynamic and structural models can be drastically different in the number of elements and local geometric resolution. This is illustrated in Figure 5-1 which shows a planform view of the aerodynamic and structural models used in the present analysis. In this case, the aerodynamic grid has a much larger number of grid points, and a

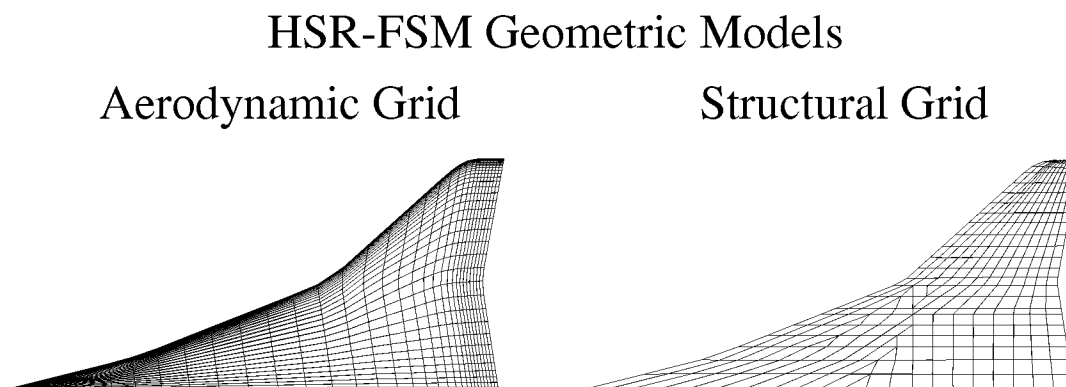


Figure 5-1. Aerodynamic and structural models for the HSR-FSM exhibit significantly different grid resolutions.

great deal of grid clustering is added near the wing leading edge, trailing edge and tip regions, which is not present in the structural model. Also, the two models are topologically different with the structural model consisting of a loosely ordered set of quadrilateral and triangular elements, while the aerodynamic grid is a highly ordered set of elements consisting only of quadrilaterals. These issues complicate the problem of transferring loads from one model to the other.

A straightforward approach to the problem is to simply interpolate the pressures computed on the aerodynamic model to the structural model. However, interpolation can be very difficult for models which have topological and resolution differences. Classical interpolation schemes based on a parameterization of the geometry become especially risky for models which originate from similar, but slightly different, geometric databases. In general, it cannot be assumed, given current modeling techniques, that the aerodynamic and structural models will be derived from the same geometric database. Slight differences between the aerodynamic and structural grids can always be anticipated.

Beyond the difficulties encountered in simply implementing classical interpolation schemes, physical inaccuracies can be significant using this approach. This problem occurs when the aerodynamic model exhibits areas of high grid resolution, while the structural model has correspondingly lower grid resolution. This is typical of leading and trailing edge regions where pressure gradients can be large, forcing the aerodynamicist to resolve these regions with a high density of grid points to properly capture the aerodynamic details. In contrast, structural analyses

require less detail in these areas for accuracy. If straight interpolation of pressure is employed, a great deal of aerodynamic detail which can contribute significantly to the overall load is lost in the transfer from the aerodynamic model to the structural model. In general, this must be viewed as unconservative since the loads on the structural model will often be lower than the actual aerodynamic loads.

A method for overcoming both of the above problems is to simply compute the load on each aerodynamic panel by averaging the pressure on the corners of the panel, multiplying by the panel area, and placing the load at the panel centroid. The structural grid is then searched to identify a group of structural nodes that are “near” the aerodynamic load point. The aerodynamic load is then transferred to this group of nodes using a distance-weighted formula. Using this method, one avoids the complexities presented by implementing classical interpolation schemes since this method only requires that the aerodynamic and structural models be similar, not precisely coincident. In addition, it is assured that the entire aerodynamic load will be transferred to the structure.

Unfortunately, there is still a major problem with this scheme; the aerodynamic moments are not conserved by this method. In fact one cannot even assume that the moments generated by the structural loading will be within a given tolerance level of the aerodynamic moments. This problem is easily countered by computing the moment of the structural loads, due to a given aerodynamic load, about the aerodynamic panel centroid and adding a structural moment of opposite sign to the model. Again, this moment is spread to the structural nodes using a distance-weighted formula. This simply and concisely ensures that all aerodynamic forces and moments will be conserved in the transfer of loads from the aerodynamic grid to the structural grid.

5.2 Load Transfer Methodology

The technique developed for this purpose is described by assuming that the aerodynamic load, L_A , at a given aerodynamic panel centroid, (X_A, Y_A, Z_A) , is transferred to a set of structural loads, L_{S_i} , at structural node points, $(X_S, Y_S, Z_S)_i$, so that:

$$L_{S_i} = W_i L_A \quad (5-2)$$

In this equation W_i represents a set of weights that have the property:

$$\sum_{i=1}^{N_{nodes}} W_i = 1 \quad (5-3)$$

where N_{nodes} is the number of structural nodes within a given group. These weights are determined by the relation:

$$W_i = \frac{\frac{1}{r_i}}{\sum_{j=1}^{N_{nodes}} \frac{1}{r_j}} \quad (5-4)$$

where:

$$r_i = \sqrt{(X_A - X_{S_i})^2 + (Y_A - Y_{S_i})^2 + (Z_A - Z_{S_i})^2} \quad (5-5)$$

This weighting scheme ensures that, within a given group, the structural nodes closest to the aerodynamic loading point receive the largest share of the aerodynamic load, while those farther away receive a proportionately smaller share. When the aerodynamic point and a structural node are directly coincident, Equation 5-4 becomes singular. In this rare case, the structural node simply receives the entire aerodynamic load, which physically is exactly what should happen.

With this background, the load transfer method employed in this analysis can now be discussed. The present technique works with both the structural nodes and the structural model nodal connectivity. In short, the load on each aerodynamic panel is computed and transferred to the structure by first searching the structural model to determine which structural panel's centroid is nearest to the aerodynamic panel centroid. If, for a given aerodynamic panel, a structural panel is selected which contains a node that is identical to the aerodynamic panel centroid, the search is terminated. The aerodynamic load is transferred directly to that structural node and the method continues on to the next aerodynamic panel.

Once the nearest structural element has been identified, the nodes for that element are added to a list of nodes eligible to receive a portion of the aerodynamic load. This list is then traversed a user-specified number of times to determine what other structural panels include the nodes in the list. Each time a structural panel is identified as containing a node in the list, all of the other nodes defining that panel are added to the list. Each time the list is traversed, another layer of structural panels surrounding the "nearest" structural panel become eligible to receive a portion of the aerodynamic load. Thus, this strategy provides a means for spreading a given aerodynamic load over a number of structurally connected panels. This scheme is described graphically in Figure 5-2 for a group of quadrilateral and triangular structural elements.

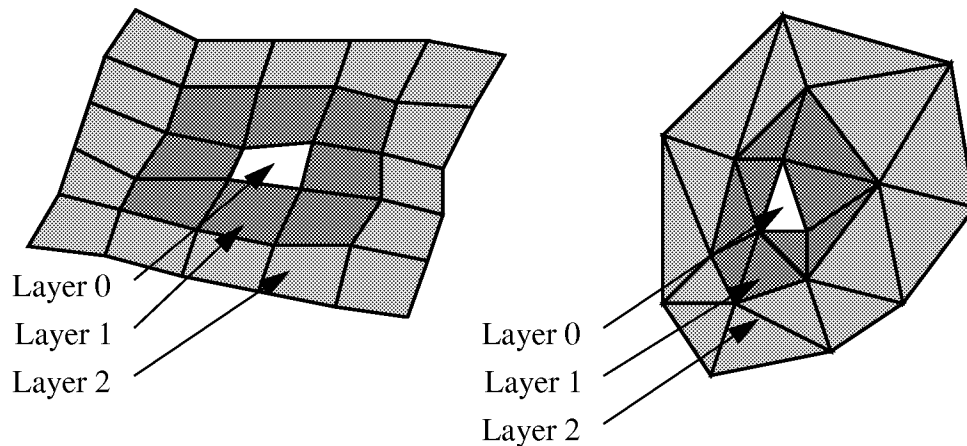


Figure 5-2. The aerodynamic load is spread over a group of structural panels according to a user variable defining the number of layers surrounding the "nearest" structural panel.

nearest structural element to the aerodynamic load point, layer 1 shows the elements that would be added by one pass through the eligible node list, while layer 2 represents the additional elements that would be added by a second pass through the list.

Once all of the eligible nodes have been identified, the aerodynamic load is spread to these nodes using Equations (5-2), (5-4), and (5-5). Once the load has been transferred to the structural nodes, the total moment these loads generate about the aerodynamic load point is computed. The sign is changed on this moment, and the moment is then spread to the structural nodes using the same weighting as used for the aerodynamic force.

The primary result of implementing this technique is to provide a load path through the structure for a given aerodynamic load. If each node in the structural model were completely interconnected a similar scheme could be defined by simply specifying a physical radius within which a given aerodynamic load influences the structure. The current method restricts the load path only to interconnected elements which is physically more realistic than arbitrarily spreading the load to all nodes falling within a given radius.

5.3 Application to the HSR-FSM

The aerodynamic model shown in Figure 5-1 was extracted from the provided CFL3D grid for the entire wind tunnel model and its surrounding flowfield. Pressures on the wing surface were computed from the $M=0.95$, $\alpha=6^\circ$ flowfield data, and the resulting wing surface pressure contours are displayed in Figure 5-3. At each panel in the aerodynamic model, an average pressure was

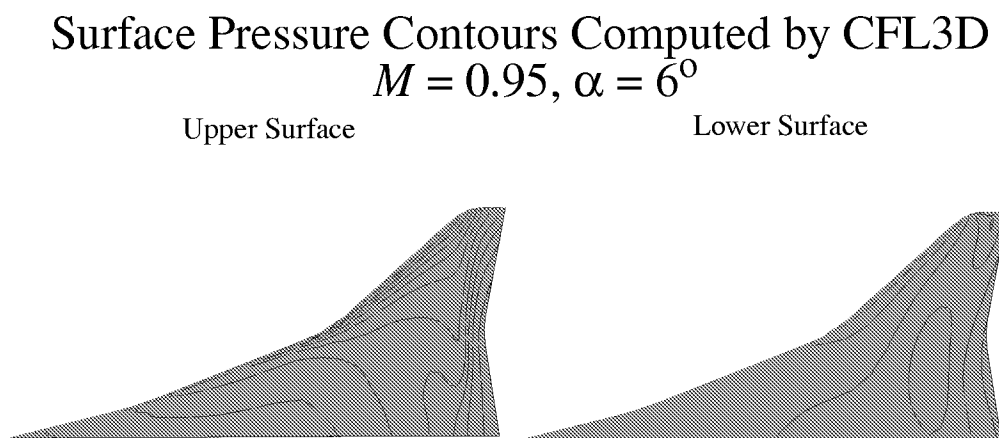


Figure 5-3. Surface aerodynamic pressure distribution used to simulate loads on the HSR-FSM.

computed along with the local panel area, the panel centroid, and a vector normal to the panel. These data provided the necessary information to compute the magnitude and direction of the aerodynamic force acting on the given panel.

The structural model was provided as a NASTRAN input deck composed of a series of quadrilateral and triangular elements. The structural model incorporated in this analysis has been previously presented in Figure 5-1.

The structural loading was computed for a dynamic pressure of 200 psf. Contours of the load applied to the wing structure are presented in Figure 5-4. For the most part, definite patterns in the

structural loading can be identified; though in certain areas, there appears to be some jagged contours and local “hot spots.” This is due to the fact that we are working with the aerodynamic load rather than the aerodynamic pressure, and the load is a function of the local panel area. Changes in grid density both in the structural and in the aerodynamic model affect the distribution of the load on the wing. It is also interesting to note that the contours seem to become discontinuous near the inboard trailing edge of the wing. At first it was thought that there was an

Structural Load Contours $M = 0.95$, $\alpha = 6^\circ$, $q = 200\text{psf}$

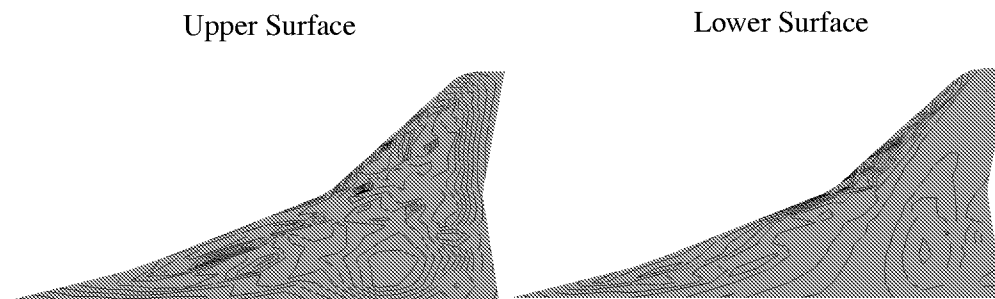


Figure 5-4. Aerodynamic load magnitude contours on the structural model.

error in the load transfer routine, but it was later realized that these discontinuous contours result from modeling the control surfaces in the FEM as disconnected structures from the main wing structure. Therefore, there is no physical load path from the main wing structure onto the control surfaces, and the present load transfer method captures this feature. The only aerodynamic loads that are acting on the control surfaces are those that are applied directly to the control surface itself.

6.0 Static Loads Test

The objective of the static loads test was to acquire and store wing deflection data for the following potential uses.

- a. Tuning and validating the stiffness of the FEM which in turn was used for vibration and flutter analyses.
- b. Evaluating the nonlinearity of the structure with respect to load magnitude and time under load.
- c. Proof testing the wing at maximum static loads anticipated for the wind-tunnel test.
- d. Comparison with and validation of the photogrammetric deflection measurement system.
- e. Calibrating the mid-wing strain gage bridges which were monitored for safety during wind-tunnel testing.

Static testing of the cantilevered wing was performed in the weeks preceding the wind-tunnel test. There were 13 individual test configurations, with up to 30 load stations, 14 measurement stations, and numerous data points representing various loadings and times. Thirteen electronic data files, each representing a test configuration, have been made available to NASA and the industry partners. Table 6-1 provides a summary of these data files.

Table 6-1. Data files for static loads test

File Name	Configuration	Data Type
PL_INV01	14 Deflection Gages. 30 load points, one at a time up to 4° angle-of-attack distributed load.	Stiffness data.
PL_INV02	14 Deflection Gages. 6 outer wing load points, build-up to 4° angle-of-attack distributed load, held for creep info.	Limited stiffness & creep data.
PL_INV03	14 Deflection Gages. 4 outer wing load points, build-up to 4° angle-of-attack distributed load.	Limited stiffness data & photogrammetry set-up info
PL_INV04	14 Deflection gages - 23 Photogrammetry Locations. 4 outer wing load points, build-up to 4° angle-of-attack distributed load.	Limited stiffness data & photogrammetry data
PL_INV05	14 Deflection Gages - MODCOMP Tab Points with 4 Strain Gage Outputs. 5 outer wing load points, build-up to 4° angle-of-attack distributed load.	Limited stiffness data & cal info for in-situ strain gages.

Table 6-1. Data files for static loads test

File Name	Configuration	Data Type
PL_INV06	14 Deflection Gages - 16 Photogrammetry Locations. 10 outer wing load points, build-up to 4 AOA distributed load.	Stiffness data & photogrammetry data.
PL_INV07	14 Deflection Gages - 17 Photogrammetry Locations. 10 outer wing load points, build-up to 4 AOA distributed load.	Stiffness data & photogrammetry data.
PL_INV08	12 Deflection Gages - 23 Photogrammetry Locations. 4 pair of outer wing load points, build-up to 30# for single point and 60# for pair of load points.	Stiffness data & photogrammetry data
PL_INV09	12 Deflection Gages. 2 pair of mid-wing load points, build-up to 30# for single point and 60# for pair of load points.	Stiffness data.
PL_INV10	14 Deflection Gages - 23 Photogrammetry Locations - MODCOMP Tab Points with 4 Strain Gage Outputs. 30 load points build-up to 3° angle-of-attack distributed load.	Stiffness data & Photogrammetry data & cal info for in-situ strain gages.
PL_UP01	14 Deflection Gages - 21 Photogrammetry Locations - MODCOMP Tab Points with 4 Strain Gage Outputs. 5 pairs of outer wing load points, build-up to 30# for single point and 60# for pair of load points.	Stiffness data & Photogrammetry data & Cal info for in-situ strain gages.
PL_UP02	14 Deflection gages - 21 Photogrammetry Locations - MODCOMP Tab Points with 4 Strain Gage Outputs. 29 load points build-up to 0deg distributed load.	Stiffness data & photogrammetry data & cal info for in-situ strain gages.
PL_UP03	11 Deflection Gages - MODCOMP Tab Points. 2 torsion blocks: 1 @ BL 35.15 applied weight build-up to 40#; 1 @ BL 57.2 applied weight build-up to 20#.	Limited stiffness data & cal info for in-situ torsion strain gage.

In this section, selected portions of the data pertaining to objectives a and b will be presented and discussed. The three static loads configurations used here will be (1) point loads with the wing cantilevered upside down (file PL_INV01), (2) three degree angle-of-attack distributed load with the wing cantilevered upside down (file PL_INV10), and (3) torsion block test with the wing right-side up (file PL_UP03).

Figure 6-1 is a photo of the FSM mounted upside down on the strong back. The wing rail was clamped as rigidly as possible to the backstop. The electronic dial gages were mounted at the coordinates of the measurement positions shown in Figure 6-2. Note that the measurement position numbers correspond to the FEM grid point numbers. Point and distributed loads were applied with hooks applied to small pads at the load positions identified in Figure 6-2. Torsion loads were applied with one of two torsion blocks which were clamped across the wing along streamwise chords at span stations 35.15 and 57.2 in. A pulley arrangement was used to apply an upward load on the torsion block just forward of the leading edge, and an equal downward load was applied at an equal distance aft of the trailing edge.



Figure 6-1. FSM loads test hardware.

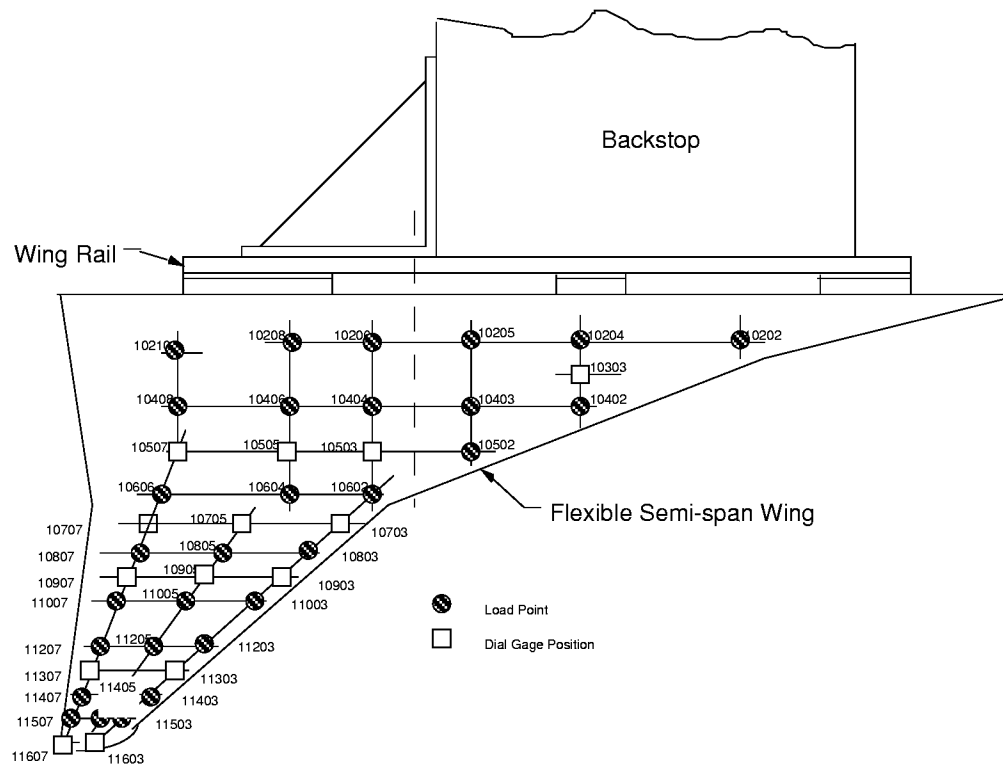


Figure 6-2. Static loads test arrangement.

6.1 Stiffness Nonlinearity and FEM Tuning

The primary purpose of the dynamics FEM discussed here was for predicting vibration frequencies and mode shapes which were in turn used for flutter analysis. Therefore, it was important for the mass distribution to be accurate, and for the stiffness to simulate an instantaneous resistance of the wing to a load. The fiberglass used for the FSM skin carried most of the load and was therefore the primary contributor to stiffness.

Aeroelastic scaling of the FSM led to the selection of Fiberglass 108 which was the thinnest, most flexible skin material identified which could also provide minimum acceptable strength for the wind-tunnel loads. Fiberglass however, is not purely elastic because in addition to instantly deforming when loaded, it tends to gradually “creep” or further elongate with time under load. Technically, the nonlinearity is with respect to both load magnitude and time under load, but the time-dependency was the most obvious and troubling for the FSM.

The objective for tuning the FEM was to adjust skin properties to best simulate the vibration test results. Static testing is useful in accomplishing this because it eliminates uncertainty concerning mass, and gives local deformation measurements to help pinpoint where stiffness may require adjustment. This process however, was complicated by the additional uncertainty of creep.

Material coupon testing is not typically performed in a way that distinguishes between linear and nonlinear displacements. For example, a coupon test for the FSM skin material typically lasted

about thirty minutes which resulted in stiffness data which included instantaneous deformation as well as extensive creep. The resulting material moduli initially used in the FEM were accordingly too flexible for a dynamics model. In the end, moduli were tuned using both static loads and vibration data. For the skin outboard of the break, the elastic modulus was increased by 35%, but the shear modulus was left unchanged. This resulted in reasonable agreement of the FEM with point load displacement, torsion displacement, and vibration frequencies and mode shapes.

6.2 Point Loads Test

A point loads test was used to determine the displacement at each measurement position to a single load applied at each load position. This provides a good measure of wing stiffness which can be compared to the FEM. However, even at the relatively light loadings of the point loads test, creep was apparent.

As an example, Figure 6-3 gives the deflection histories of selected measurement points with loads at point 11503 (refer to Figure 6-2 for point locations). Inboard, mid-span, and tip region displacements are given on separate plots (a, b, c). For comparison purposes, the final FEM results are shown as filled symbols for an 8.3 lb. load. In plot c, results of the FEM analysis with the original coupon skin moduli are also given and are indicated by symbols filled in gray. The hysteresis in the test data is caused primarily by creep. The tuned FEM displacements are in reasonable agreement with the upload cycle and substantially lower than the original FEM results.

An example of creep is presented quantitatively in Figure 6-4. The term creep ratio used here is simply the difference between test and FEM displacements normalized by FEM displacement. The increase in this value during the up and down load cycle is clear evidence that the structure creeps under load. The discontinuity at the second upload point of 3.3 lb. cannot be explained with certainty, but is probably due to some manual movement of the structure during the test. Two additional observations can be made from this data. First, is that for even a relatively lightly loaded condition near the wing tip, creep alone contributed almost 20% of the total displacement. Second, a general discrepancy between various points of the FEM as compared to the recorded test data is also in the 10 to 20% range. FEM points near the wing tip tend to agree with the test data better than those further inboard. It is likely that geometry location errors and measurement errors are more significant on the inboard regions (which have very small displacements).

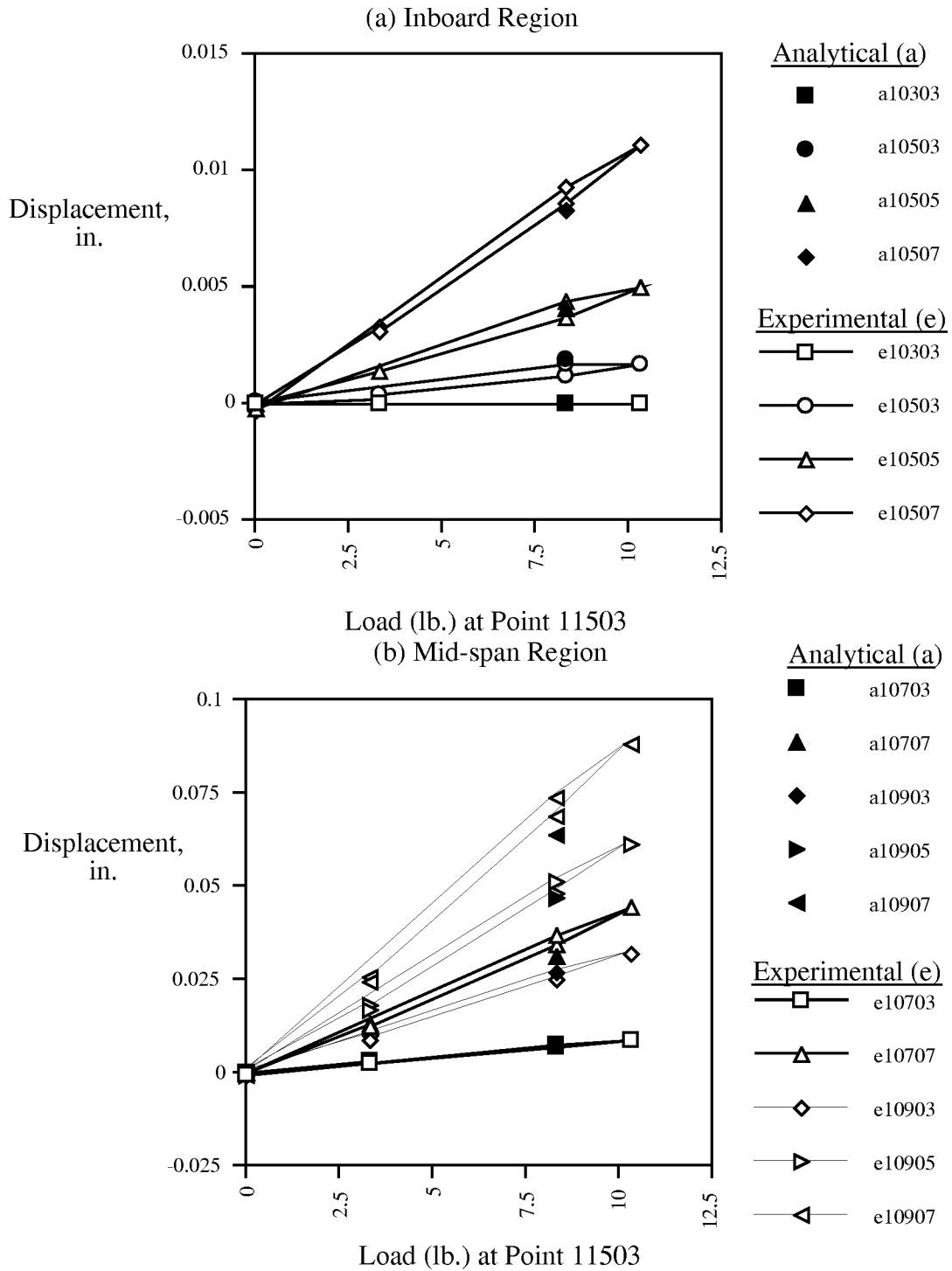


Figure 6-3. Displacements for loads at point 11503.

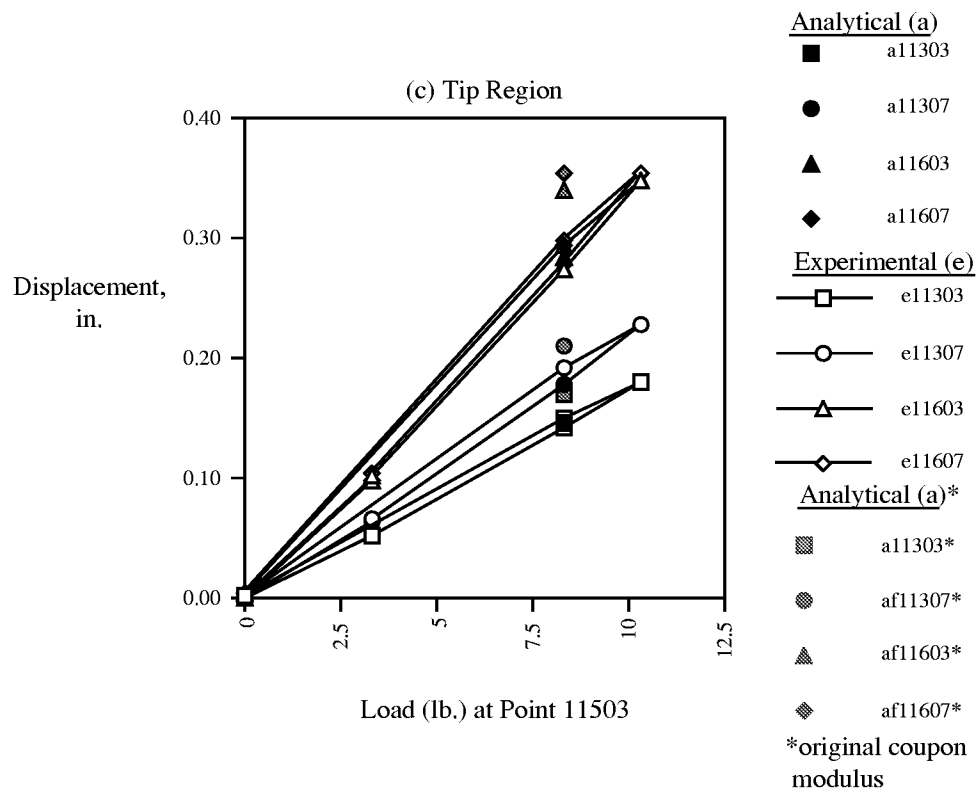


Figure 6-3(Continued). Displacements for loads at point 11503.

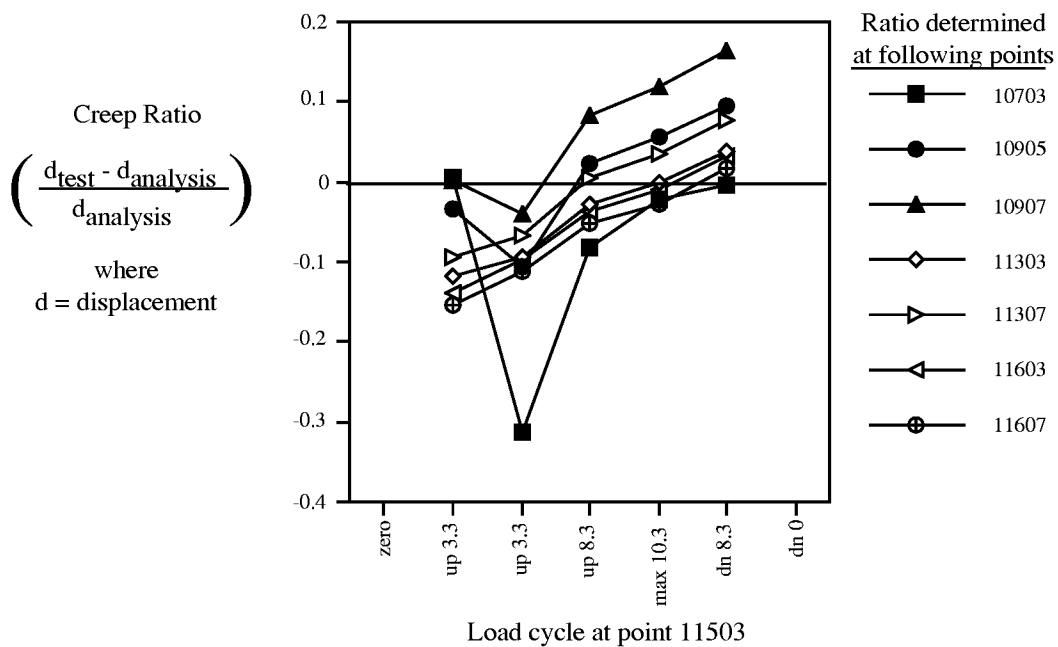


Figure 6-4. Creep ratios for loads at point 11503.

6.3 Torsion Loads Test

Torsion loads displacement data were important in tuning the shear modulus of the skin material. Data from the outboard torsion test will be discussed here. For this test, equal forces of 6.4, 11.4, 16.4 and 21.4 lb. were applied upward on the forward end of the 27.85 inch torsion block, and downward on the aft end. Figure 6-5 gives measured and analytical displacements for selected points on the inboard, mid-span and tip regions (plots a, b, c respectively). Figure 6-6 presents some of the same data as differences between selected point pairs on the leading and trailing edges at the same span stations. This last plot better represents torsion stiffness because it is a direct measure of twist. The solid symbols represent the tuned FEM results for the 11.4 lb. (317.49 in-lb. torsion) case. As with the point loads, hysteresis can be observed. The largest discrepancy for the FEM is the differential displacement of points 11603 and 11607 at the wing tip.

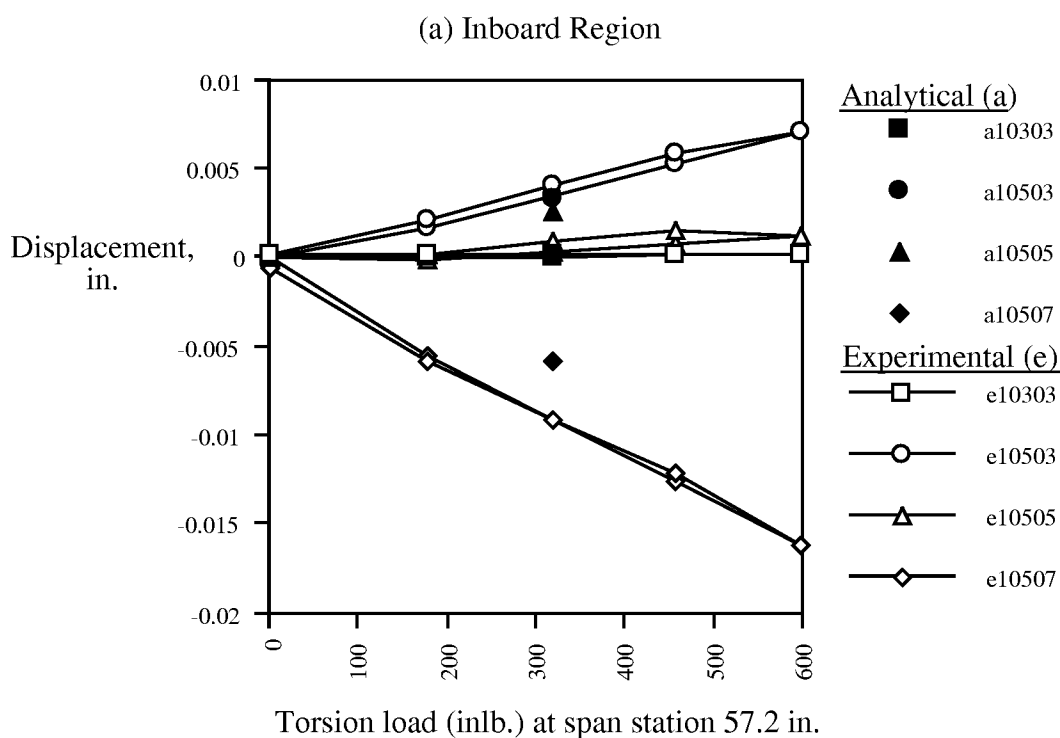


Figure 6-5. Displacements for torsion loads.

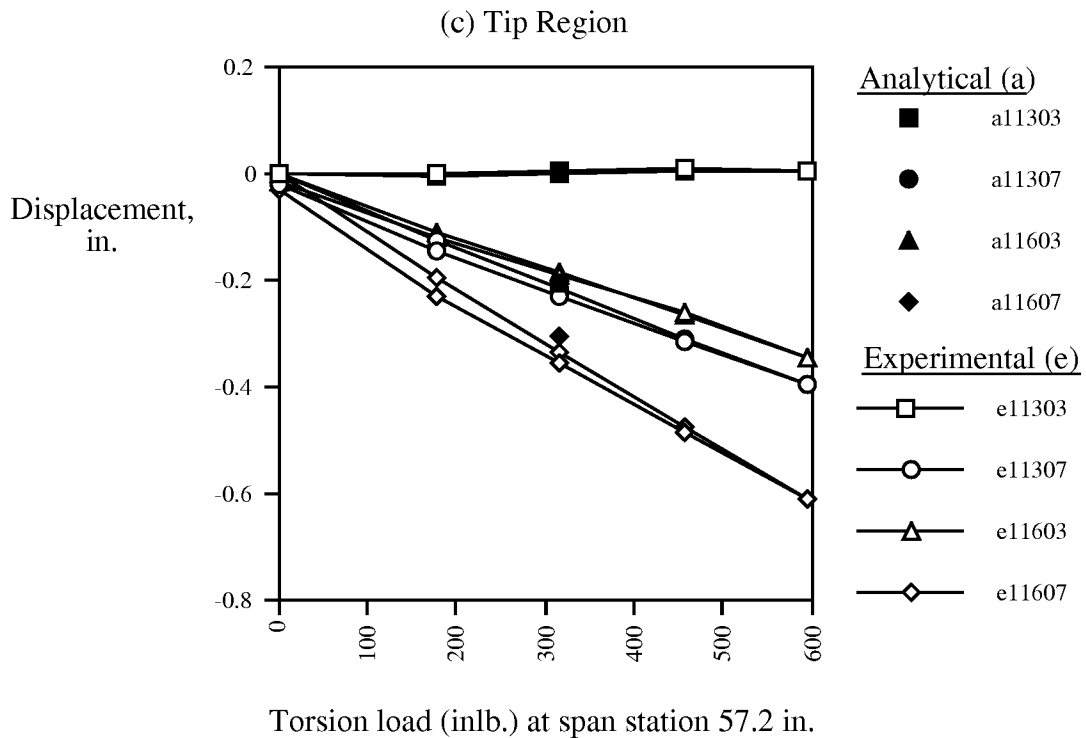
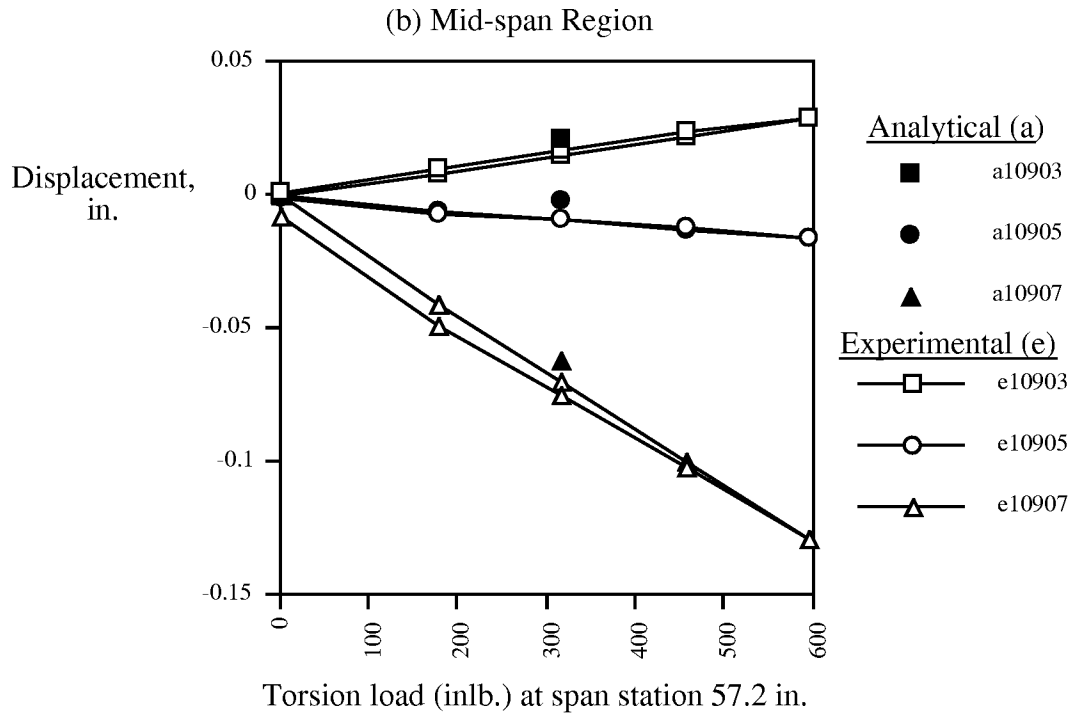


Figure 6-5 (Continued). Displacements for torsion loads.

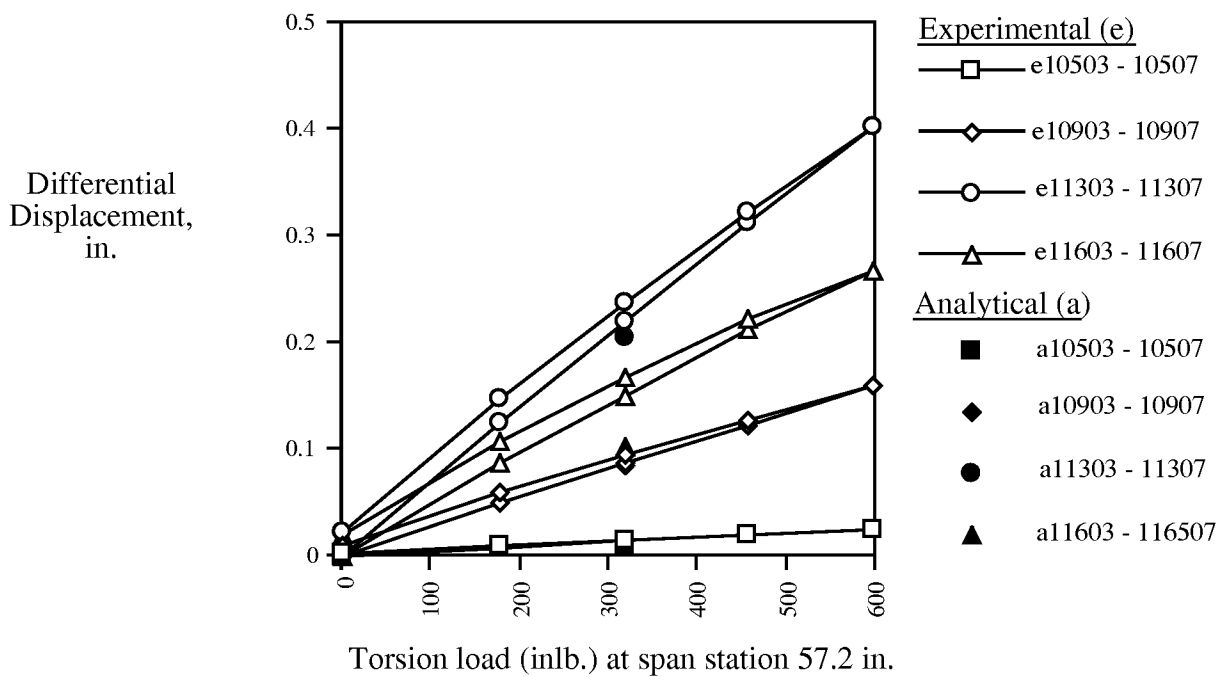


Figure 6-6. Differential displacements of leading and trailing edge points for torsion loads.

6.4 Distributed Loads Test

The main purpose of the distributed loads tests was to ensure that the wing was structurally sound under these loading conditions. Therefore, distributed loads tests were performed for loads predicted at zero and three degrees angle-of-attack for Mach 0.95 with dynamic pressure of 200 psf. These conditions represented the most severe loading conditions anticipated during wind tunnel testing. The loads were based on CAP-TSD³ calculations which included structural flexibility effects, and were applied in the same manner as for the point loads test. Table 6-2 gives the calculated and actual test loads for these conditions.

Selected data from the 3 AOA loading case will be presented here. Table 6-3 lists selected load conditions for the load cycle. Data from the inboard, mid-span and tip regions are given in plots a, b, and c respectively of Figure 6-7. Also shown are the corresponding analytical deflections from the tuned FEM. The FEM appears much stiffer than the physical model, and diverges more as the test progresses. As with the previous data, this discrepancy is primarily due to creep, and the test data does not represent the instantaneous stiffness of the wind-tunnel model. As with the point load data, the creep ratio is plotted for the same load cycle points as a function of time in Figure 6-8. Because the wing is heavily loaded for this test, the creep ratios are greater in magnitude. As with the point loads, apparent FEM errors are generally lower near the tip, except during the unload cycle. During unloading, the creep from the maximum loading continues to affect the measured displacements.

Table 6-2. Calculated and applied test loads

Point	x, in.	y, in.	Load, lb. CAP-TSD 0° AOA	Load, lb. Test 0° AOA	Load, lb. CAP-TSD 3° AOA	Load, lb. Test 3° AOA
10202	130.669	12.47	3.3	0	23.899	26.45
10204	151.362	12.47	3.567	-3.45	24.842	24.85
10205	165.987	12.47	-2.006	-2.1	23.405	25.1
10206	178.799	12.47	-5.405	-5.45	20.861	20.05
10208	190	12.47	-11.564	-11.6	13.421	13.5
10210	204.11	13.95	-23.642	-23.65	1.96	2.05
10402	151.362	21.03	2.127	-2.15	25.753	26.45
10403	165.987	21.03	-1.951	-2	25.215	26.8
10404	178.799	21.03	-5.838	-5.8	24.325	25.1
10406	190	21.03	-12.357	-12.35	16.65	16.6
10408	204.11	21.03	-24.236	-24.25	4.341	4.45
10502	165.987	27.08	-3.506	-3.5	25.177	25.5
10602	178.799	32.38	-7.013	-6.95	26.54	26.45
10604	190	32.38	-11.114	-12.15	19.477	22.05
10606	206.175	32.38	-19.045	-19.05	10.38	12.15
10803	187.072	40.02	-9.575	-9.65	20.032	20.05
10805	198.115	40.02	-13.775	-13.8	15.791	18.15
10807	209.158	40.02	-16.048	-16.05	13.104	13.05
11003	193.789	46.22	-7.878	-7.85	15.043	15.2
11005	202.688	46.22	-10.119	-10.05	12.319	12.4
11007	211.587	46.22	-11.161	-11.15	10.644	10.75
11203	200.506	52.42	-6.637	-6.6	11.672	11.65
11205	207.261	52.42	-7.587	-7.6	9.871	10.05
11207	214.015	52.42	-7.213	-7.2	7.131	7.35
11403	207.223	58.62	-5.036	-5.05	8.069	8.15
11405	211.834	58.62	-5.023	-5	6.26	6.35
11407	216.444	58.62	-3.605	-3.65	4.351	4.35
11503	210.43	61.58	-3.383	-3.4	5.237	5.4
11505	214.017	61.58	-2.993	-3.05	3.579	3.9
11507	217.603	61.58	-2.097	-2.15	2.743	2.9
Total load (lb.) =			-230.813	-246.7	432.092	447.25
Total load outboard of break =			-112.13	-112.25	145.846	149.7

Table 6-3. Distributed load cycle for three degrees AOA

Grid Point	Upload, Tab 8, lb.	Upload, Tab 16, lb.	Max Load, Tab 24, lb.	Unload, Tab 30, lb.	Unload, Tab 36, lb.
10202	26.45	26.45	26.45	26.45	26.45
10204	24.85	24.85	24.85	24.85	24.85
10205	25.1	25.1	25.1	25.1	25.1
10206	20.05	20.05	20.05	20.05	20.05
10208	13.5	13.5	13.5	13.5	13.5
10210	2.05	2.05	2.05	2.05	2.05
10402	26.45	26.45	26.45	26.45	26.45
10403	26.8	26.8	26.8	26.8	26.8
10404	25.1	25.1	25.1	25.1	25.1
10406	16.6	16.6	16.6	16.6	16.6
10408	4.45	4.45	4.45	4.45	4.45
10502	25.5	25.5	25.5	25.5	25.5
10602	26.45	26.45	26.45	26.45	26.45
10604	22.05	22.05	22.05	22.05	22.05
10606	12.15	12.15	12.15	12.15	12.15
10803			20.05	20.05	20.05
10805		18.15	18.15	18.15	18.15
10807	13.05	13.05	13.05	13.05	13.05
11003		15.2	15.2	15.2	
11005		12.4	12.4	12.4	
11007	10.75	10.75	10.75	10.75	
11203		11.65	11.65	11.65	
11205		10.05	10.05	10.05	
11207		7.35	7.35	7.35	
11403			8.15		
11405			6.35		
11407		4.35	4.35		
11503			5.4		
11505			3.9		
11507			2.9		
Total, lb.	321.35	400.5	447.25	416.2	348.8
Total outboard, lb.	23.8	102.95	149.7	118.65	51.25

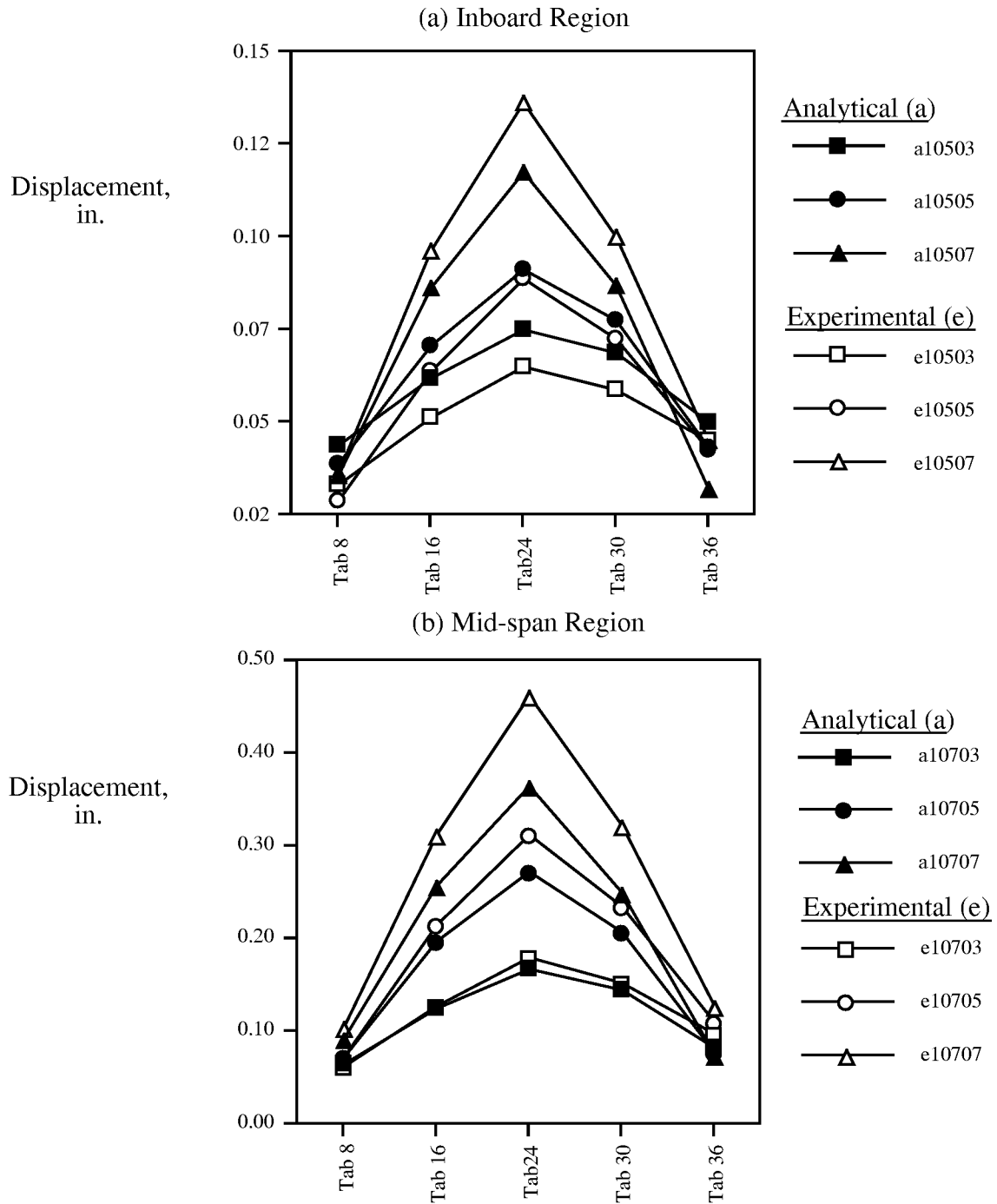


Figure 6-7. Displacements for 3° AOA distributed load.

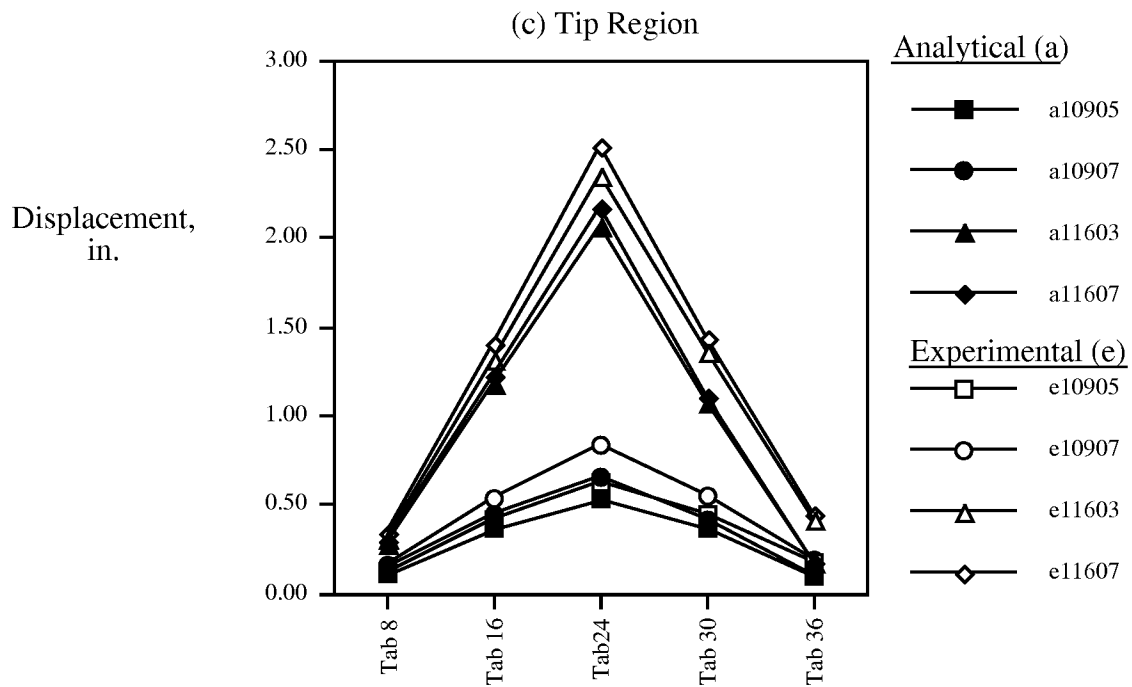


Figure 6-7(Continued). Displacements for 3° AOA distributed load.

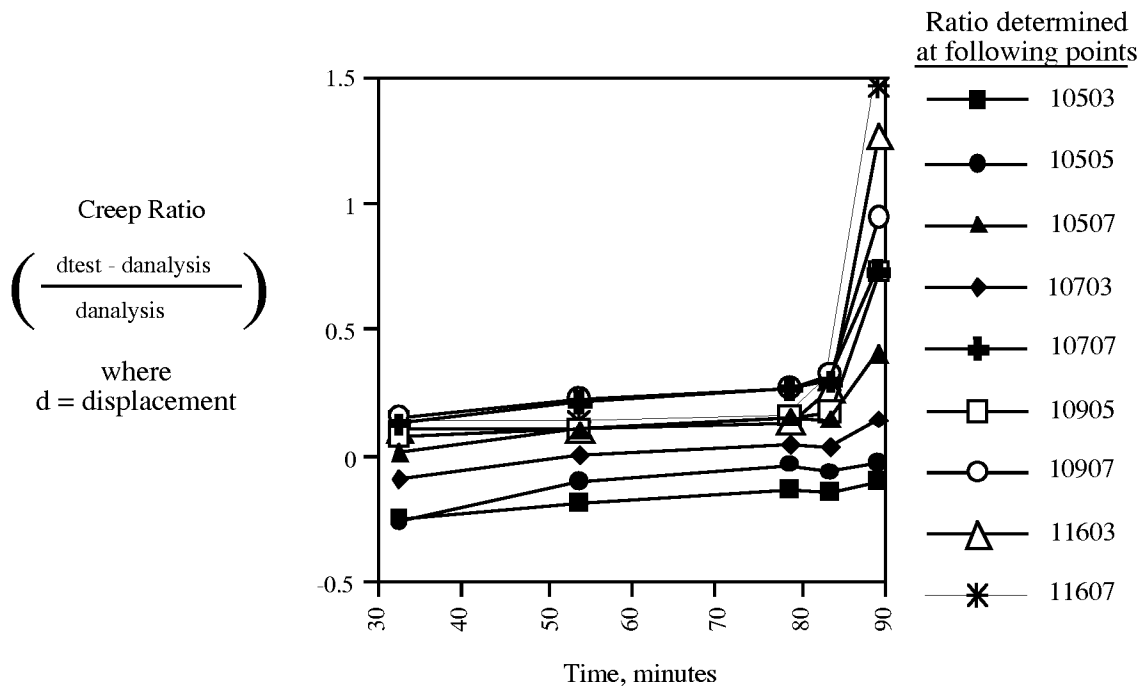


Figure 6-8. Creep for 3° AOA distributed load.

7.0 Flutter Analysis

Flutter analysis was a driving factor in the attempt to tune the FSM for flutter in the TDT, and consequently was performed repeatedly throughout the design and development stages of the wind-tunnel model. In the last days prior to the wind-tunnel test, the FEM and flutter analysis were continually updated based on experimental data from the GVT and loads test. Even during the wind-tunnel test itself, the process was repeated in order to account for configuration changes and TDT vibration test data.

A number of factors complicated the flutter analysis throughout the process. Following are some of those factors.

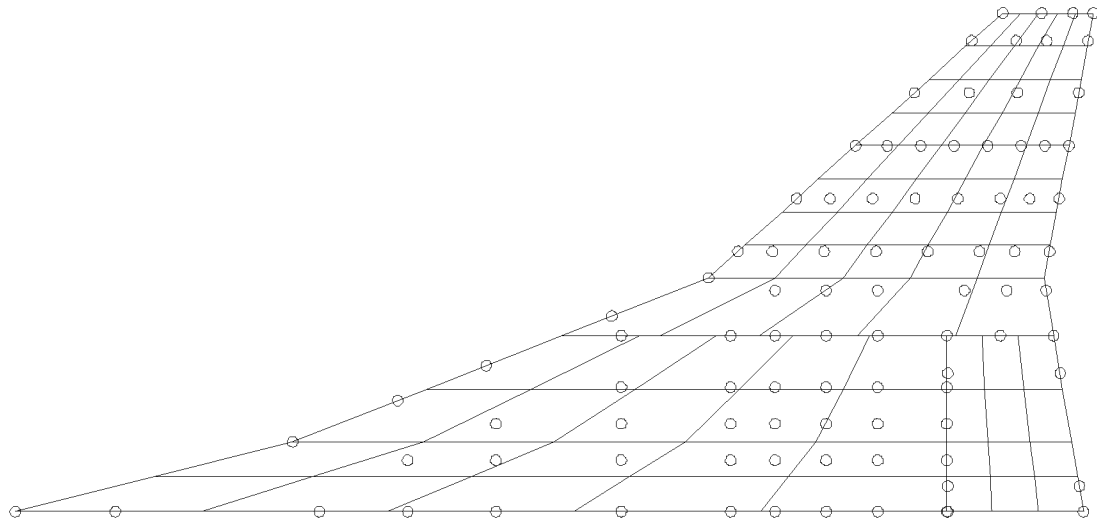
- a) The necessity to make the outboard wing proportionately thicker than the Reference H baseline wing. The increased thickness made it very difficult to obtain skins that were sufficiently flexible to allow the desired flutter behavior, yet strong enough to meet tunnel safety requirements.
- b) The tendency of the wing skins to creep, and the large scatter in the coupon stiffness data. As described in section 6.0 Static Loads Test, the “instantaneous” stiffness of the wing skins appeared substantially greater than the coupon data indicated.
- c) Lack of precise structural definitions of the mounting hardware, especially the dummy balance and the retractable turntable.
- d) The overall complexity of the wind-tunnel model arrangement. For example, the aerodynamics associated with the fuselage could be substantially different from a splitter plate which is often used for semi-span model flutter testing.
- e) The fact that the lowest dynamic pressure flutter mechanism predicted was a so-called hump mode which are typically difficult to predict with confidence.

7.1 Aeroelastic Models

Early in the design stage, a kernel function flutter analysis model was developed and used for design synthesis. Subsequently, an ISAC (ISAC is described in unpublished preliminary NASA TM 100662 by Hoadley and Adams, June 1992) model was also developed as a backup procedure. Generally, the two models produced similar results, with the kernel function usually predicting slightly higher flutter dynamic pressures. During and after the actual wind-tunnel test, the ISAC model was used exclusively. This latter shift to the ISAC model was made only after it was shown that the results were consistently similar, and was largely a matter of convenience and the expertise of the personnel available to perform the analyses.

The aeroelastic models, when used with the FEM and specially developed FORTRAN routines, provide a complete subsonic aeroelastic analysis package for the FSM. These files are available on request from authorized HSR participants.

Figure 7-1 shows the box layout for the ISAC Doublet Lattice unsteady aerodynamics model. The circles indicate the positions of the structural points used to define mode shapes for the ISAC routines. This model was used along with the p-k method of the STABCAR Code⁴ for the post-test results discussed below.



HSCT FLEXIBLE SEMISPAN



ISAC

/DLIN

DATE: FEB 20,97

TIME: 16:33:59

Figure 7-1. ISAC Doublet Lattice model with superimposed FEM grid points.

7.2 Pretest Analysis

Figure 7-2 gives predicted flutter boundary plots based on the finite element model version 18-2 (see Table 3-1) which was run with and without a 2.2 lb. tip mass. The kernel function results show a dramatic decrease in flutter q due to the tip mass. The ISAC results agree well with the kernel function prediction for the 14 Hz mechanism, but also predict a weak hump mode at 32 Hz. The kernel function results also indicate the presence of such a hump mode which remains slightly stable. In order to achieve flutter near a dynamic pressure of 200 psf, these predictions resulted in a decision to install 2.5 lb. of tungsten in the wind-tunnel model trailing edge near the wing tip.

HSR-FSM Analytical Flutter Boundary Kernel Function Aerodynamics

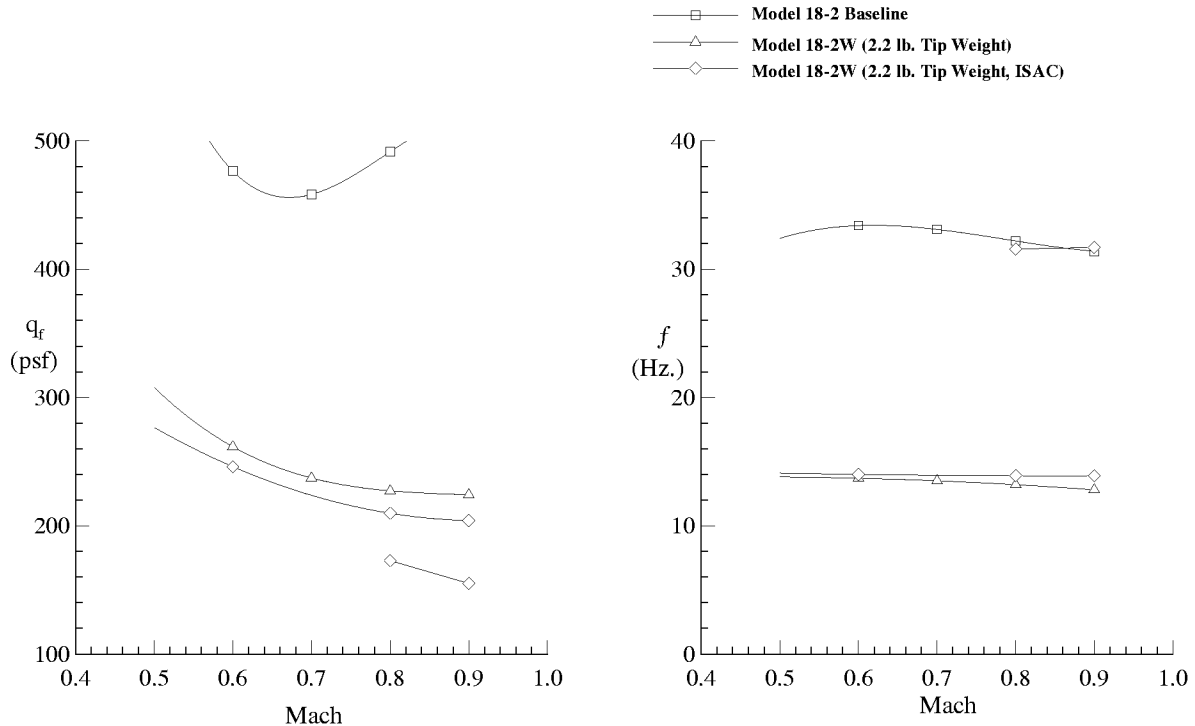


Figure 7-2. Pretest flutter analyses.

7.3 Post-test Analysis

Figure 7-3 gives dynamic pressure and frequency flutter boundary plots for the wind-tunnel configuration based on FEM version 18-5 and the ISAC aeroelastic model. The plot also indicates the observed flutter points in the TDT. The highest Mach number point is where the model was lost due to hard flutter. Except for a period when the wing trailing edge had become loose, the model was more resistant to flutter than had been predicted. The only observed flutter occurred in what appeared to be “deeply transonic” conditions. The model had repeatedly experienced high dynamic response in the 12 to 14 Hertz range near Mach 0.98 at substantially lower dynamic pressure. Because the model was lost before subsonic flutter could be observed, there can be no direct comparison between analytical and experimental flutter at a Mach number (Mach 0.8 or less) where confidence in a linear analysis such as ISAC would be greater.

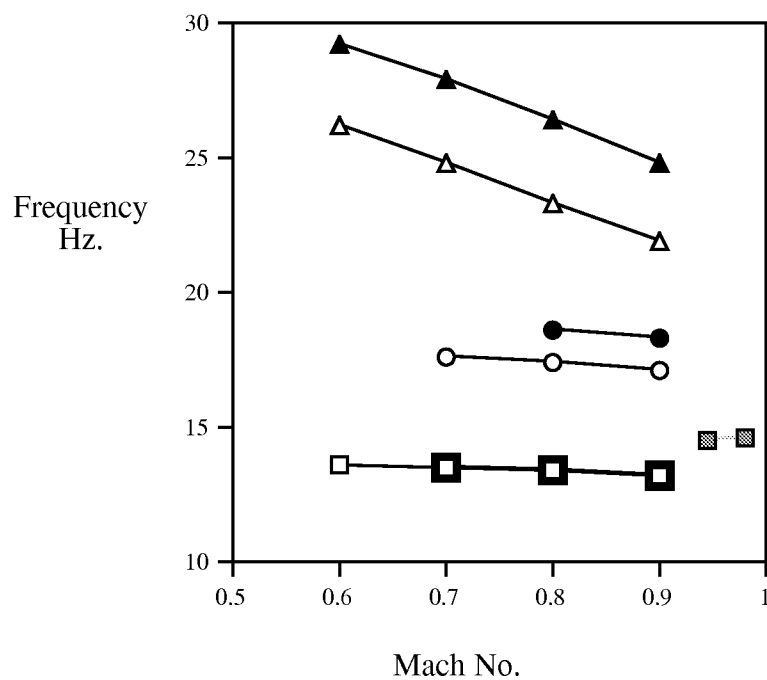
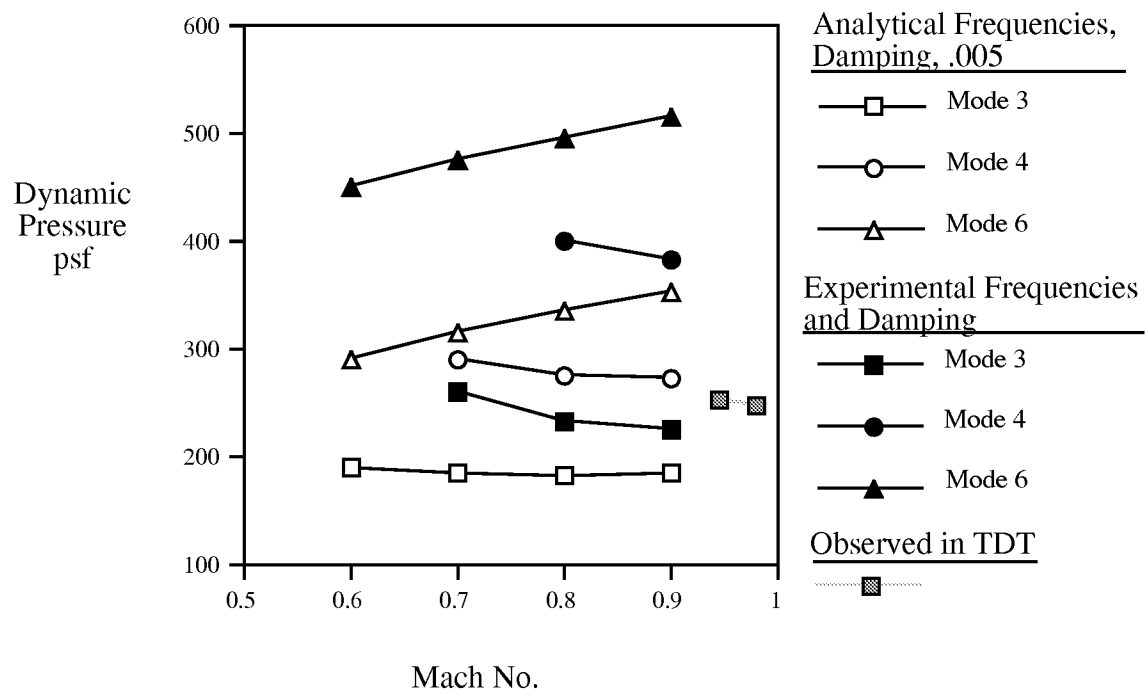


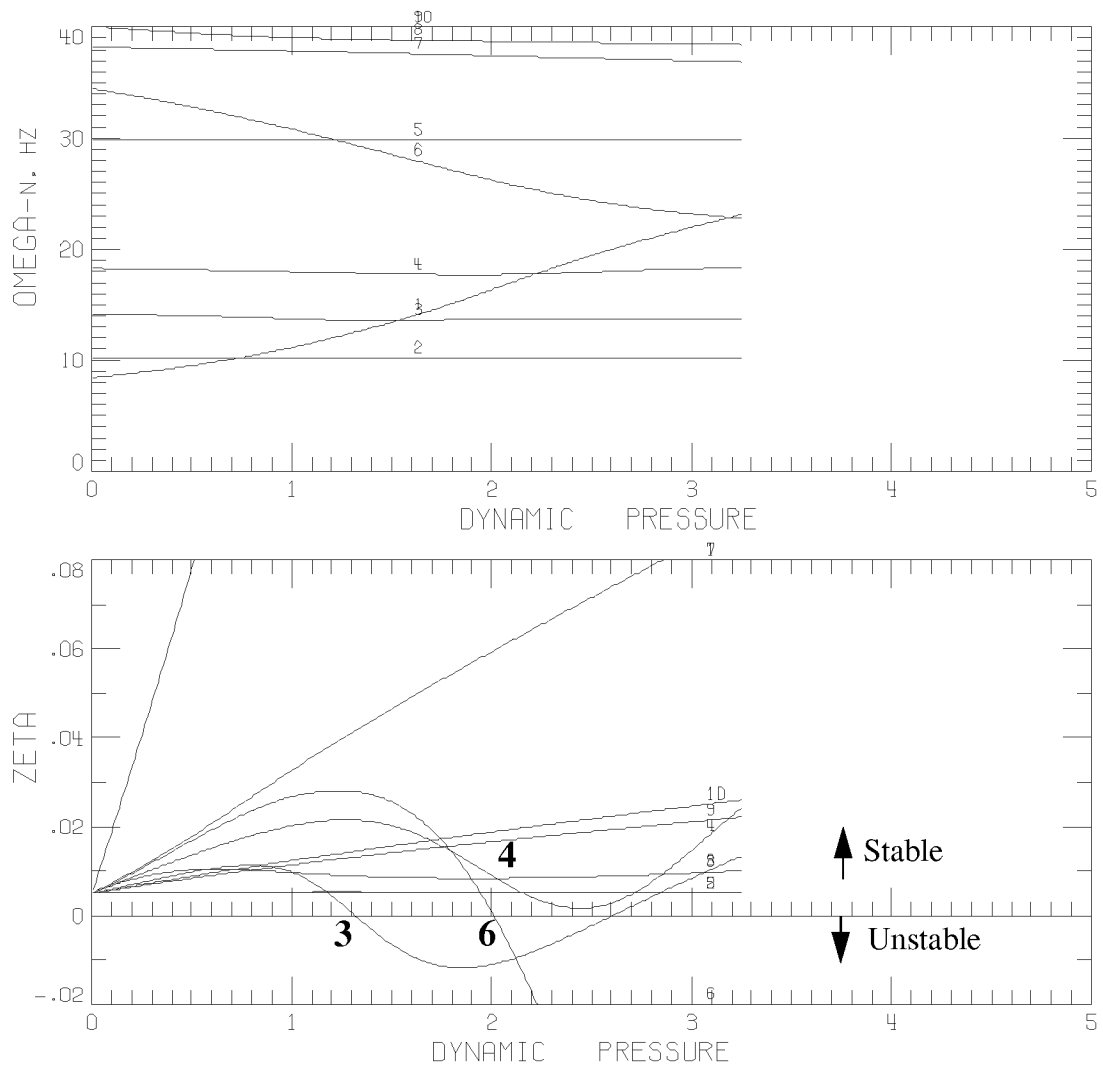
Figure 7-3. Post-test flutter analyses for the wind-tunnel flutter configuration.

Based on the analytical frequencies and nominal damping values of 0.5% critical damping, a 14 Hz flutter mechanism was predicted at just under 200 psf (open symbols on Figure 7-3). STABCAR stability and frequency plots showing these results are given in Figure 7-4 for Mach numbers 0.6, 0.7, 0.8, and 0.9 respectively. The critical (lowest dynamic pressure) mechanism involves mode 3 and is a hump mode which appears to involve considerable wing bending along with pitch and plunge from the mounting system (based on the mode shapes shown in Figure 4-5). The hump mode appears stronger (i.e. sharper crossing, deeper negative damping trace) as the Mach number increases.

Because the critical flutter mechanism is a hump mode, it is more difficult to predict than a flutter mechanism with a sharp crossing (such as mode 6). However, when the appropriate experimental modal frequencies and dampings (see Table 4-3) are substituted for analytical values, the resulting flutter analysis provides some useful insight. The filled symbols in Figure 7-3 are the results of these analyses and correspond to the stability plots of Figure 7-5. When using experimental frequencies and damping, it appears that the 14 Hz flutter mechanism is higher in dynamic pressure and weaker (shallower crossings) than for the pure analytical values used for Figure 7-3. In fact, the 14 Hz flutter mechanism disappears completely below Mach 0.7. Although this does not completely resolve differences between analysis and experiment, it indicates that the intended mechanism could have in reality been much weaker in the subsonic range, and higher in dynamic pressure, than pretest analysis indicated.

7.4 Flutter Analysis Summary

The FSM was shown to be flutter free at subsonic dynamic pressures greater than the pressures at which flutter was predicted by analysis. Unfortunately the wing encountered catastrophic flutter at a dynamic pressure of about 246 psf, Mach 0.98. There were a number of probable factors leading to the wing being more resistant to flutter than desired or predicted. These include the overall configuration complexity and a lack of better definition of the supporting structures (such as the dummy balance and retractable turntable). However, the authors feel that the most significant factors involve problems with the wing skins. When the wing was actually sized, approximately a year before the wind-tunnel test, it became apparent that it would be very difficult to find a material with sufficient flexibility and strength for the outer wing panel. Data from the manufacturer indicated this was possible with Fiberglass 108. The time schedule required that the fabrication process commence, so the skin material selection became irreversible. During the summer of 1995, an error in FEM geometry was discovered, and when corrected, the finite element model became stiffer than desired. However, with the use of tip weights, it appeared that a reasonable flutter mechanism could still be achieved. As fabrication proceeded, coupon testing indicated that the skins were somewhat stiffer than anticipated from the manufacturer's estimates, and inconsistent in modulus among the various samples. Even the coupon data however, indicated that the skin was more flexible than the subsequent vibration testing indicated. The authors finally concluded, based on further vibration and static loads testing, that apparent skin moduli depend on the testing method. The nonlinearity of the material due to creep gives an apparent stiffness somewhat lower than the "instantaneous" stiffness desired for flutter analysis models. Even today, it is not known if there is a suitable material available that would have met the design requirements. Such a material would have to be extremely flexible, yet strong and linear with respect to load magnitude and time under load. This experience should be considered for future HSR stressed-skin flutter model designs.



INPUT VELOCITY IS 3.600E+03±±
 HSR FLEXIBLE SEMISPAN, M 0.6. FREQN



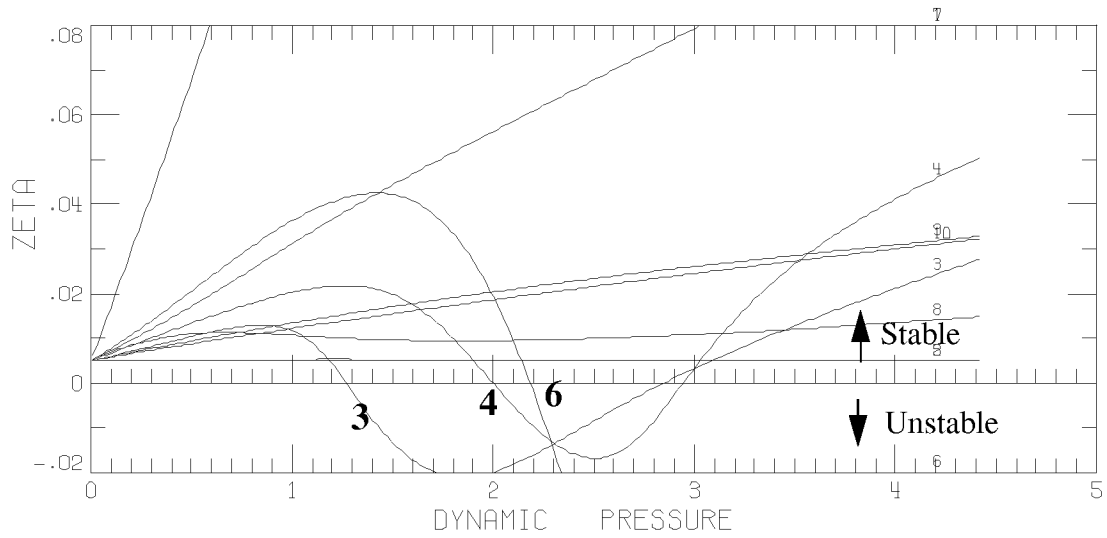
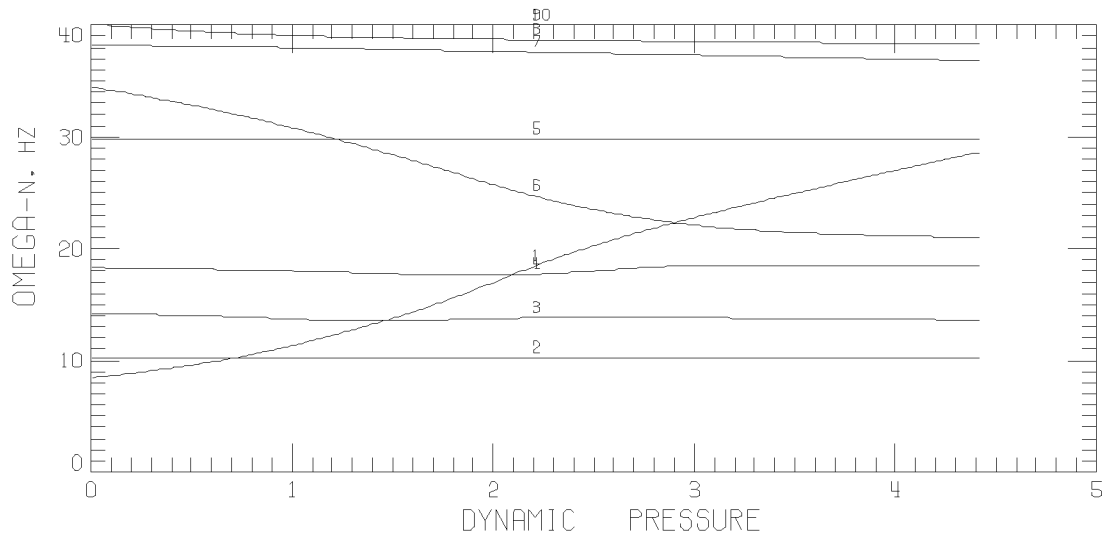
I S A C

/STABCAR

DATE: FEB 21, 97

TIME: 10:56:49

Figure 7-4. STABCAR modal frequency and stability plots based on analytical frequencies and nominal damping.

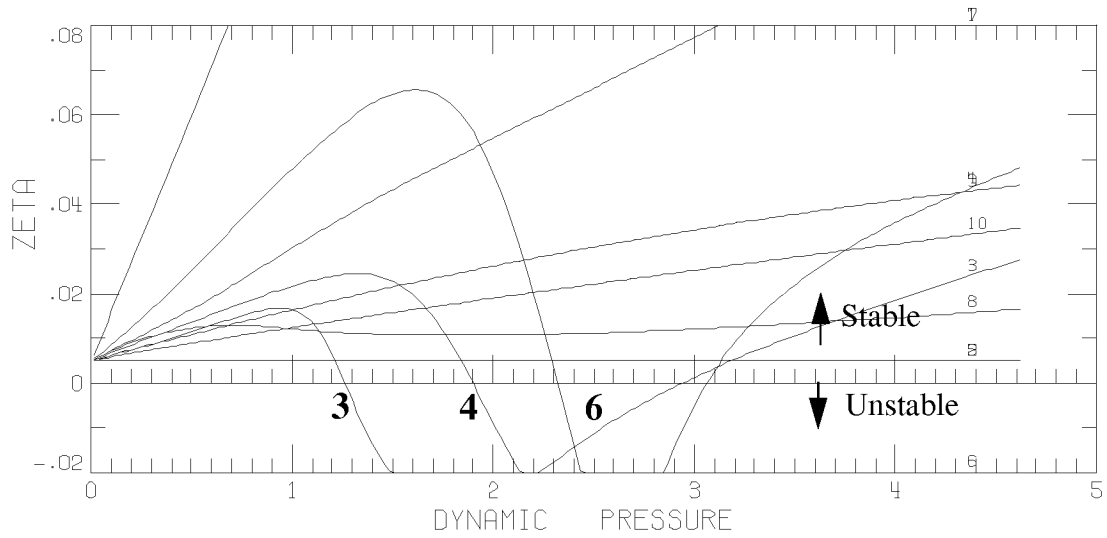
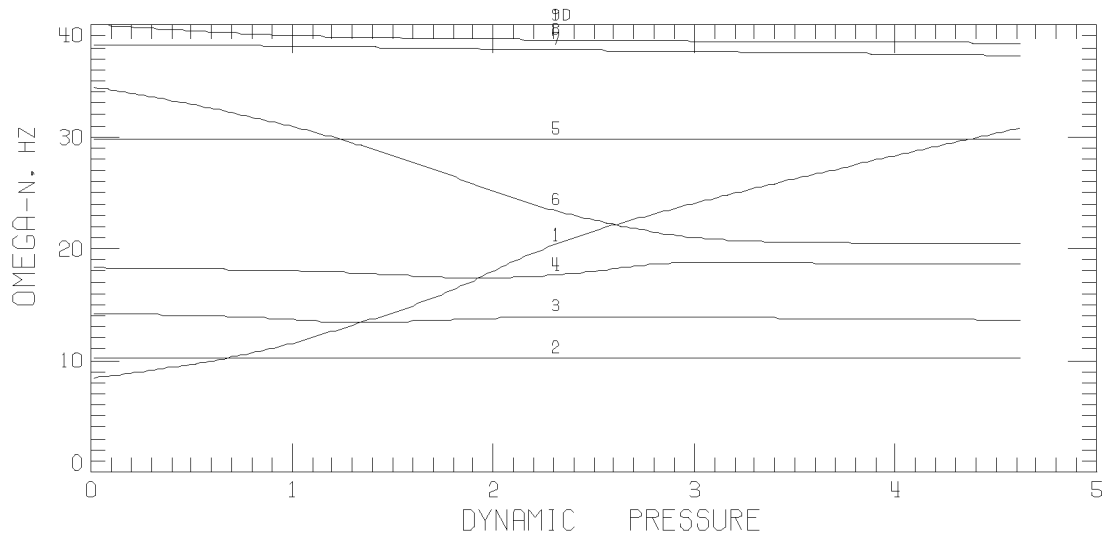


INPUT VELOCITY IS 4.200E+03±±
HSR FLEXIBLE SEMISPAN, M 0.7. FREDN



I S A C /STABCAR DATE: FEB 21,97 TIME: 12:34:09

Figure 7-4(Continued). STABCAR modal frequency and stability plots based on analytical frequencies and nominal damping.



INPUT VELOCITY IS 4.800E+03±±
 HSR FLEXIBLE SEMISPAN, M 0.8. FREDN



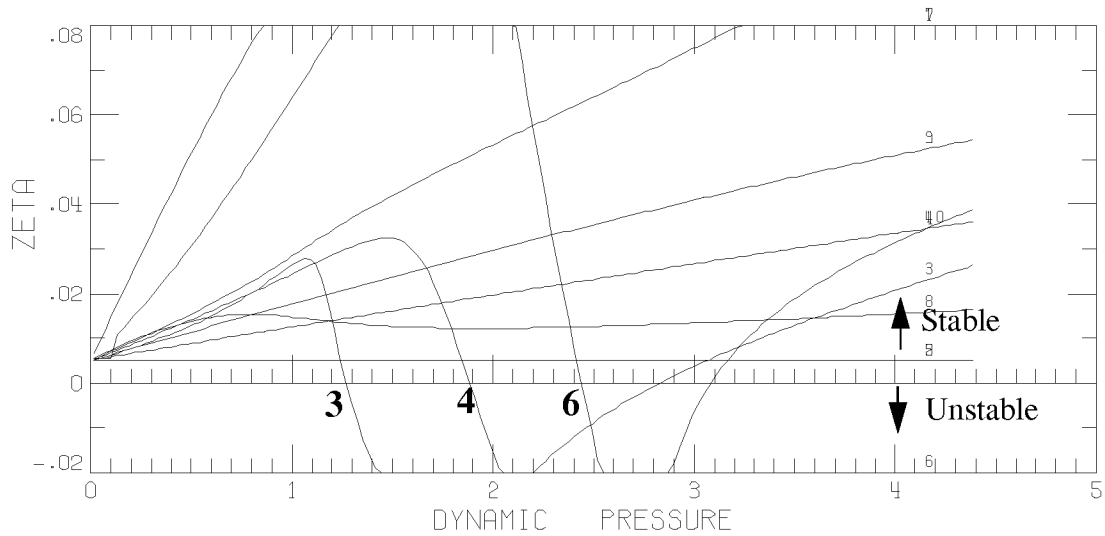
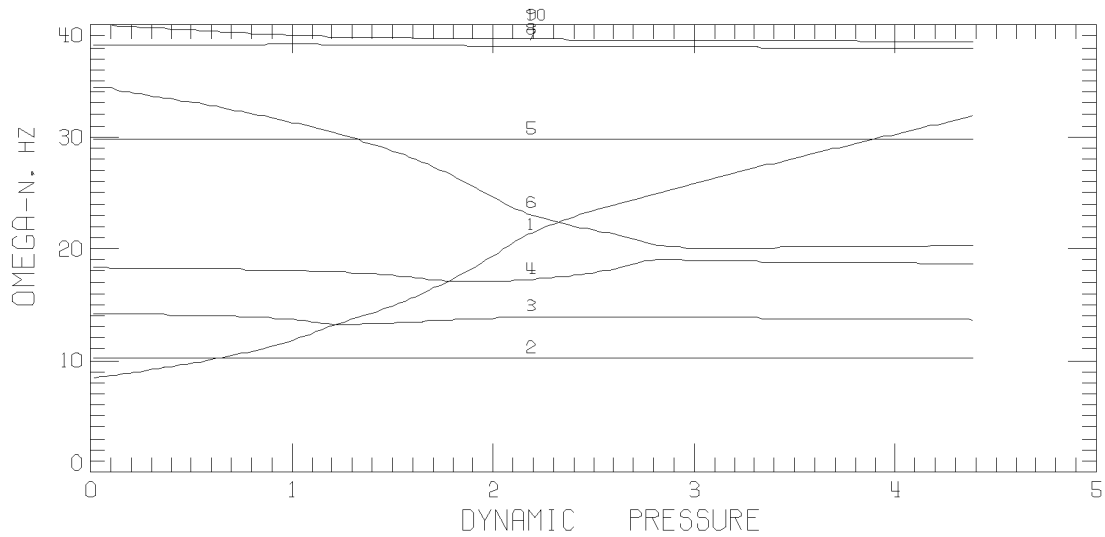
I S A C

/STABCAR

DATE: FEB 21,97

TIME: 12:40:09

Figure 7-4(Continued). STABCAR modal frequency and stability plots based on analytical frequencies and nominal damping.

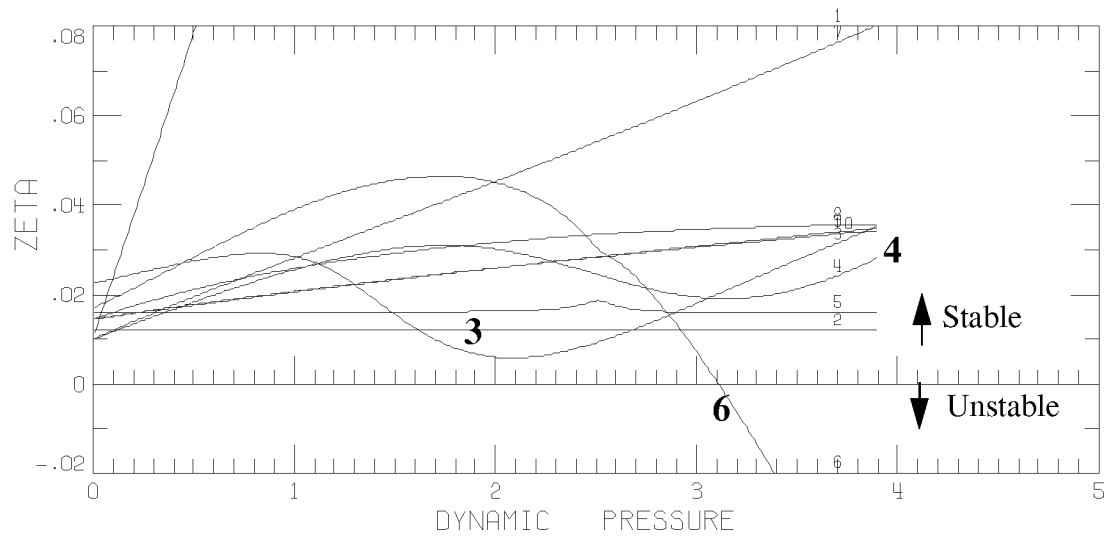
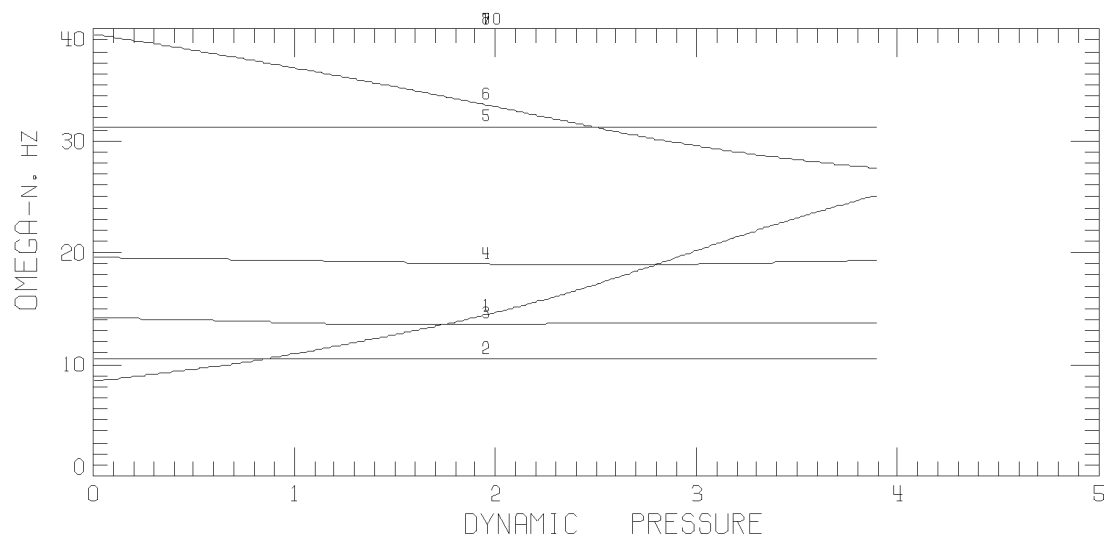


INPUT VELOCITY IS 5.400E+03±±
 HSR FLEXIBLE SEMISPAN, M 0.9, FREON



I S A C /STABCAR DATE: FEB 21,97 TIME: 12:50:59

Figure 7-4(Continued). STABCAR modal frequency and stability plots based on analytical frequencies and nominal damping.



INPUT VELOCITY IS 3.600E+03±±
HSR FLEXIBLE SEMISPAN, M 0.6, FREQN



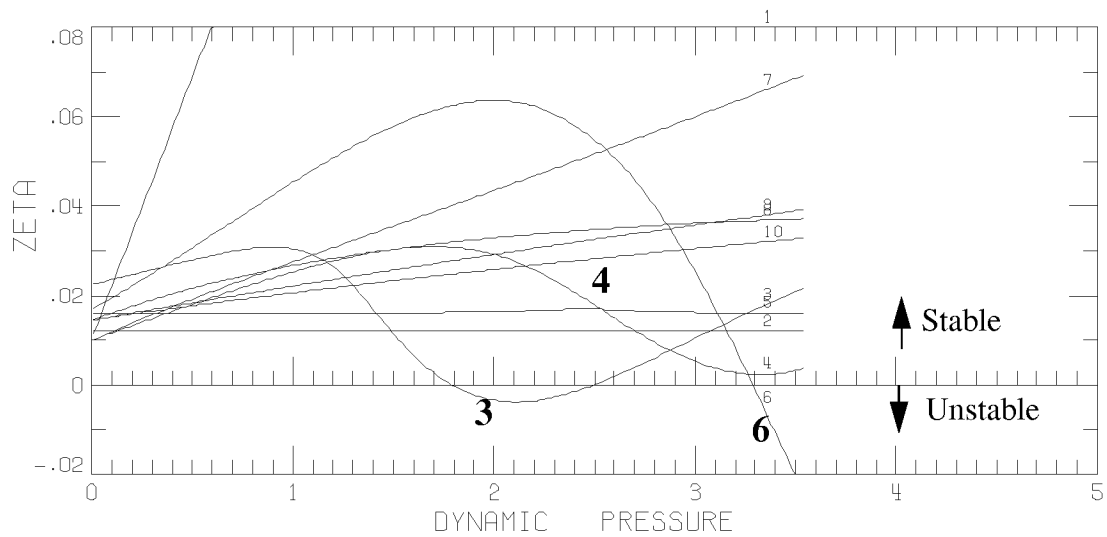
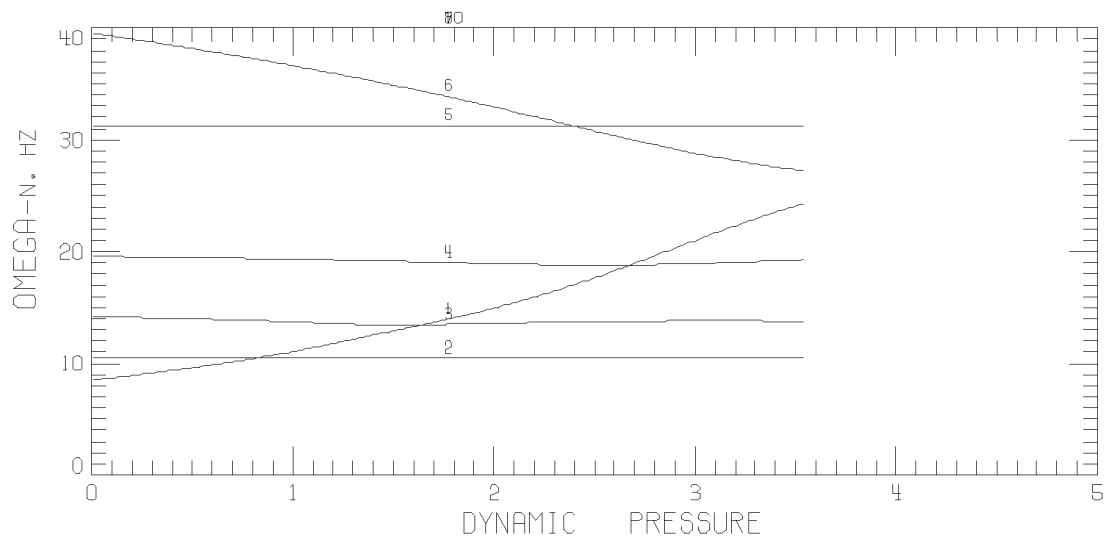
I S A C

/STABCAR

DATE: FEB 21,97

TIME: 08:26:49

Figure 7-5. STABCAR modal frequency and stability plots based on experimental frequencies and damping.



INPUT VELOCITY IS 4.200E+03±±
HSR FLEXIBLE SEMISPAN, M 0.7. FREQN



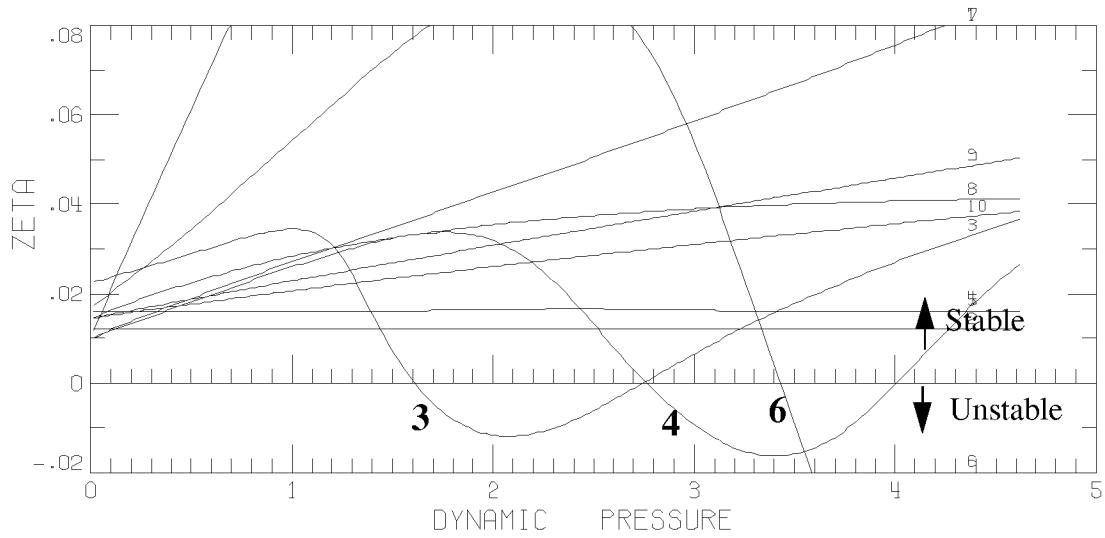
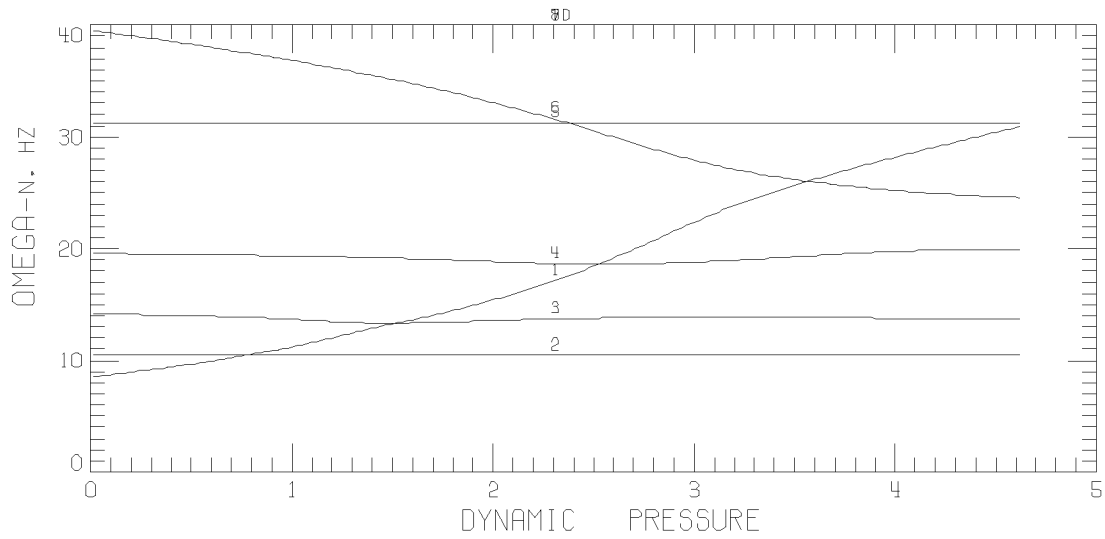
I S A C

/STABCAR

DATE: FEB 22, 97

TIME: 14:00:49

Figure 7-5 (Continued). STABCAR modal frequency and stability plots based on experimental frequencies and damping.



INPUT VELOCITY IS 4.800E+03±±
 HSR FLEXIBLE SEMISPAN, M 0.8, FREON



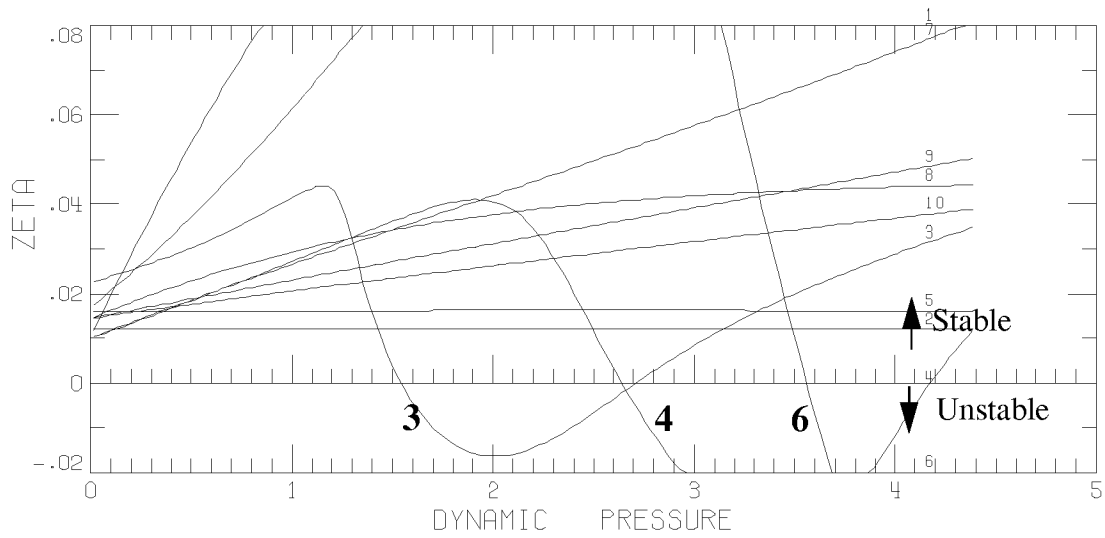
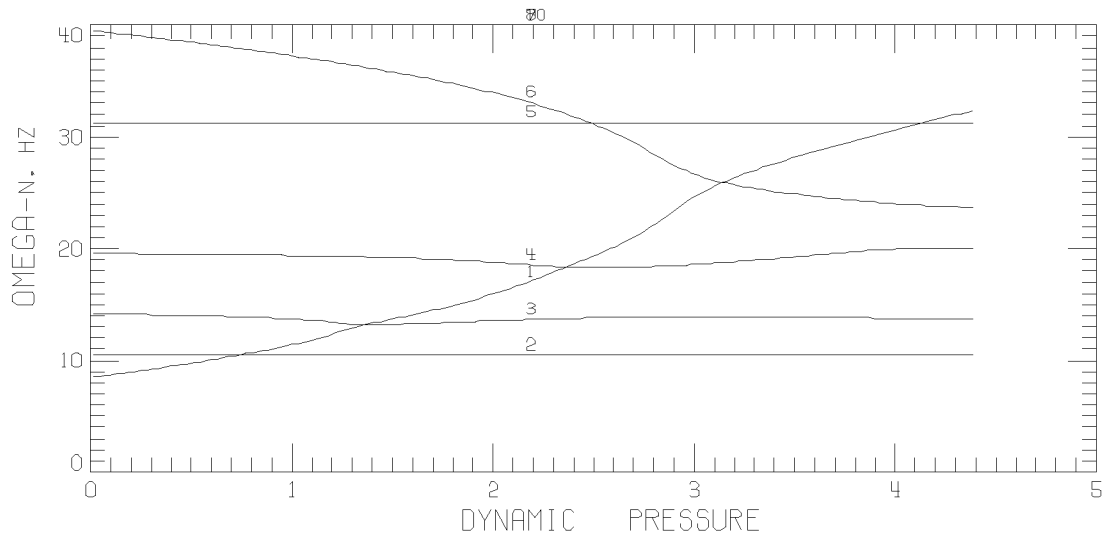
I S A C

/STABCAR

DATE: FEB 18, 97

TIME: 11:23:39

Figure 7-5 (Continued). STABCAR modal frequency and stability plots based on experimental frequencies and damping.



INPUT VELOCITY IS 5.400E+03±±
HSR FLEXIBLE SEMISPAN, M 0.9, FREON



I S A C /STABCAR DATE: FEB 21,97 TIME: 10:29:49

Figure 7-5 (Continued). STABCAR modal frequency and stability plots based on experimental frequencies and damping.

8.0 Wind Tunnel Testing on Loads Balance

This section describes the aerodynamic data acquired on the HSR-FSM during NASA Langley Transonic Dynamics Tunnel (TDT) Test 521 conducted from 8 April to 6 May, 1996. Angle-of-attack and control surface deflection polars at subsonic, transonic and low-supersonic Mach numbers were obtained in the tunnel's heavy gas configuration. Unsteady pressure and steady loads data were acquired on the wing, while steady pressures were measured on the fuselage.

These data were reduced using a variety of methods, programs and computer systems. The reduced data was ultimately compiled onto a CD-ROM volume which was distributed to HSR industry team members in August, 1996. The methods used to acquire and reduce the data are documented in this section, and the quality, repeatability, and overall character of the measured aerodynamics are assessed.

8.1 Test Conditions and Data Summary

The HSR-FSM was tested over a wide range of flight conditions. A series of angle-of-attack and flap deflection polars were acquired for Mach numbers ranging from 0.8 to 1.15. The model angle-of-attack was limited by the aerodynamic load the wing could safely withstand and typically varied between -1 and 3 degrees. Flap deflections were limited to +/- 4 degrees. Freestream dynamic pressure was also varied to assess its impact on the quality of the aerodynamic data obtained and to determine if any aeroelastic effects could be observed during the testing of the model. Data at dynamic pressures of 100, 125, and 150 lbs./ft.² (psf) were acquired during this test.

A summary of the angle-of-attack and flap deflection polars is presented in Table 8-1. In this table, the data are organized by configuration, dynamic pressure and Mach number. The run number, range of tab points and comments are provided for each variation. The major configurations tested were clean-wing and wing-with-nacelles.

8.2 Loads Data Acquisition and Reduction

Five component aerodynamic loads data were acquired for each point at which pressure data were obtained. Side force is the only load component not measured in this test. The balance limits and assumed resolution for this test are shown in Table 8-2. In this table, the measurement resolution was obtained using the measured balance error. This absolute load increment was then converted to coefficient form to provide a guideline for balance resolution in terms of standard aerodynamic quantities. These resolutions are considered conservative since measurements in the TDT verified that the balance was able to resolve normal, pitch and roll loads that are smaller than the quoted balance errors.

Table 8-1. HSR-FSM polar summary
TDT T521 Aerodynamic Data Run Log

No Nacelles, AOA Polars

Mach No.	Dynamic Pressure (PSF)	Run No.	Tab Nos.	Comments
0.80	100	11	321 - 333	Tab 332 Missing, Unrecoverable Data
0.95	100	8	232 - 242	
0.98	100	7	207 - 217	
1.02	100	7	194 - 205	
1.05	100	7	181 - 192	
1.10	100	7	169 - 180	
0.90	125	12	371 - 379	Tab 266 Missing
1.02	123	9	264 - 273	
1.02	123	11	310 - 319	
1.05	125	8	248 - 256	
1.15	123	8	221 - 231	
0.80	150	13	471 - 479	
0.85	150	13	458 - 465	
0.90	150	13	450 - 457	
0.95	150	13	438 - 444	
0.97	150	12	420 - 426	
0.98	150	12	408 - 414	
0.99	150	12	402 - 407	
1.00	150	12	396 - 401	
1.02	150	12	384 - 390	
1.05	150	11	357 - 363	
1.10	150	11	343 - 351	
1.15	150	9	275 - 283	

Nacelles On, AOA Polars

Mach No.	Dynamic Pressure (PSF)	Run No.	Tab Nos.	Comments
0.80	100	15	567 - 577	
0.95	97	15	557 - 566	
0.98	100	15	547 - 556	
1.05	97	15	535 - 544	
1.10	100	15	524 - 534	
0.80	150	18	659 - 666	
0.95	150	16	611 - 617	
0.98	150	16	604 - 610	
1.05	149	16	592 - 598	
1.10	155	16	585 - 591	
1.10	150	18	642 - 648	

Table 8-1. HSR-FSM polar summary
TDT T521 Aerodynamic Data Run Log

No Nacelles, Flap Polars

Mach No.	Dynamic Pressure (PSF)	Run No.	Tab Nos.	Comments
0.80	100	11	333 - 337	
0.95	100	8	242 - 246	
0.90	126	12	379 - 383	
1.05	125	8	256 - 260	
0.80	150	13	479 - 486	Tab 419 Bad Force Data
0.85	150	13	465 - 470	
0.95	150	13	444 - 449	
0.98	149	12	414 - 419	
1.02	148	12	390 - 395	
1.10	155	11	351 - 356	
0.80	101	11	338 - 342	Flap Oscillation
0.80	152	13	487 - 488	Flap Oscillation

Nacelles-on, Flap Polars

Mach No.	Dynamic Pressure (PSF)	Run No.	Tab Nos.	Comments
0.80	150	18	666 - 670	
0.95	150	18	650 - 654	
1.05	149	16	598 - 602	

Table 8-2. Balance load limits and assumed measurement resolution.

Component	Load Limit	Resolution ($\alpha = 0^\circ$, $q = 100\text{psf}$)
Normal Force	1500 lb.	$\Delta C_L = \pm 0.00365$
Axial Force	120 lb.	$\Delta C_D = \pm 0.000284$
Pitching Moment	6000 in.-lb.	$\Delta C_M = \pm 0.000754$
Rolling Moment	30,000 in.-lb.	$\Delta C_l = \pm 0.000626$
Yaw Moment	3000 in.-lb.	$\Delta C_n = \pm 0.000375$

The aerodynamic loads data presented in this report were reduced based on the diagram and reference areas and lengths presented in Figure 8-1. Since the planform for this model is a 1/12 scale version of the Boeing Reference H concept, the reference areas and lengths used to assess the aerodynamics of Reference H, appropriately scaled, were used for the present data reduction. The balance is located very near 50% mean aerodynamic chord, so this location was used as the streamwise moment center. The spanwise moment center is the TDT east wall, and the vertical moment center was chosen as the vertical location of the wing root leading edge. The equations used to compute the aerodynamic moments are also presented in the figure. Note that a side force

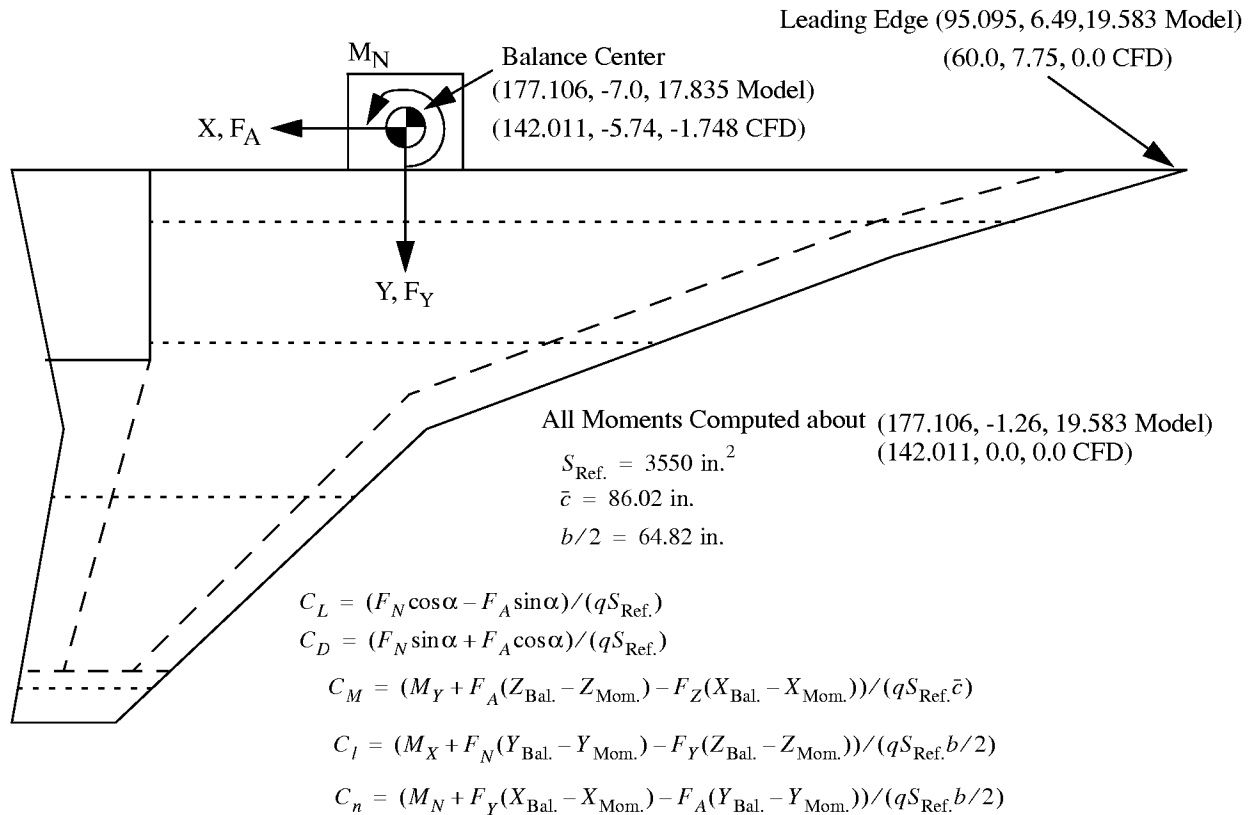


Figure 8-1. Reference diagram for calculation of HSR-RSM aerodynamic loads.

coefficient is not included in the list since the balance did not measure this force component. Also, the actual equations for the moment coefficients are considerably simpler than what is shown since the side force component is zero and the streamwise location of the balance and the moment center are the same.

Aerodynamic polars with respect to angle-of-attack and flap deflection were processed post-test using the TDT channel statistics files generated for each tab point at which pressure data were acquired. The post processing program reads a specified set of channel statistic files, sorts them by increasing angle-of-attack or flap deflection, converts the balance data into aerodynamic coefficients based on a specified set of reference data and prints out the data in tabular form. A

sample output from the force polar post processing program is shown in Figure 8-2. In addition to tabulating the acquired data, the post processor also curve fits the lift drag and pitching moment data using a least squares approximation. The equations used to fit the data are:

$$\begin{aligned} C_L &= C_{L_0} + C_{L_\alpha} \alpha \\ C_M &= C_{M_{C_L=0}} + C_{M_{C_L}} C_L \\ C_D &= C_{D_{min}} + k \left(C_L - C_{L_{C_{D_{min}}}} \right)^2 \end{aligned} \tag{8-1}$$

The lift coefficient data are fit as a function of angle-of-attack or flap deflection depending on the type of polar, and a linear approximation is used for this purpose. The coefficients C_{L_0} and C_{L_α} are the computed lift at zero AOA or flap deflection and the lift curve slope, respectively. The pitching moment is fit as a function of lift coefficient and again a linear approximation is utilized. In this equation, $C_{M_{C_L=0}}$ and $C_{M_{C_L}}$ are the pitching moment at zero lift and the pitching moment slope as a function of lift coefficient, respectively. The drag coefficient fit is computed as a quadratic function of lift coefficient. The coefficient $C_{D_{min}}$ is the computed minimum drag, k is the so-called drag due to C_L^2 , and $C_{L_{C_{D_{min}}}}$ is the lift coefficient at minimum drag. Each of these coefficients is computed from the least squares fit and printed with the tabular data along with the Root Mean Squared (RMS) error for each fit.

Lift, drag, and pitching moment data from the post processing code are also written to a separate file for plotting. A sample force data plot is presented in Figure 8-3. In this figure, the experimental data points are represented by the symbols, while the curve fit data are shown by the solid line.

```

TDT T521 HSR-FSM (Balance), Run    8
M=0.95 R-12 Q=100 R08 T232-242
*****

Mach 0.9506    Q  99.9 psf    Re  1.548 million/ft.

***** Fit Data *****
CL0=-0.0518 dCL/dalpha= 0.0466          CL = CL0 + dCL/dalpha*alpha
CM0= 0.0081 dCM/dCL=-0.0779           CM = CM0 + dCM/dCL*CL
CD0= 0.0065 K= 0.1989 CLCD0= 0.0125     CD = CD0 + K*(CL-CLCD0)**2

***** Fit RMS Error *****
CLrms=0.00059  CMrms=0.00008  CDrms=0.00006

Alpha    Delf    CL      CD      CM      Cl      Cn      Tab
-----
-0.50    0.02   -0.0742  0.0079  0.0140  -0.0400  0.0013  234
 0.00    0.02   -0.0529  0.0074  0.0123  -0.0282  0.0015  233
 0.52    0.02   -0.0273  0.0067  0.0100  -0.0153  0.0017  235
 0.99    0.01   -0.0065  0.0065  0.0086  -0.0045  0.0016  242
 1.00    0.02   -0.0053  0.0065  0.0084  -0.0037  0.0016  232
 1.02    0.02   -0.0042  0.0066  0.0084  -0.0037  0.0018  236
 1.50    0.02    0.0188  0.0065  0.0067  0.0077  0.0016  237
 1.99    0.01    0.0410  0.0066  0.0050  0.0191  0.0015  241
 2.01    0.01    0.0416  0.0066  0.0048  0.0193  0.0014  238
 2.52    0.01    0.0654  0.0071  0.0030  0.0314  0.0013  239
 3.00    0.00    0.0889  0.0076  0.0012  0.0434  0.0010  240

```

Figure 8-2. Sample tabular output from force data post processing program.

TDT T521 HSR-FSM (Balance)

- M=0.95 R-12 Q=100 R08 T232-242
- △— M=1.05 R-12 Q=125 R08 T248-256
- M=1.15 R-12 Q=125 R08 T221-231

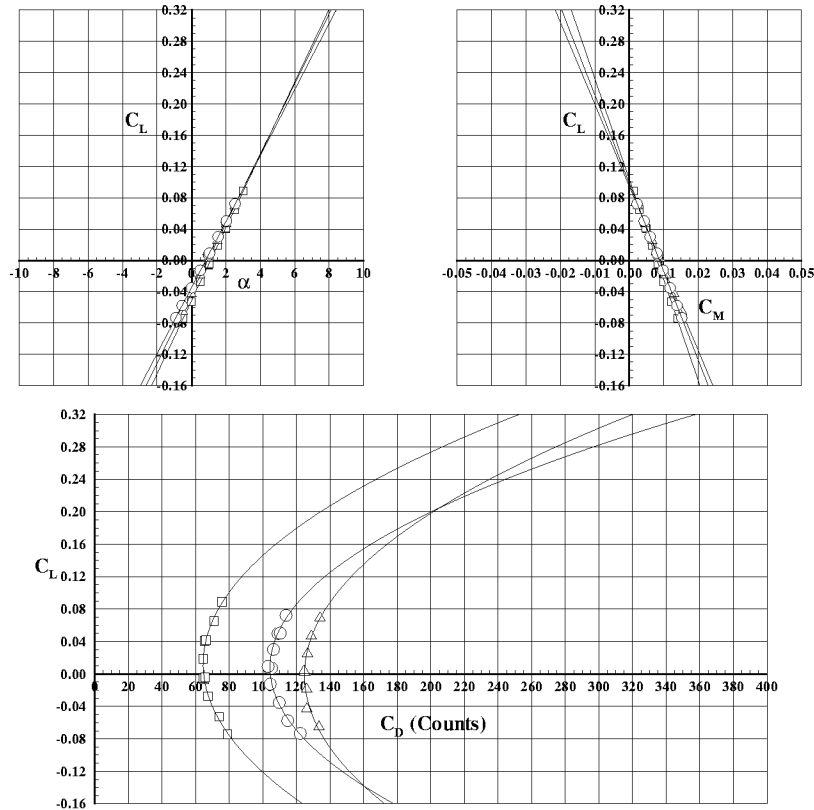


Figure 8-3. Sample plot from force data post processing program.

8.3 Loads Data Analysis

The tabulated loads data were written to CD-ROM and delivered to the airframe companies along with hardcopies of the force data plots for each TDT run. Therefore, a complete listing of the tabular data and plots will not be repeated in this report. However, we will assess the character and quality of the force data by reviewing selected polars that illustrate the primary objectives of the test. We will examine the variation of the data with Mach number and dynamic pressure, the effect of the nacelles, and the performance of the control surface as a function of Mach number.

8.3.1 Effect of Variation of Dynamic Pressure

Dynamic pressures of 100, 125, and 150 psf were run during this test to assess the aeroelastic qualities of the model. Figure 8-4 presents the aerodynamic data for the clean wing configuration

at Mach 0.8 and dynamic pressures of 100 and 150 psf. The range of dynamic pressures tested do not have a significant impact on the aerodynamic performance of this model at these conditions. Examination of the curve fit data indicates that the lift curve slope at 150 psf is slightly lower than at 100 psf, which is expected for a flexible swept-back wing. Likewise the pitching moment slope is slightly more positive for the 150 psf case, which is indicative of the wing washing out near the tip as the aerodynamic load is increased. The largest impact of the variation of the dynamic pressure is seen in the drag comparison with the drag at 150 psf being lower than at 100 psf. However, this comparison may be misleading at the higher lift coefficients since the 150 psf polar is based on fewer data points than the 100 psf data. The larger aerodynamic loads at 150 psf prevented us from testing the wing at higher lift coefficients due to model safety considerations.

TDT T521 HSR-FSM (Balance)

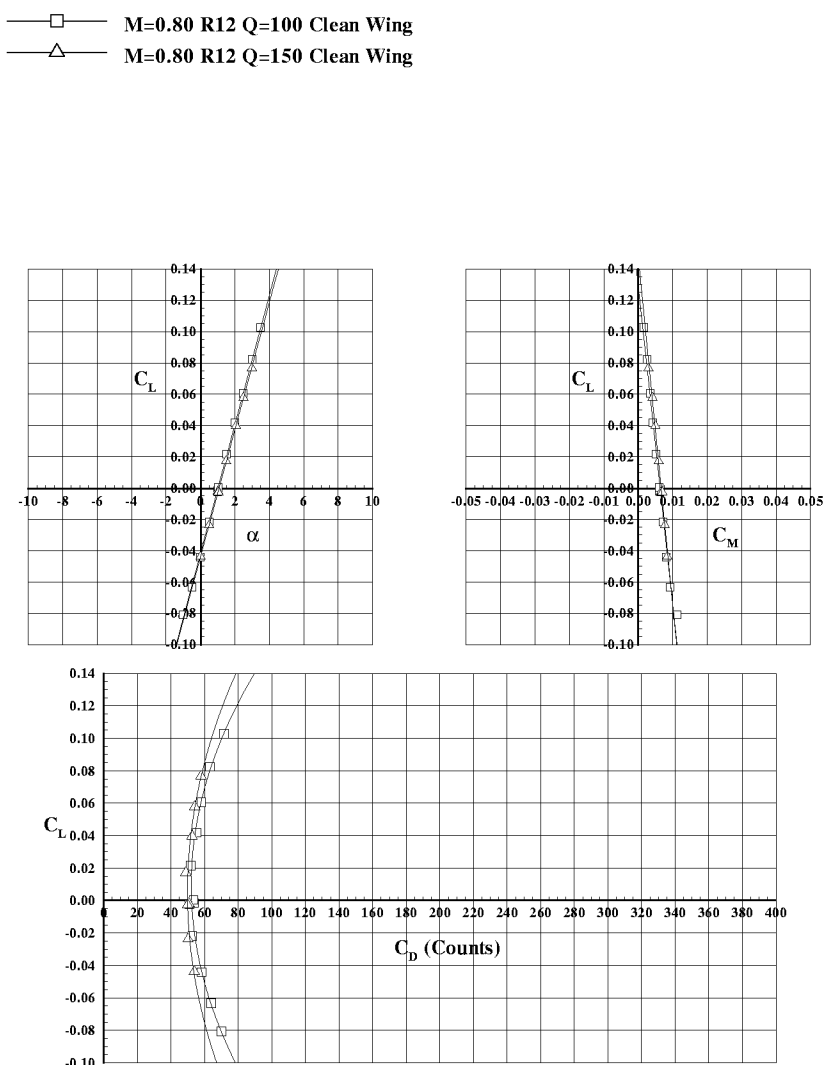


Figure 8-4. Aerodynamic data for various values of dynamic pressure.

8.3.2 Loads Data as a Function of Mach Number

During TDT T521, the HSR-FSM was tested at Mach numbers ranging from 0.8 to 1.15. Figure 8-5 shows how the aerodynamic data vary with Mach number. The data plotted here represent the full range of Mach numbers tested at a dynamic pressure of 150 psf. In this set of figures, it appears that the lift and moment data are significantly affected by the wing flexibility, and it is difficult to draw meaningful conclusions about their response to variation of the freestream Mach number. Rigid wing aerodynamic data is typically characterized by an increasing lift curve slope with Mach number which peaks in the transonic range, then falls off in the supersonic speed regime. Similarly, the slope of the pitching moment curve tends to decrease as the Mach number is increased due to the aft shift in the wing center of pressure. The flexibility of the HSR-FSM wing has significantly diluted these features in the aerodynamic data. From Mach 0.8 to 0.95, a discernible shift in the center of pressure can be seen in the pitching moment data, but beyond Mach 0.95, the flexibility of the wing counteracts this characteristic and very little change in the pitching moment slope is observed. As with rigid wings, the HSR-FSM drag steadily increases with Mach number, with the gradient increasing in the transonic range.

TDT T521 HSR-FSM (Balance)

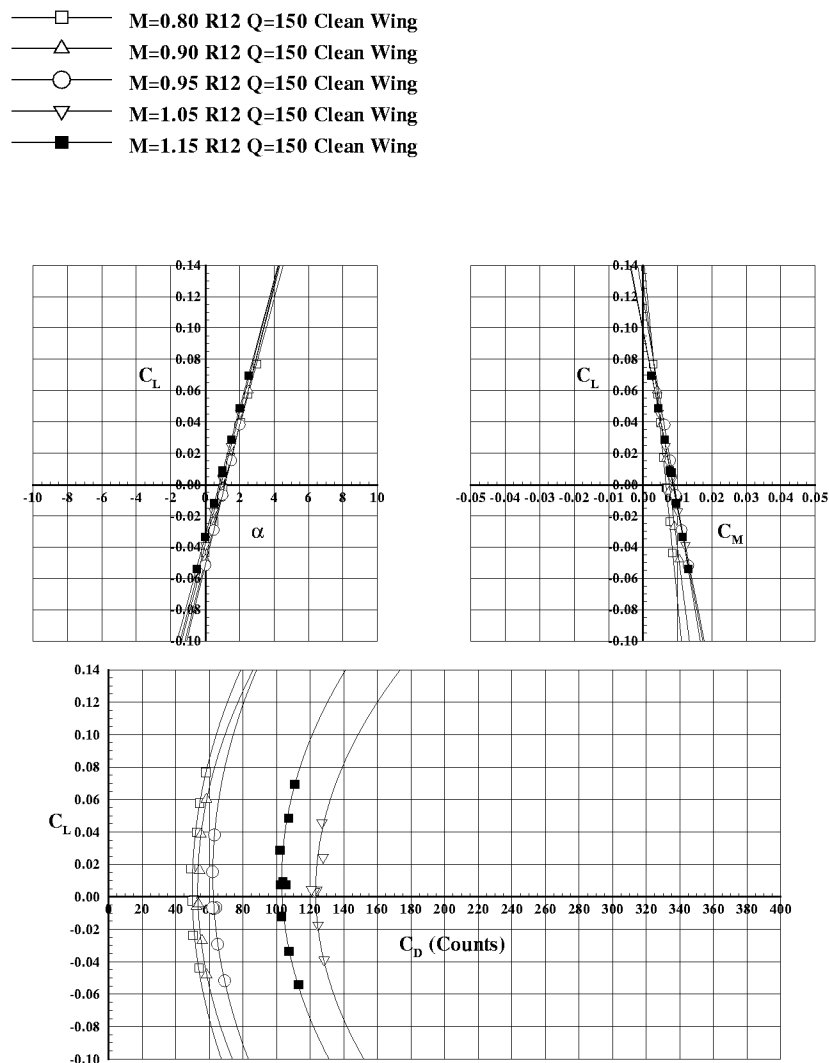


Figure 8-5. Aerodynamic data as a function of Mach number.

8.3.3 Impact of Nacelles on Wing Aerodynamics

A pair of flow-through engine nacelles representative of those included on the Reference H configuration were also tested during this wind tunnel entry. The impact of these nacelles on the aerodynamics of the vehicle at Mach 0.95 are presented in Figure 8-6. The addition of the nacelles shift the lift curve to the left, but it has a minimal impact on the slope of the curve. This is not surprising since the slope of the lift curve is most impacted by the wing planform. Addition of the engine nacelles effectively changes the camber distribution on the inboard portion of the wing which translates into a shift in the model lift coefficient at zero angle-of-attack. The slope of the pitching moment curve is increased with the addition of the nacelles, indicating that the nacelles reduce the static stability of this configuration. As expected, the drag increases substantially with the addition of the nacelles. Figure 8-7 makes a similar comparison at $M=1.15$. The clean-wing and the nacelles-on data at $M=1.15$ are similar to the $M=0.95$ data in all respects.

TDT T521 HSR-FSM (Balance)

—□— $M=0.95$ R12 Q=150 Clean Wing
 —△— $M=0.95$ R12 Q=150 Nacelles On

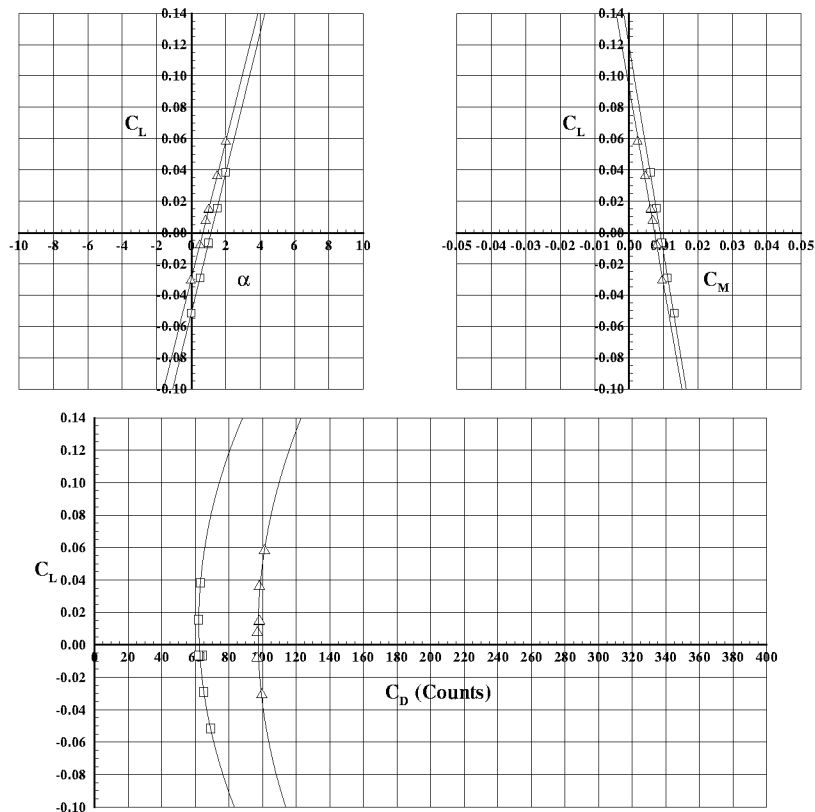


Figure 8-6. Comparison of clean-wing and nacelles-on data at $M=0.95$.

TDT T521 HSR-FSM (Balance)

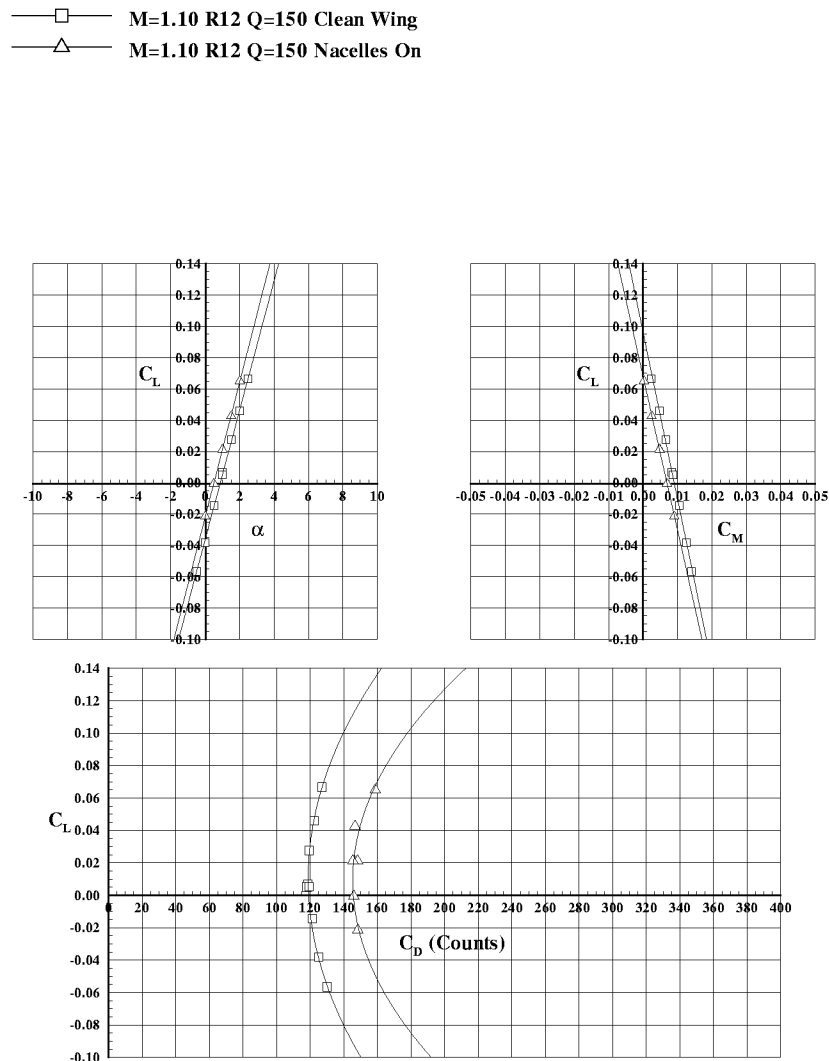


Figure 8-7. Comparison of clean-wing and nacelles-on data at $M=1.15$.

8.3.4 Aerodynamic Response to Control Surface Deflection

Aerodynamic data were acquired as a function of flap deflection at constant angle-of-attack for both the clean-wing and wing-with-nacelles configurations. Steady deflected flap and oscillating flap data were taken at Mach numbers ranging from 0.8 to 1.10. The majority of data were acquired at a dynamic pressure of 150 psf, but selected data were also taken at 100 and 125 psf. Time history records for the oscillating flap cases are available in digital form, but only the steady deflected flap data are discussed in this report.

Figure 8-8 shows the response of the HSR-FSM lift, pitching moment, and drag due to flap deflection for a Mach number range of 0.85 to 1.10. This plot presents a wide variation in control surface effectiveness with Mach number. The lift curve slope at Mach 1.10 is approximately one-

half that at Mach 0.85. As with the HSR-Rigid Semispan Model (HSR-RSM) rigid wing data, this variation is very likely due to shock interaction with the control surface in the transonic range. The pitching moment data show similar trends with the slope steadily decreasing with increasing Mach number.

TDT T521 HSR-FSM (Balance)

- M=0.85 R12 Q=150 Clean Wing
- △— M=0.95 R12 Q=150 Clean Wing
- M=0.98 R12 Q=150 Clean Wing
- ▽— M=1.10 R12 Q=150 Clean Wing

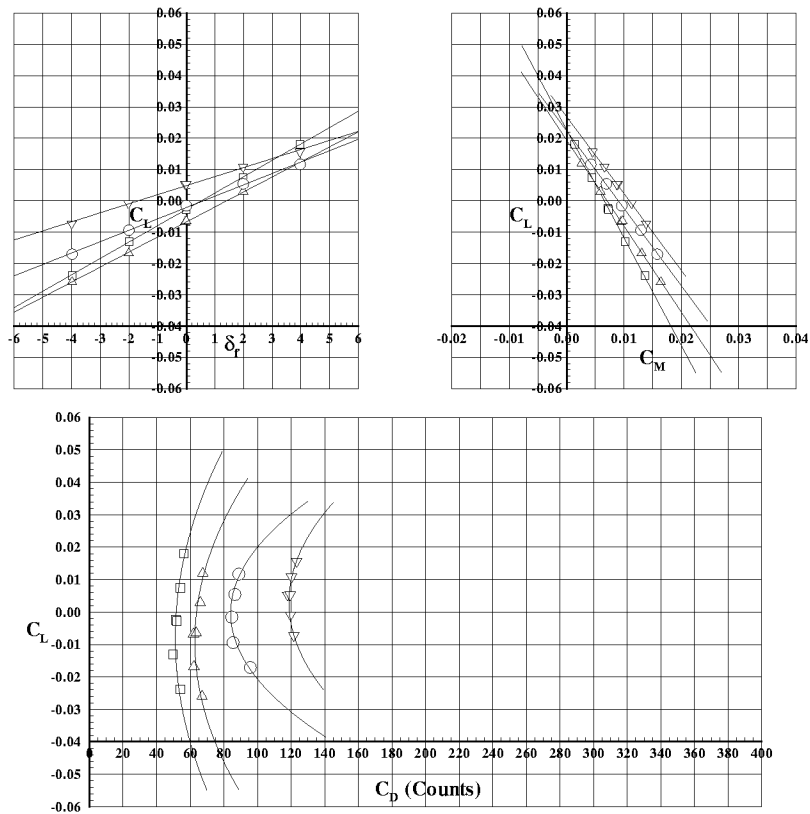


Figure 8-8. HSR-FSM clean-wing steady flap deflection data.

Figure 8-9 shows the steady flap deflection loads for the wing with the nacelles. The trends observed in this plot are similar to those for the clean-wing data except for the drag polar. The wing-with-nacelles data show a noticeable increase in the lift coefficient for minimum drag as Mach number increases. This characteristic is consistent with the nacelles-on flap polar data acquired on the HSR-RSM.

TDT T521 HSR-FSM (Balance)

- M=0.80 R12 Q=150 Nacelles On
- △— M=0.95 R12 Q=150 Nacelles On
- M=1.05 R12 Q=150 Nacelles On

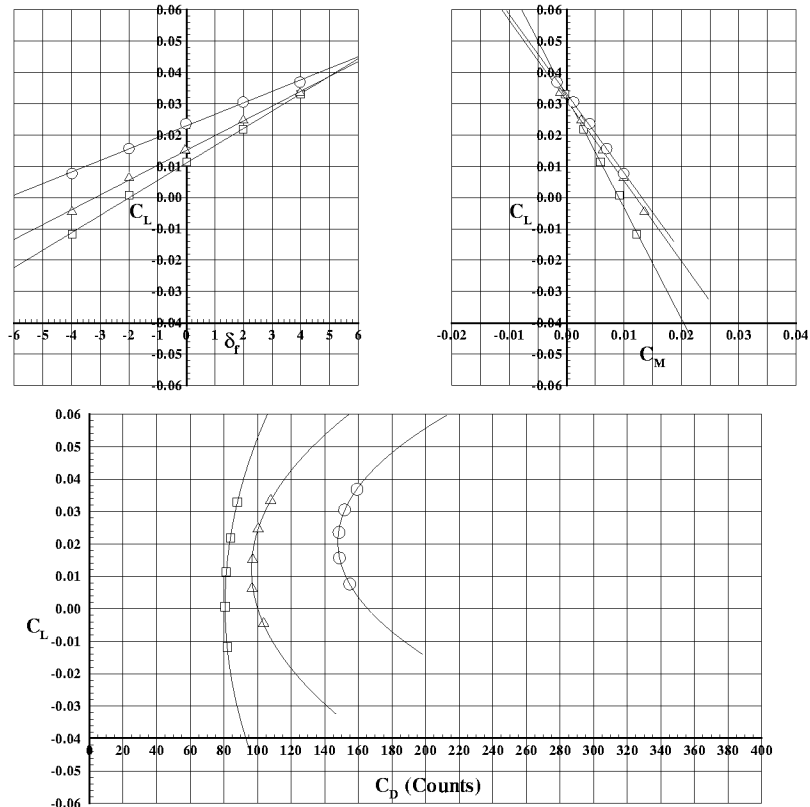


Figure 8-9. HSR-FSM wing-with-nacelles steady flap deflection data.

8.3.5 Comparison of Flexible and Rigid Force Data

The force data obtained during the HSR-FSM static testing has been compared with the rigid-wing force data acquired during the previous test of the HSR-RSM. Lift, pitching moment and drag data are compared by plotting the lift curve slope, pitching moment curve slope, and drag coefficient at a constant lift coefficient versus Mach number. Figure 8-10 shows the lift curve slope as a function of Mach number at a dynamic pressure of 150 psf. In this and subsequent plots, the experimental data is fit using a cubic B-spline denoted by the solid line for the rigid model and the dashed line for the flexible model. The lift curve slope follows the same basic trend for both the rigid and flexible models, increasing with Mach to just below Mach 1.0, then falling off at supersonic speeds. However, static aeroelastic effects on the magnitude of the lift curve slope are significant, especially in the supersonic range. Subsonically, structural flexibility results in about a 2.5%

reduction in the wing lift curve slope. This margin rapidly increases through the transonic range, ultimately accounting for approximately an 11% drop in lift curve slope at Mach 1.15.

A similar trend is seen when the rigid and flexible pitching moment slopes are compared in Figure 8-11. Again, the same overall character is seen in both the rigid and flexible data. Subsonically, flexibility increases the pitching moment slope by approximately 15%, and this difference increases to 28% supersonically. This is equivalent to an aft shift in the aerodynamic center due to model flexibility of approximately 0.7 inches model scale (8.3 inches full scale) at subsonic speeds and 2.8 inches model scale (34 inches full scale) at supersonic speeds.

Flexible/Rigid Force Data Comparison

HSR Semispan Models (Clean Wing)

R-12, $q = 150$ psf

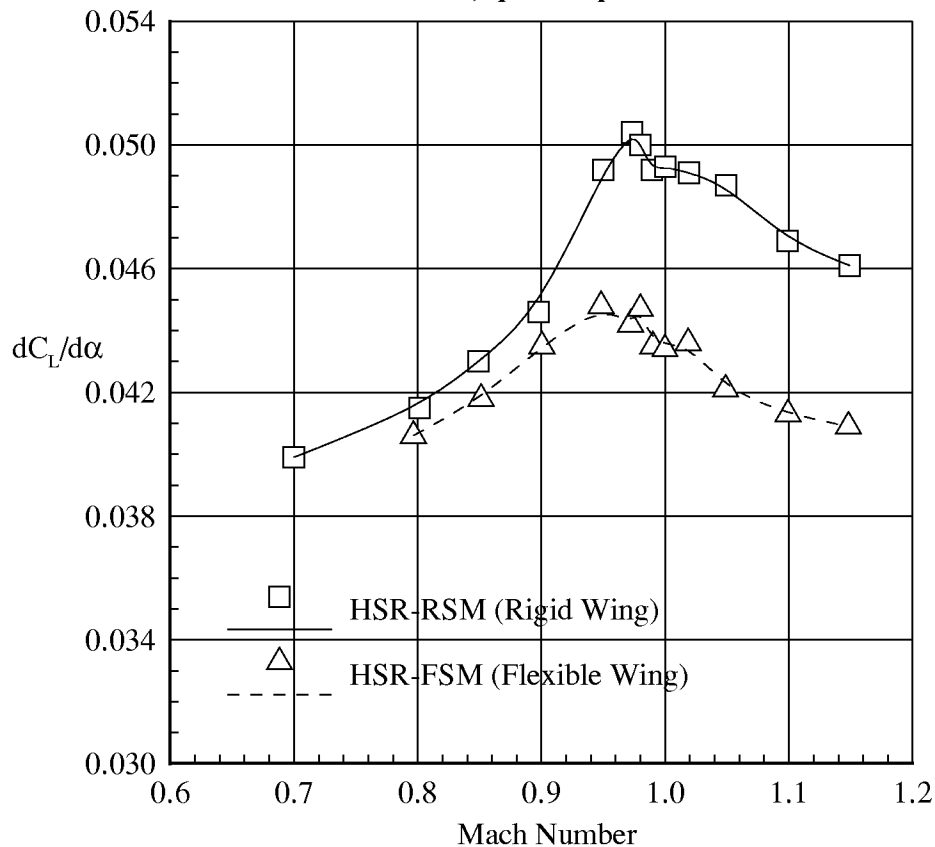


Figure 8-10. Comparison of clean wing rigid (HSR-RSM) and flexible (HSR-FSM) lift curve slopes as a function of Mach number.

Flexible/Rigid Force Data Comparison

HSR Semispan Models (Clean Wing)

R-12, $q = 150$ psf

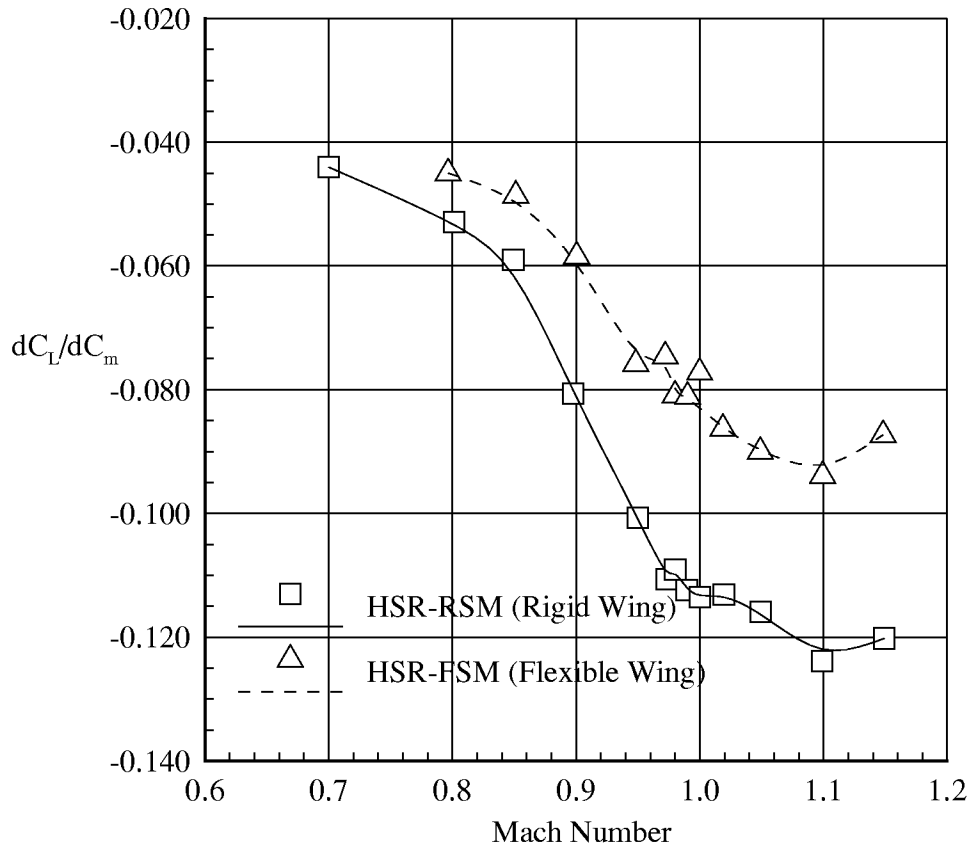


Figure 8-11. Comparison of clean wing rigid (HSR-RSM) and flexible (HSR-FSM) pitching moment curve slope as a function of Mach number.

Finally, the drag coefficient at a constant lift coefficient of 0.1 is plotted against Mach number in Figure 8-12. Contrary to the previous cases, flexibility has the largest impact on drag at subsonic speeds. Flexibility reduces the subsonic drag of the wing by approximately 10 counts, or about 13.5% at Mach 0.8. However, as the wing progresses through transonic drag rise and into the supersonic regime, flexibility has little impact on the drag. Note that these drag values have not been trimmed for the change in pitching moment due to flexibility, so generalizations as to the role of flexibility in the overall performance of the vehicle should not be inferred from the drag data of Figure 8-12.

Flexible/Rigid Force Data Comparison

HSR Semispan Models (Clean Wing)

R-12, $q = 150$ psf

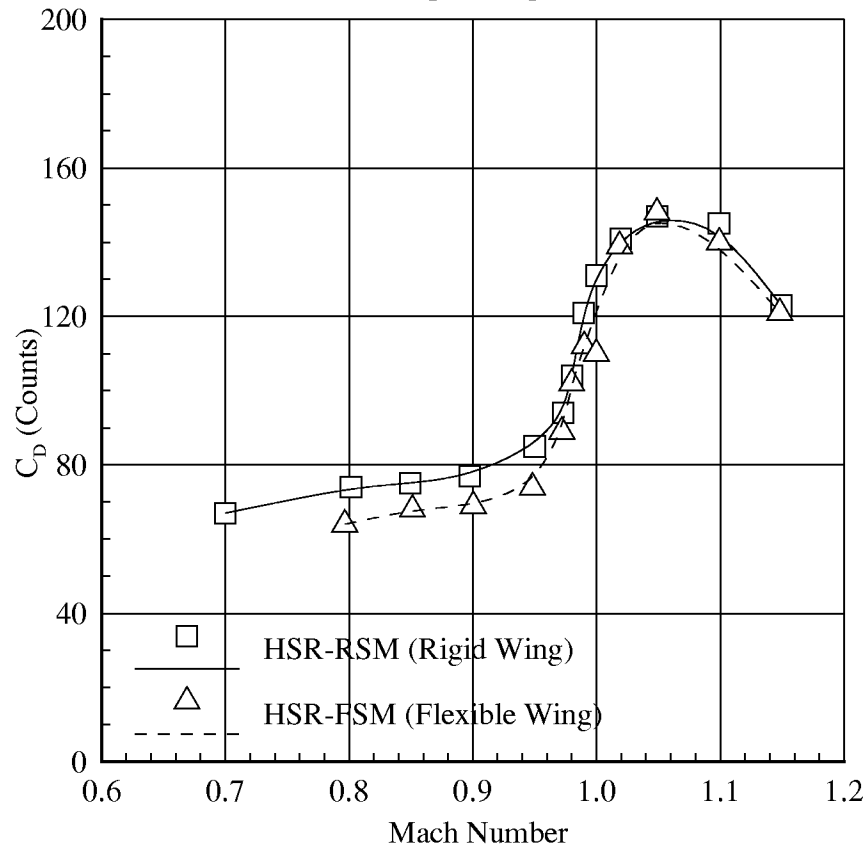


Figure 8-12. Comparison of clean wing rigid (HSR-RSM) and flexible (HSR-FSM) drag coefficient at $C_L = 0.1$ as a function of Mach number.

8.4 Pressure Data Acquisition and Reduction

Wing and fuselage pressure data were acquired for each polar presented in Table 8-1. At each tab point, unsteady pressure data were acquired and time averaged to obtain a mean pressure and maximum and minimum pressure fluctuation for each point on the surface of the wing. Simultaneously, steady fuselage pressures were obtained using a separate data system. Both the wing and fuselage data were then processed into ASCII channel statistics files and stored for future post processing. The wing pressure transducer calibrations were checked before each run by applying a known constant pressure to the reference side of each transducer and recording the pressure reading. Transducers were calibrated if the error between the actual and measured pressure was greater than 3%. The fuselage pressure calibrations were found to be very stable. These transducers were simply calibrated on a periodic basis, typically immediately after the initial warm-up run at the beginning of a day of testing. Prior to and following each run, a wind-off zero was taken and the pressure reading of each transducer was recorded. This allowed us to monitor the health of each transducer over the period of the run and also provided guidance for determining

when the transducers might require calibration. The wind-off zero before each run is also used as a basis for reducing the raw pressure data that is included in the channel statistics file.

The channel statistics files for each tab point are tabulated and processed during testing using a spreadsheet macro. The wing pressure output from this macro for a single tab point is shown in Figure 8-13. For each tab point, tunnel conditions are summarized, pressure data organized along wing chords are tabulated, and the wing pressure coefficient as a function of percentage of local wing chord is plotted. In addition, the wing pressure coefficient at 20% wing chord is plotted as a function of wing semispan. The pressure differential between the upper and lower surface of the wing is calculated for each chord and is also tabulated and plotted in this figure. Note that the aerodynamic loads tabulated in these charts were normalized by different areas and reference lengths than those reported elsewhere in this document. Therefore, the aerodynamic loads printed by the pressure-data macros should only be used for comparison with like-macro output.

Figure 8-14 is a similar output for the fuselage pressure data. Since the fuselage pressure instrumentation measures steady pressure, only the mean pressure coefficient at each fuselage station is tabulated. The fuselage pressure data are organized along constant fuselage station cuts and are tabulated and plotted as a function of the azimuthal angle measured from the TDT wall on the upper surface of the fuselage to the TDT wall on the lower surface of the fuselage.

The output from both the wing and fuselage macros, as well as all of the channel statistics files for each run and tab point taken during this test have been compiled into a CD-ROM volume. Copies of this volume have been previously distributed to the HSR industry partners.

For model safety reasons, the angle-of-attack range at which the HSR-FSM was tested is limited as compared to the test range for the HSR-RSM. The flexible model was typically tested at angles-of-attack ranging from zero to three degrees. In this range, the load on the wing is purposely low, and the differences between the rigid and flexible model pressure distributions are subtle and often difficult to visualize. To give the reader a feel for the overall pressure data quality and character, three comparisons of the rigid and flexible pressure distributions will be presented in this report. Unfortunately, it is difficult to derive further meaningful conclusions about the static aeroelastic performance of this wing from these data.

Run	8					TDT Test # 521 HSR FSM-Bal							
Tab	240					Pressure Distribution Statistics							
						Aileron Position (deg.)							
						Cmd.			Pos.				
Mach	(psf)	Re	γ	α		Mean	0.06	0.00					
0.949	100.1	1.57	1.136	3.00		Amplitude	0.04	0.01					
						(1/2 P-P)							
Tunnel Conditions						Aileron Hinge Moment (in-lbs.)							
H	P	T	R-12				Max.	Min.	Mean				
(psf)	(psf)	(deg F)	Purity				35.56	22.03	29.64				
321.5	195.7	99.7	0.95										
Lift	Pitching	Drag	Rolling	Yawing									
Force	Moment	Force	Moment	Moment									
Coeff.	Coeff.	Coeff.	Coeff.	Coeff.									
0.0444	-0.0405	0.0038	0.0108	0.0002									
						Acquired 17 APR 96 at 21:12:47							
						Adjusted using wind-off zero Tab # 220							
						500 samples/second for 5 seconds							
						Samples 1 through 2500; 100.00% of 2500 samples							
Upper surface 0.10 semispan						Lower surface 0.10 semispan							
x/c	Cp Mean	Cp Min	Cp Max	Std Dev	Chan	x/c	Cp Mean	Cp Min	Cp Max	Std Dev	Chan	Delta-Cp	
0.000	0.011	-0.021	0.042	0.010	151	0.025	0.087	0.066	0.109	0.007	187	0.146	
0.025	-0.059	-0.086	-0.027	0.008	186	0.050	0.070	0.050	0.091	0.006	169	0.126	
0.050	-0.056	-0.082	-0.026	0.008	152	0.100	0.082	0.061	0.105	0.006	170	0.161	
0.100	-0.079	-0.105	-0.049	0.009	153	0.150	0.092	0.069	0.111	0.006	171	0.205	
0.150	-0.114	-0.147	-0.078	0.010	154	0.200	0.079	0.060	0.104	0.006	172	0.181	
0.200	-0.102	-0.130	-0.063	0.010	155	0.250	0.057	0.037	0.077	0.006	173	0.157	
0.250	-0.100	-0.126	-0.057	0.009	156	0.300	0.048	0.026	0.073	0.007	174	0.139	
0.300	-0.091	-0.122	-0.048	0.011	157	0.350	0.035	0.015	0.060	0.007	175	0.145	
0.350	-0.110	-0.143	-0.062	0.013	158	0.400	0.018	-0.006	0.043	0.007	176	0.651	
0.400	-0.633	-0.676	-0.580	0.020	159	0.450	-0.002	-0.025	0.028	0.008	177	0.091	
0.450	-0.093	-0.127	-0.042	0.013	160	0.500	-0.005	-0.027	0.034	0.008	178	0.083	
0.500	-0.088	-0.119	-0.040	0.012	161	0.550	-0.021	-0.043	0.014	0.008	179	0.079	
0.550	-0.100	-0.135	-0.038	0.013	162	0.600	-0.040	-0.066	0.002	0.009	180	0.076	
0.600	-0.116	-0.153	-0.037	0.017	163	0.650	-0.045	-0.068	0.002	0.010	181	0.070	
0.650	-0.114	-0.155	-0.035	0.017	164	0.700	-0.064	-0.094	-0.008	0.011	182	0.068	
0.700	-0.133	-0.186	-0.055	0.021	165	0.750	-0.095	-0.123	-0.046	0.010	183	0.018	
0.750	-0.113	-0.168	-0.034	0.021	166	0.800	-0.129	-0.157	-0.082	0.011	184	-0.053	
0.800	-0.075	-0.125	-0.015	0.017	167	0.850	-0.010	-0.022	0.002	0.003	185	0.077	
0.850	-0.086	-0.138	-0.032	0.018	168								
Upper surface 0.30 semispan						Lower surface 0.30 semispan							
x/c	Cp Mean	Cp Min	Cp Max	Std Dev	Chan	x/c	Cp Mean	Cp Min	Cp Max	Std Dev	Chan	Delta-Cp	
0.000	0.036	-0.002	0.069	0.010	111	0.025	0.049	0.022	0.083	0.009	146	0.185	
0.025	-0.136	-0.175	-0.103	0.011	145	0.050	0.028	0.003	0.060	0.009	129	0.212	
0.050	-0.184	-0.216	-0.147	0.012	112	0.100	0.033	0.010	0.067	0.009	130	0.100	
0.100	-0.067	-1.145	0.000	0.177	113	0.150	0.033	0.010	0.066	0.009	131	0.192	
0.150	-0.159	-0.197	-0.108	0.016	114	0.200	0.032	0.007	0.073	0.009	132	0.142	
0.200	-0.109	-0.147	-0.067	0.013	115	0.250	0.029	0.005	0.071	0.009	133	0.152	
0.250	-0.124	-0.159	-0.074	0.014	116	0.300	0.030	0.005	0.068	0.009	134	0.165	
0.300	-0.136	-0.172	-0.088	0.013	117	0.350	0.016	-0.008	0.058	0.010	135	0.016	
0.350	0.000	0.000	0.000	0.000	118	0.400	0.007	-0.019	0.049	0.011	136	0.155	
0.400	-0.148	-0.174	-0.077	0.013	119	0.450	-0.002	-0.029	0.041	0.011	137	0.155	
0.450	-0.157	-0.232	-0.060	0.033	120	0.500	-0.012	-0.037	0.034	0.011	138	0.120	
0.500	-0.132	-0.168	-0.056	0.016	121	0.550	-0.038	-0.062	0.011	0.011	139	0.122	
0.550	-0.160	-0.207	-0.038	0.026	122	0.600	-0.060	-0.085	-0.007	0.011	140	0.112	
0.600	-0.172	-0.214	-0.037	0.023	123	0.650	-0.123	-0.147	-0.060	0.012	141	0.042	
0.650	-0.165	-0.237	-0.016	0.038	124	0.700	-0.212	-0.237	-0.145	0.013	142	-0.106	
0.700	-0.107	-0.166	-0.002	0.028	125	0.750	-0.332	-0.364	-0.212	0.018	143	-0.276	
0.750	-0.055	-0.103	0.031	0.022	126	0.800	-0.272	-0.377	-0.089	0.060	144	-0.148	
0.800	-0.124	-0.179	-0.046	0.022	127								

Figure 8-13. Output from the wing pressure package macro.

Run	8				TDT Test # 521 HSR FSM-Bal																															
Tab	240				Pressure Distribution Statistics																															
					Aileron Position (deg.)																															
					Cmd.				Pos.																											
Mach	q	Re	γ	α																																
(psf)	(10**6/ft)		(deg)																																	
Mean					0.06 0.00																															
Amplitude					0.04 0.01																															
					(1/2 P-P)																															
Tunnel Conditions					Aileron Hinge Moment (in-lbs.)																															
H	P	T	R-12																																	
(psf)	(psf)	(deg F)	Purity																																	
Max.	Min.	Mean																																		
321.5	195.7	99.7	0.95							35.56 22.03 29.64																										
					Acquired 17 APR 96 at 21:12:47																															
					Adjusted using wind-off zero Tab # 220																															
					500 samples/second for 5 seconds																															
					Samples 1 through 2500; 100.00% of 2500 samples																															
Lift					Pitching					Drag					Rolling					Yawing																
Force					Moment					Force					Moment					Moment																
Coeff.					Coeff.					Coeff.					Coeff.					Coeff.																
0.0444					-0.0405					0.0038					0.0108					0.0002																
Upper surface 0.60 semispan													Lower surface 0.60 semispan																							
x/c						Cp Mean					Cp Min					Cp Max					Std Dev					Chan					Delta-Cp					
0.000						0.094					0.019					0.177					0.023					65					0.050					
0.050						-0.355					-0.482					-0.233					0.037					66					0.100					
0.100						-0.210					-0.245					-0.133					0.018					67					0.150					
0.150						-0.132					-0.189					-0.048					0.021					68					0.200					
0.200						-0.151					-0.186					-0.079					0.012					69					0.250					
0.250						-0.183					-0.207					-0.073					0.014					70					0.300					
0.300						-0.216					-0.250					-0.038					0.025					71					0.350					
0.350						-0.235					-0.287					-0.054					0.036					72					0.400					
0.400						-0.223					-0.297					-0.040					0.045					73					0.450					
0.450						-0.205					-0.284					-0.022					0.042					74					0.500					
0.500						-0.234					-0.313					-0.038					0.042					75					0.550					
0.550						-0.256					-0.325					-0.054					0.042					76					0.600					
0.600						-0.205					-0.263					-0.027					0.035					77					0.650					
0.650						-0.206					-0.257					-0.019					0.035					78					0.700					
0.700						-0.199					-0.246					-0.027					0.034					79					0.750					
0.750						-0.252					-0.296					-0.072					0.037					80					0.800					
0.800						-0.411					-0.483					-0.091					0.081					81					0.850					
0.850						-0.211					-0.442					0.004					0.119					82					0.900					
0.900						-0.045					-0.229					0.052					0.050					83					0.950					
0.950						0.057					-0.005					0.116					0.024					84					0.950					
1.000						0.191					0.151					0.227					0.014					85										
Upper Surface 0.95 Semispan													Lower Surface 0.95 Semispan																							
x/c						Cp Mean					Cp Min					Cp Max					Std Dev					Chan					Delta-Cp					
0.000						0.288					0.149					0.348					0.027					31					0.100					
0.100						-0.301					-0.355					-0.145					0.018					32					0.200					
0.200						-0.457					-0.500					-0.169					0.023					33					0.300					
0.300						-0.409					-0.492					-0.066					0.067					34					0.400					
0.400						-0.289					-0.436					-0.017					0.104					35					0.500					
0.500						-0.135					-0.329					0.038					0.089					36					0.600					
0.600						-0.116					-0.265					0.038					0.057					37					0.700					
0.700						-0.204					-0.339					-0.038					0.057					38					0.800					
0.800						-0.130					-0.405					-0.009					0.057					39					0.900					
0.900						0.016					-0.029					0.087					0.019					40					0.900					
Upper Surface 0.20 Chord													Lower Surface 0.20 Chord																							
2y/b						Cp Mean					Cp Min					Cp Max					Std Dev					Chan					Delta-Cp					
0.100						-0.102					-0.130					-0.063					0.010					155					0.100					
0.200						-0.097					-0.124					-0.057					0.011					147					0.200					
0.300						-0.109					-0.147					-0.067					0.013					115					0.300					
0.450						-0.128					-0.203					-0.076					0.021					105					0.450					
0.600						-0.151					-0.186					-0.079					0.012					69					0.600					
0.750						-0.244					-0.308					-0.041					0.041					62					0.750					
0.950						-0.457					-0.500					-0.169					0.023					33					0.950					

Figure 8-13(Continued).Output from the wing pressure package macro.

Run	8		TDT Test # 521 HSR FSM-Bal		
Tab	240		Pressure Distribution Statistics		
	q	Re	γ	α	Aileron Position (deg.)
	(psf)	(10**6/ft)		(deg)	Cmd. Pos.
Mach					Mean
0.949	100.1	1.57	1.136	3.00	0.06 0.00
					Amplitude
					0.04 0.01
					(1/2 P-P)
Lift	Pitching	Drag	Rolling	Yawing	Acquired 17 APR 96 at 21:12:47 Adjusted using wind-off zero Tab # 220 500 samples/second for 5 seconds Samples 1 through 2500; 100.00% of 2500 samples
Force	Moment	Force	Moment	Moment	
Coeff.	Coeff.	Coeff.	Coeff.	Coeff.	
0.0444	-0.0405	0.0038	0.0108	0.0002	

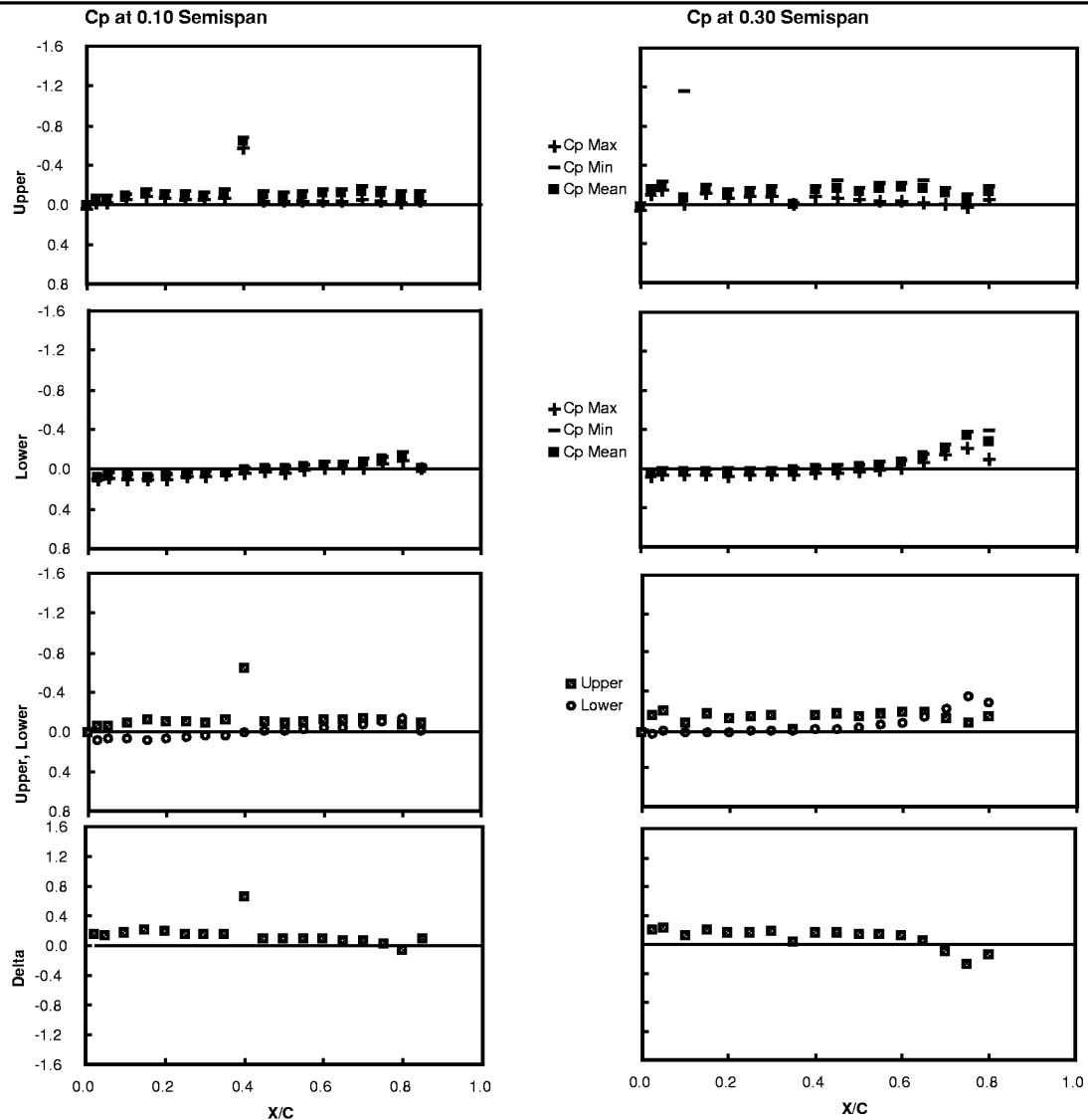


Figure 8-13(Continued).Output from the wing pressure package macro.

Run	8				TDT Test # 521 HSR FSM-Bal		
Tab	240				Pressure Distribution Statistics		
	q	Re	γ	α	Aileron Position (deg.)		
					Cmd.	Pos.	
Mach	(psf)	(10**6/ft)		(deg)	Mean	0.06	0.00
0.949	100.1	1.57	1.136	3.00	Amplitude	0.04	0.01
					(1/2 P-P)		
Lift	Pitching	Drag	Rolling	Yawing	Acquired 17 APR 96 at 21:12:47		
Force	Moment	Force	Moment	Moment	Adjusted using wind-off zero Tab # 220		
Coeff.	Coeff.	Coeff.	Coeff.	Coeff.	500 samples/second for 5 seconds		
0.0444	-0.0405	0.0038	0.0108	0.0002	Samples 1 through 2500; 100.00% of 2500 samples		

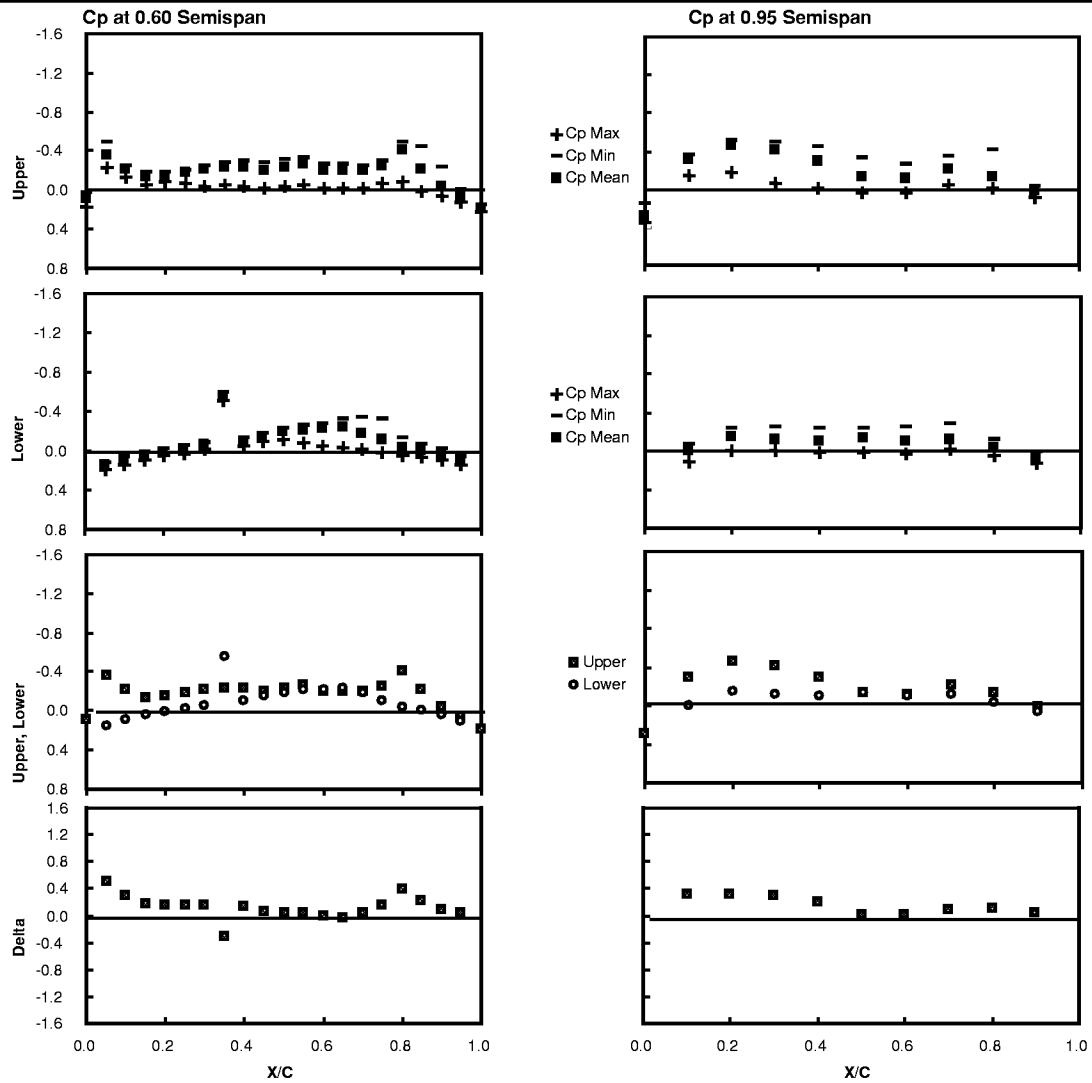


Figure 8-13(Continued).Output from the wing pressure package macro.

Run	8					TDT Test # 521 HSR FSM-Bal			
Tab	240					Pressure Distribution Statistics			
						Aileron Position (deg.)			
		q	Re	γ	α				
		psi	(10**6/ft)		(deg)	Cmd.	Pos.		
Mach						Mean	0.06	0.00	
0.949		100.1	1.57	1.136	3.00	Amplitude	0.04	0.01	
						(1/2 P-P)			
Lift	Pitching	Drag	Rolling	Yawing	Acquired 17 APR 96 at 21:12:47				
Force	Moment	Force	Moment	Moment	Adjusted using wind-off zero Tab # 220				
Coeff.	Coeff.	Coeff.	Coeff.	Coeff.	500 samples/second for 5 seconds				
0.0444	-0.0405	0.0038	0.0108	0.0002	Samples 1 through 2500; 100.00% of 2500 samples				

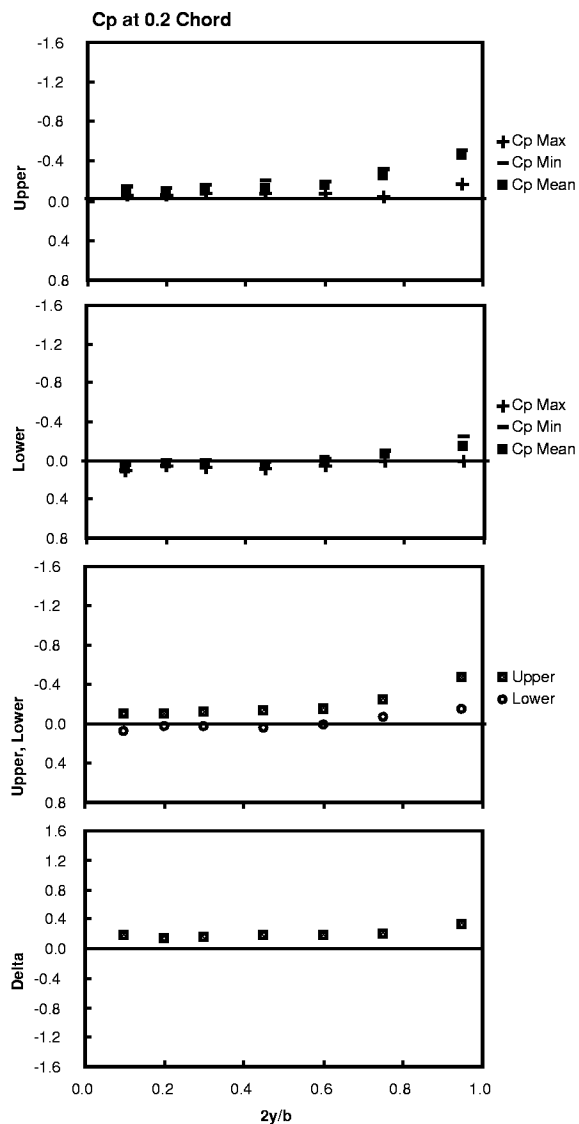


Figure 8-13(Continued).Output from the wing pressure package macro.

Run	8	TDT Test #521 HSR FSM-Bal									
Tab	240	Fuselage Pressures									
Mach	q	α									
	(psf)	(deg)									
0.948	99.90	3.00	Acquired on Apr 17, 1996 at 9:12 PM								
100 Sample Sets Acquired at a Sample Rate of 20 Khz											
Fuselage Stations											
Theta Measured from Upper Fuselage Symmetry Plane											
X = 16"			X = 36"			X = 60"			X = 102"		
Theta	Cp Mean	Chan	Theta	Cp Mean	Chan	Theta	Cp Mean	Chan	Theta	Cp Mean	Chan
9.23	−0.31	1	7.97	−0.04	17	7.97	0.03	33	54.00	−0.08	49
13.78	−0.31	2	15.64	−0.05	18	15.64	0.02	34	57.13	−0.07	50
18.22	−0.31	3	22.78	−0.03	19	22.78	0.03	35	60.23	−0.08	51
26.56	−0.30	4	35.26	−0.05	20	35.26	0.03	36	63.30	−0.09	52
40.71	−0.28	5	54.00	−0.04	21	54.00	0.04	37	66.36	−0.08	53
47.33	−0.29	6	66.36	−0.05	22	66.36	0.06	38	67.93	−0.09	54
80.99	−0.22	7	79.81	−0.04	23	79.81	0.13	39	69.53	−0.09	55
90.00	−0.21	8	90.00	−0.05	24	90.00	0.21	40	71.17	−0.09	56
99.01	−0.22	9	100.19	−0.03	25	100.19	0.09	41	108.83	0.07	57
132.67	−0.27	10	113.64	−0.08	26	113.64	0.07	42	110.47	0.08	58
139.29	−0.20	11	126.00	−0.06	27	126.00	0.05	43	112.07	0.07	59
153.44	−0.17	12	144.74	−0.02	28	144.74	0.04	44	113.64	0.07	60
161.78	−0.18	13	157.22	−0.03	29	157.22	0.04	45	119.77	0.07	61
166.22	−0.17	14	164.36	−0.04	30	164.36	0.04	46	122.87	0.06	62
170.77	−0.17	15	172.03	−0.03	31	172.03	0.04	47	126.00	0.05	63
X = 132" (Upper)			X = 132" (Lower)			X = 182"			X = 204"		
Theta	Cp Mean	Chan	Theta	Cp Mean	Chan	Theta	Cp Mean	Chan	Theta	Cp Mean	Chan
7.97	−0.04	65	107.16	−0.05	81	7.97	0.01	97	7.97	−0.08	113
15.64	−0.03	66	108.83	−0.02	82	15.64	0.00	98	15.64	−0.08	114
22.78	−0.03	67	110.47	−0.01	83	22.78	0.02	99	22.78	−0.08	115
29.24	−0.04	68	112.07	−0.02	84	35.26	0.01	100	35.26	−0.08	116
35.26	−0.04	69	113.64	−0.01	85	54.00	0.04	101	54.00	−0.07	117
41.43	−0.05	70	116.70	−0.02	86	66.36	0.06	102	66.36	−0.08	118
54.00	−0.05	71	119.77	−0.01	87	79.81	0.06	103	79.81	−0.08	119
57.13	−0.06	72	122.87	−0.02	88	90.00	0.07	104	90.00	−0.08	120
60.23	−0.07	73	126.00	−0.01	89	100.19	0.07	105	100.19	−0.08	121
63.30	−0.07	74	138.57	−0.04	90	113.64	0.06	106	113.64	−0.07	122
66.36	−0.06	75	144.74	−0.03	91	126.00	0.05	107	126.00	−0.08	123
67.93	−0.06	76	150.76	−0.04	92	144.74	0.02	108	144.74	−0.07	124
69.53	−0.07	77	157.22	−0.02	93	157.22	0.01	109	157.22	−0.09	125
71.17	−0.05	78	164.36	−0.03	94	164.36	0.01	110	164.36	−0.11	126
			172.03	−0.03	95	172.03	0.00	111	172.03	−0.10	127

Figure 8-14. Output from the fuselage pressure package macro.

Run 8
Tab 240

TDT Test #521 HSR FSM-Bal Fuselage Pressures

Mach q α
(psf) (deg)
0.948 99.90 3.00

Acquired on Apr 17, 1996 at 9:12 PM
100 Sample Sets Acquired at a Sample Rate of 20 KHz

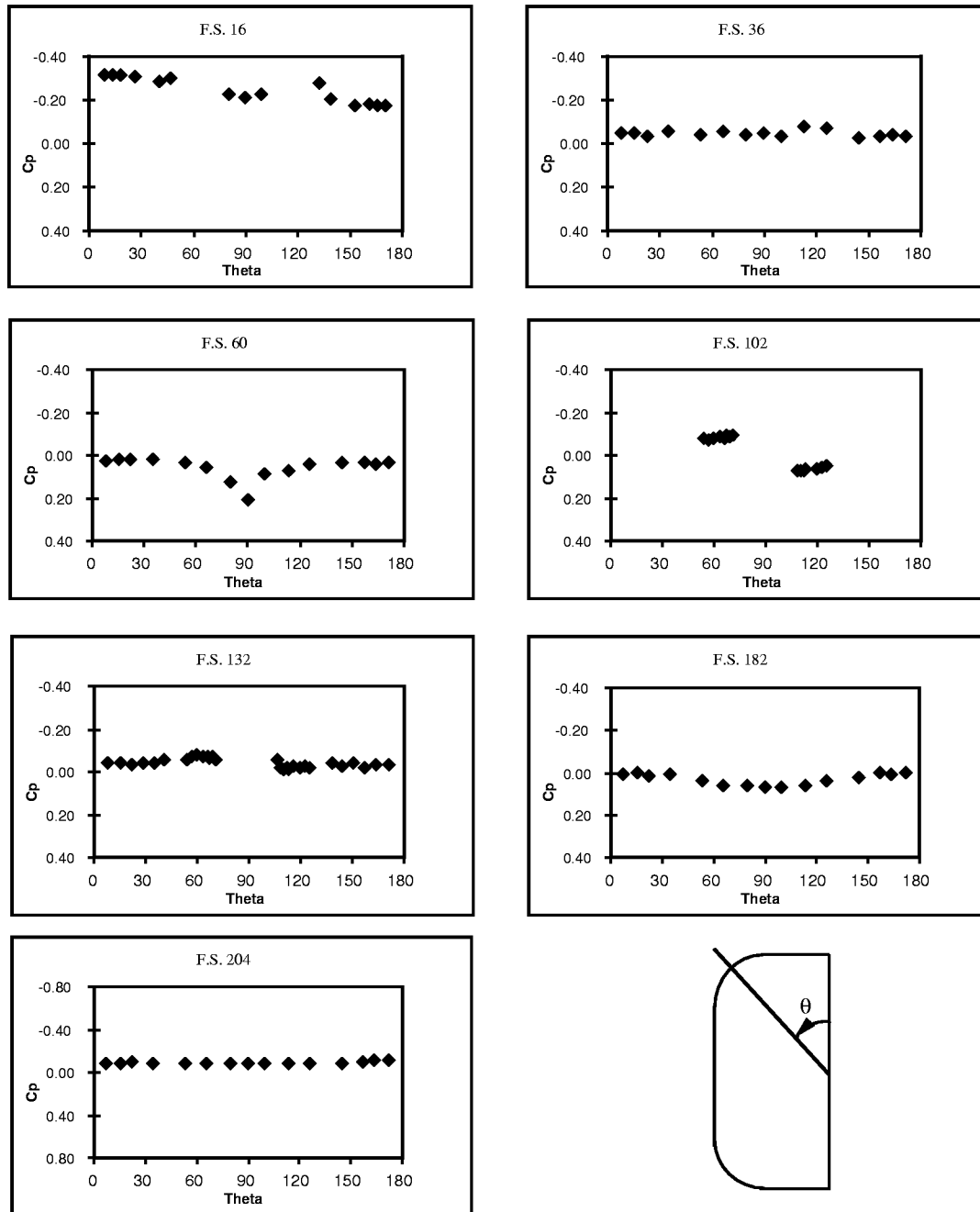


Figure 8-14(Continued).Output from the fuselage pressure package macro.

8.4.1 Clean Wing Flexible/Rigid Pressure Comparison

Clean wing flexible and rigid pressure distributions have been compared at Mach 0.95 and 1.15. Figure 8-15 presents the comparison at Mach 0.95, two degrees angle-of-attack and a dynamic pressure of 150 psf. As expected, the inboard sections of the wing compare very well with the minor inconsistencies attributable to local differences in the two models. At the 60% span station, flexibility effects can be seen in the position of the lower surface shock at approximately 80% chord. The flexible model places the shock forward of the rigid model indicating that the local wing section angle-of-attack is lower than for the rigid wing. In other words, the wing is washing out under positive aerodynamic load, which is to be expected for an aft-swept wing. The upper surface of the flexible wing is also showing a local flow acceleration at about 80% chord which is not portrayed in the rigid wing pressures. It is difficult to characterize this difference in the context of structural flexibility, and it is speculated that there may be a local surface anomaly in the flexible model which causes this acceleration. This area is very close to where the removable trailing edge section attaches to the main wing. If there is an imperfection in the surface, this is a likely place for it to occur, especially for a wing which is flexing under aerodynamic load. At 95% span the pressure distributions are very difficult to interpret and compare. They generally follow the same trend, but neither the rigid nor the flexible model generate very much load, so it is hard to determine the effect of flexibility with any confidence.

At supersonic speeds, the differences between the flexible and rigid models are more difficult to characterize. Figure 8-16 presents the clean wing rigid and flexible pressure distributions at Mach 1.15, two degrees angle-of-attack, and a dynamic pressure of 150 psf. Unlike the Mach 0.95 case, there are discernible differences in the pressure distributions on the two inboard stations. At 10% span the rigid and flexible pressure distributions on the forward section of the wing compare well, but there are differences in the pressures between 60 and 80 percent chord. At 30% span, the pressure distributions differ over the majority of the wing chord, but seem to coalesce near 80% chord. Similar characteristics are observed in the 60 and 95 percent span stations in that the rigid and flexible pressures exhibit the same overall character with observable local differences. At this level of aerodynamic load, it is extremely difficult to confidently quantify the effect of flexibility on the supersonic pressure distribution, even though the aerodynamic loads data tell us that flexibility has a significant effect on the performance of the wing.

Rigid/Flexible Pressure Distribution

$M=0.95$, $\alpha=2.0^\circ$, $q=150\text{psf}$.

$\eta=0.10$

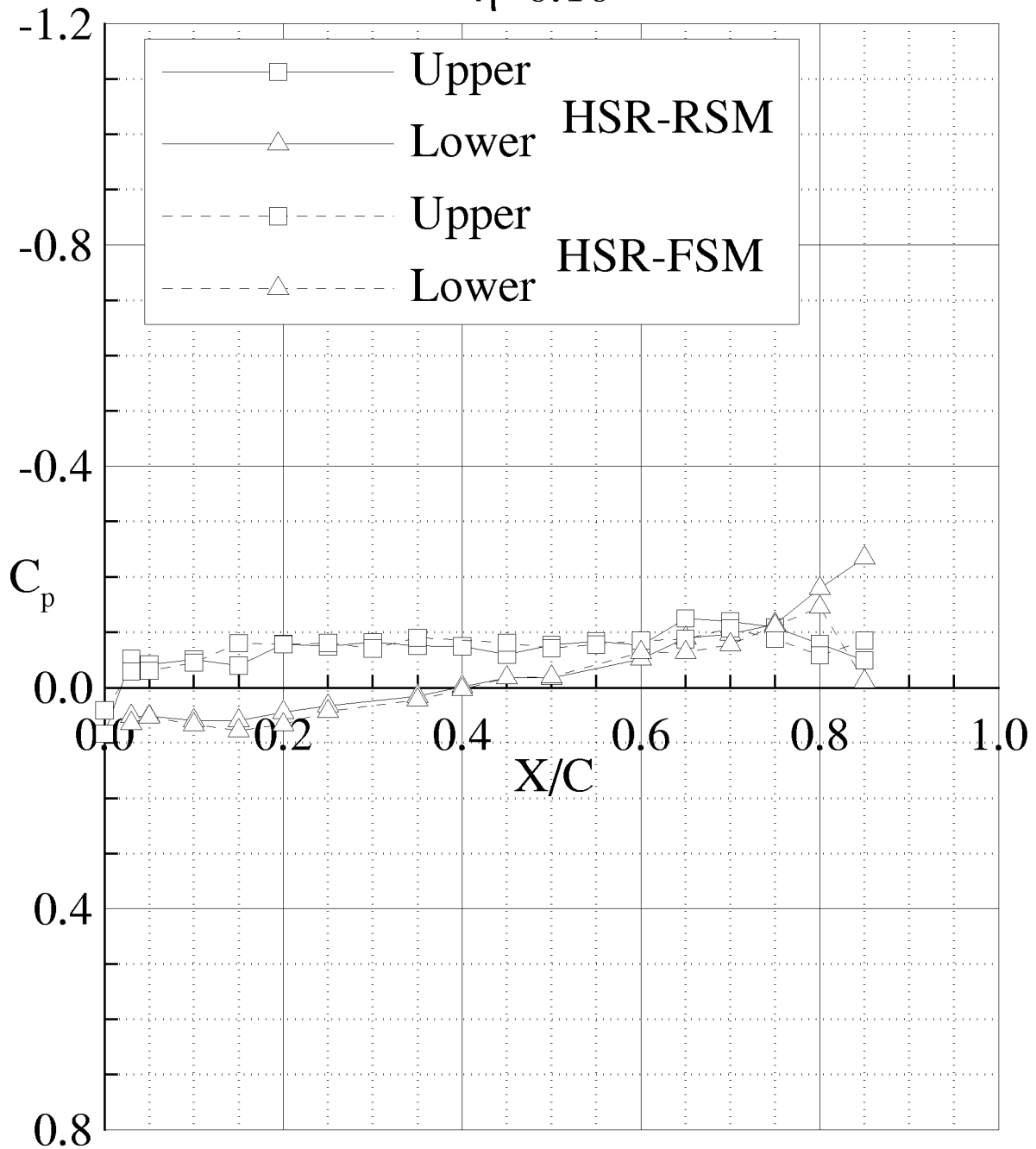


Figure 8-15. Comparison of clean wing flexible and rigid pressure distributions at $M=0.95$, $\alpha=2.0^\circ$.

Rigid/Flexible Pressure Distribution

$M=0.95$, $\alpha=2.0^\circ$, $q=150\text{psf}$.

$\eta=0.30$

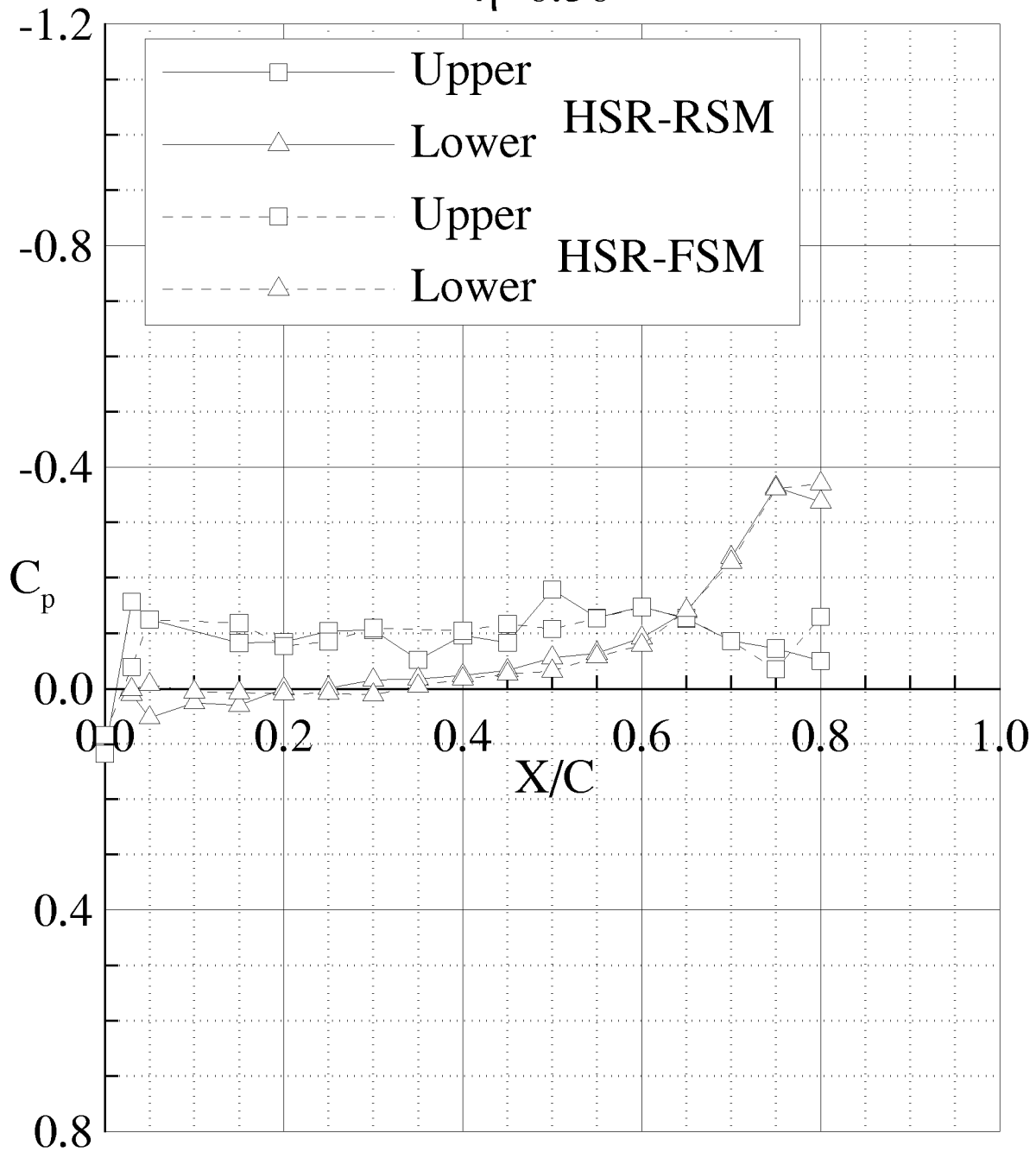


Figure 8-15 (Continued). Comparison of clean wing flexible and rigid pressure distributions at $M=0.95$, $\alpha=2.0^\circ$.

Rigid/Flexible Pressure Distribution

$M=0.95$, $\alpha=2.0^\circ$, $q=150\text{psf}$.

$\eta=0.60$

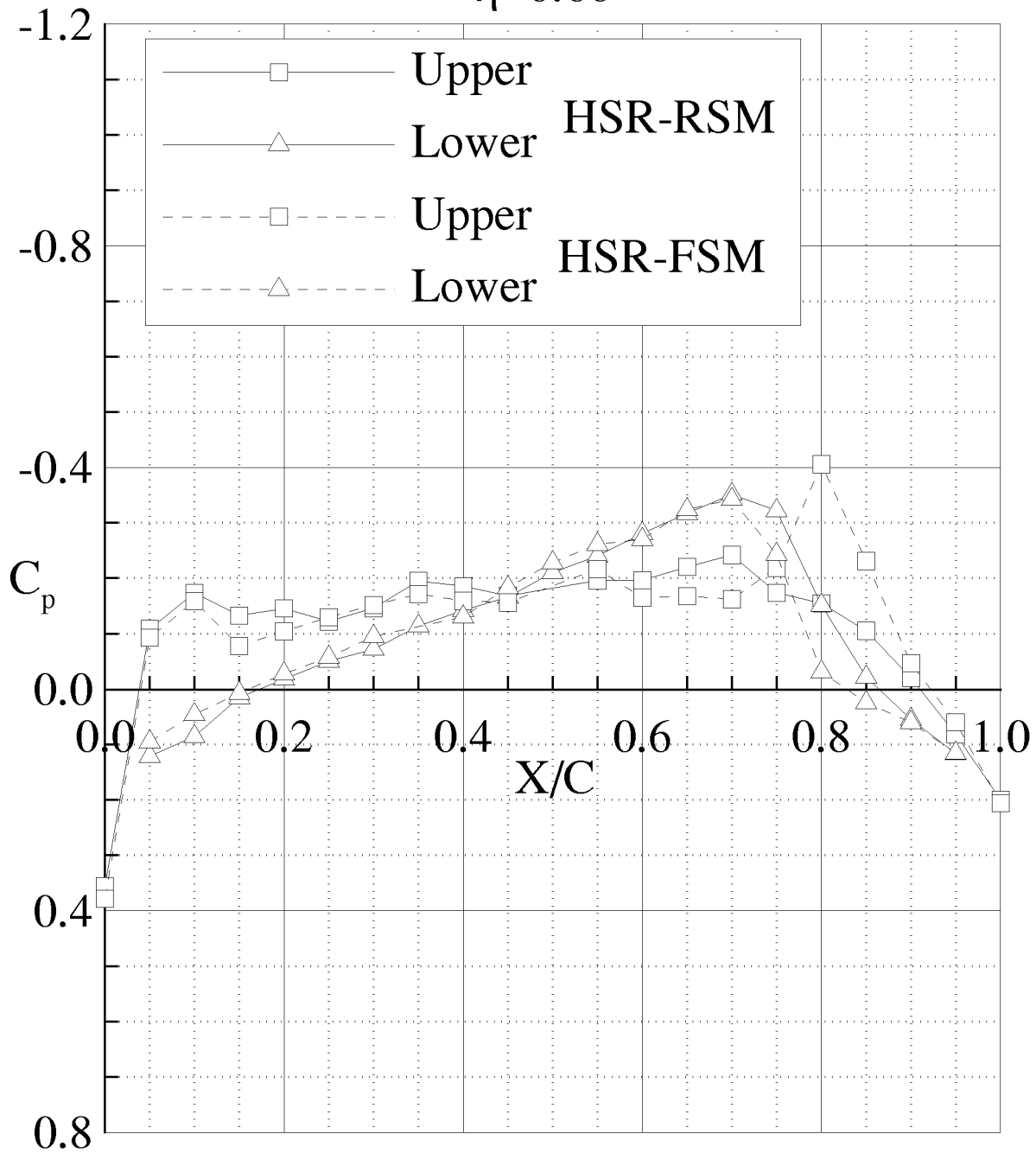


Figure 8-15 (Continued). Comparison of clean wing flexible and rigid pressure distributions at $M=0.95$, $\alpha=2.0^\circ$.

Rigid/Flexible Pressure Distribution

$M=0.95$, $\alpha=2.0^\circ$, $q=150\text{psf}$.

$\eta=0.95$

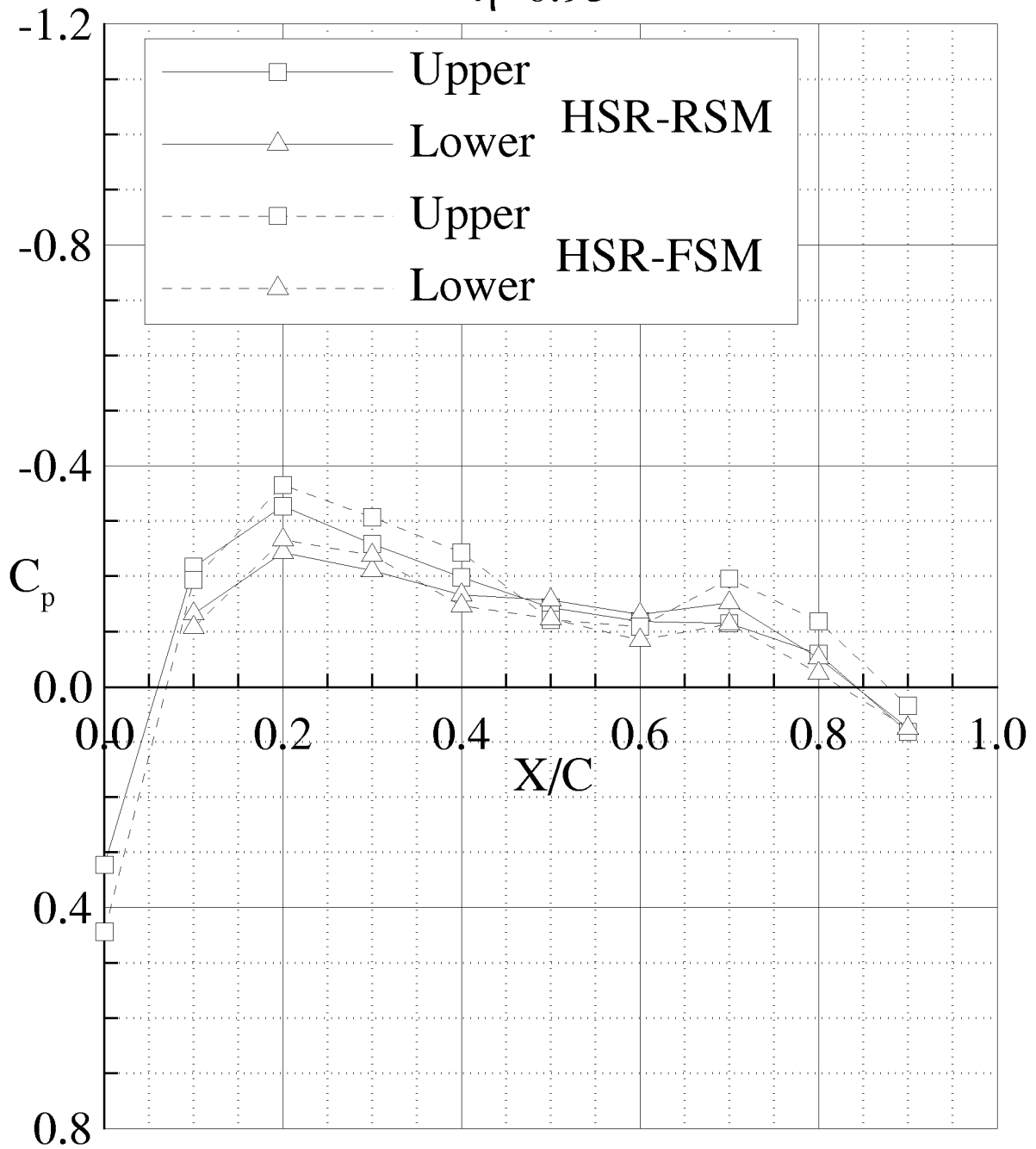


Figure 8-15 (Continued). Comparison of clean wing flexible and rigid pressure distributions at $M=0.95$, $\alpha=2.0^\circ$.

Rigid/Flexible Pressure Distribution

$M=1.15$, $\alpha=2.0^\circ$, $q=150\text{psf}$.

$\eta=0.10$

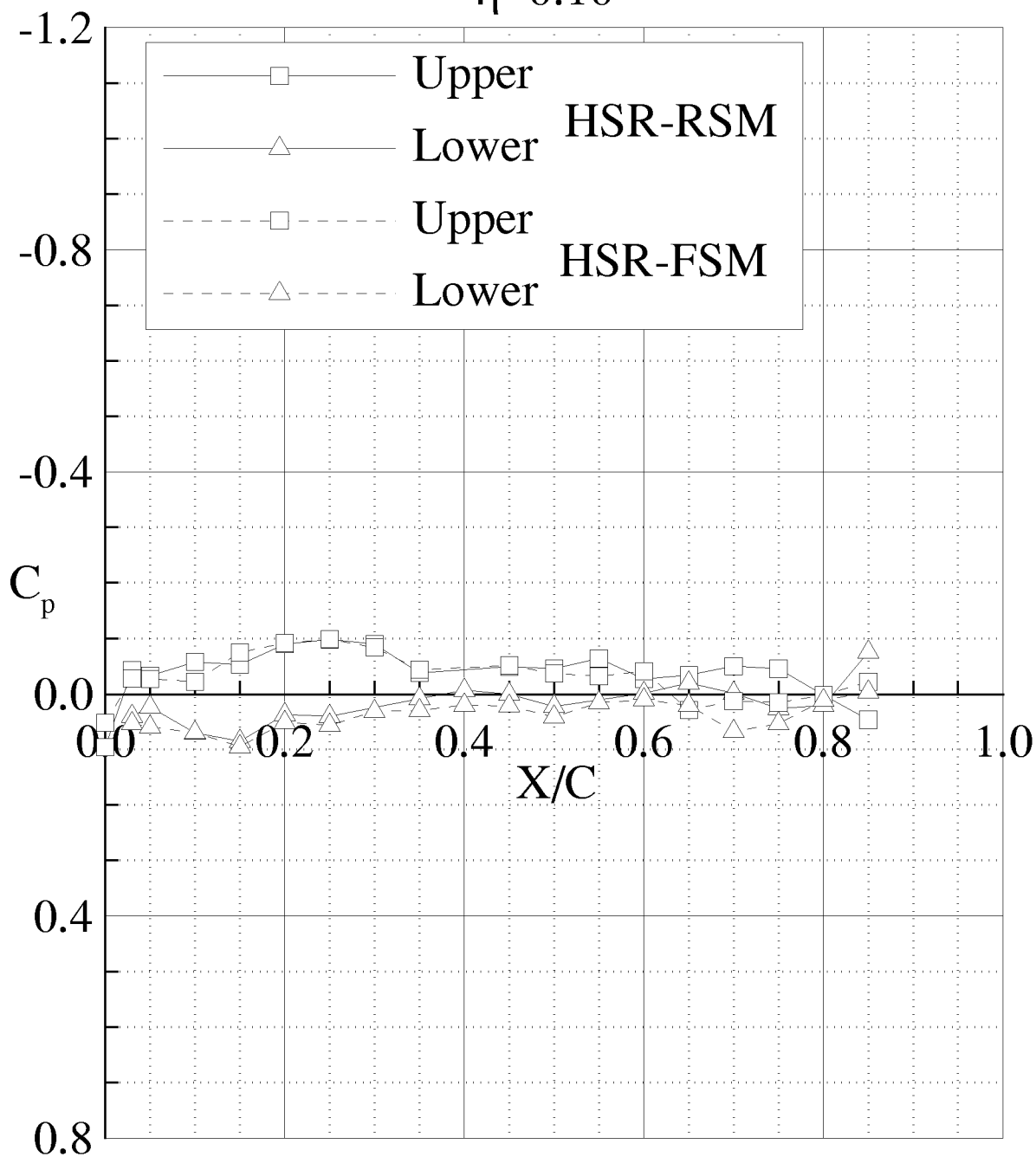


Figure 8-16. Comparison of clean wing flexible and rigid pressure distributions at $M=1.15$, $\alpha=2.0^\circ$.

Rigid/Flexible Pressure Distribution

$M=1.15$, $\alpha=2.0^\circ$, $q=150\text{psf}$.

$\eta=0.30$

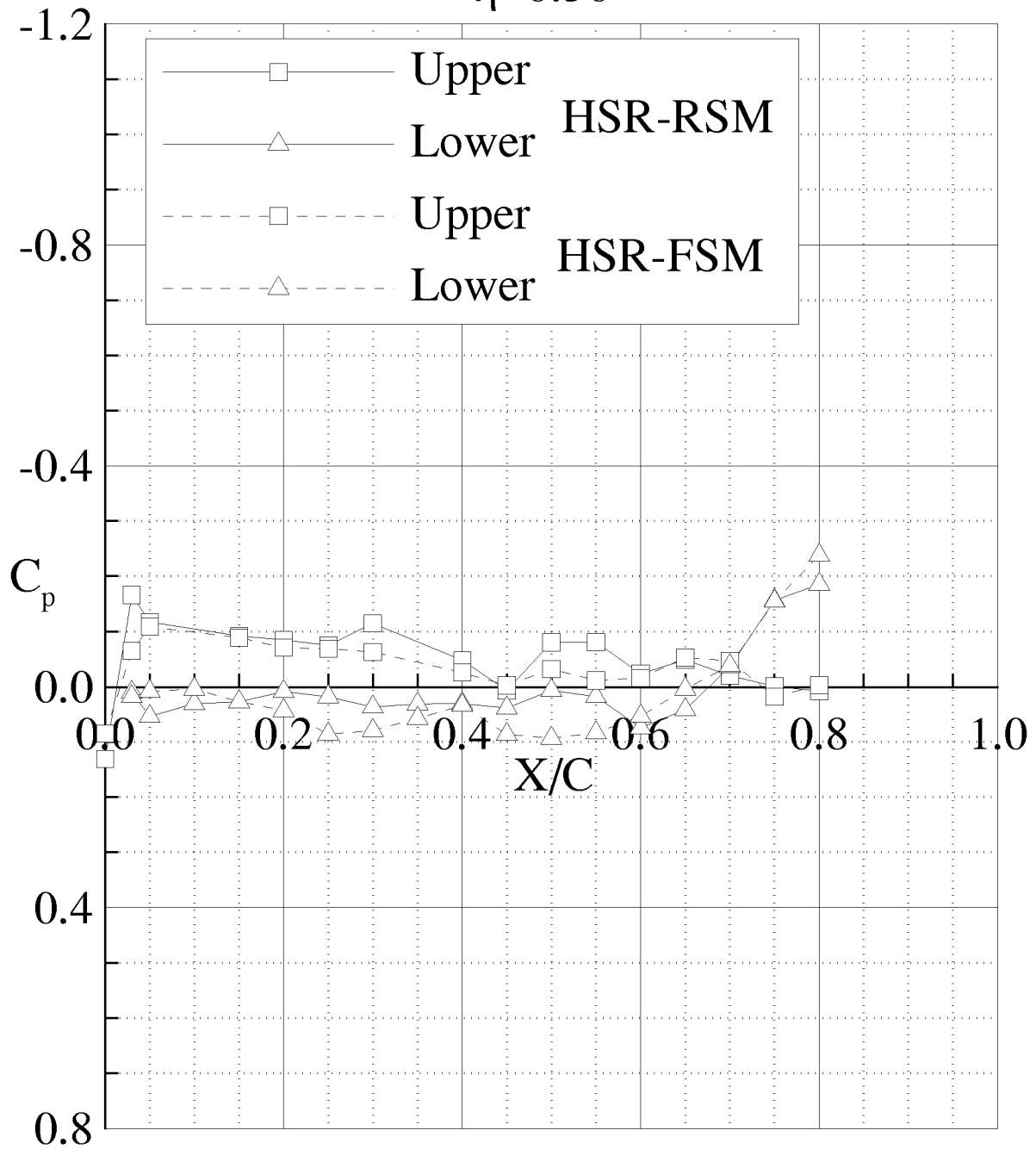


Figure 8-16 (Continued). Comparison of clean wing flexible and rigid pressure distributions at $M=1.15$,

Rigid/Flexible Pressure Distribution

$M=1.15$, $\alpha=2.0^\circ$, $q=150\text{psf}$.

$\eta=0.60$

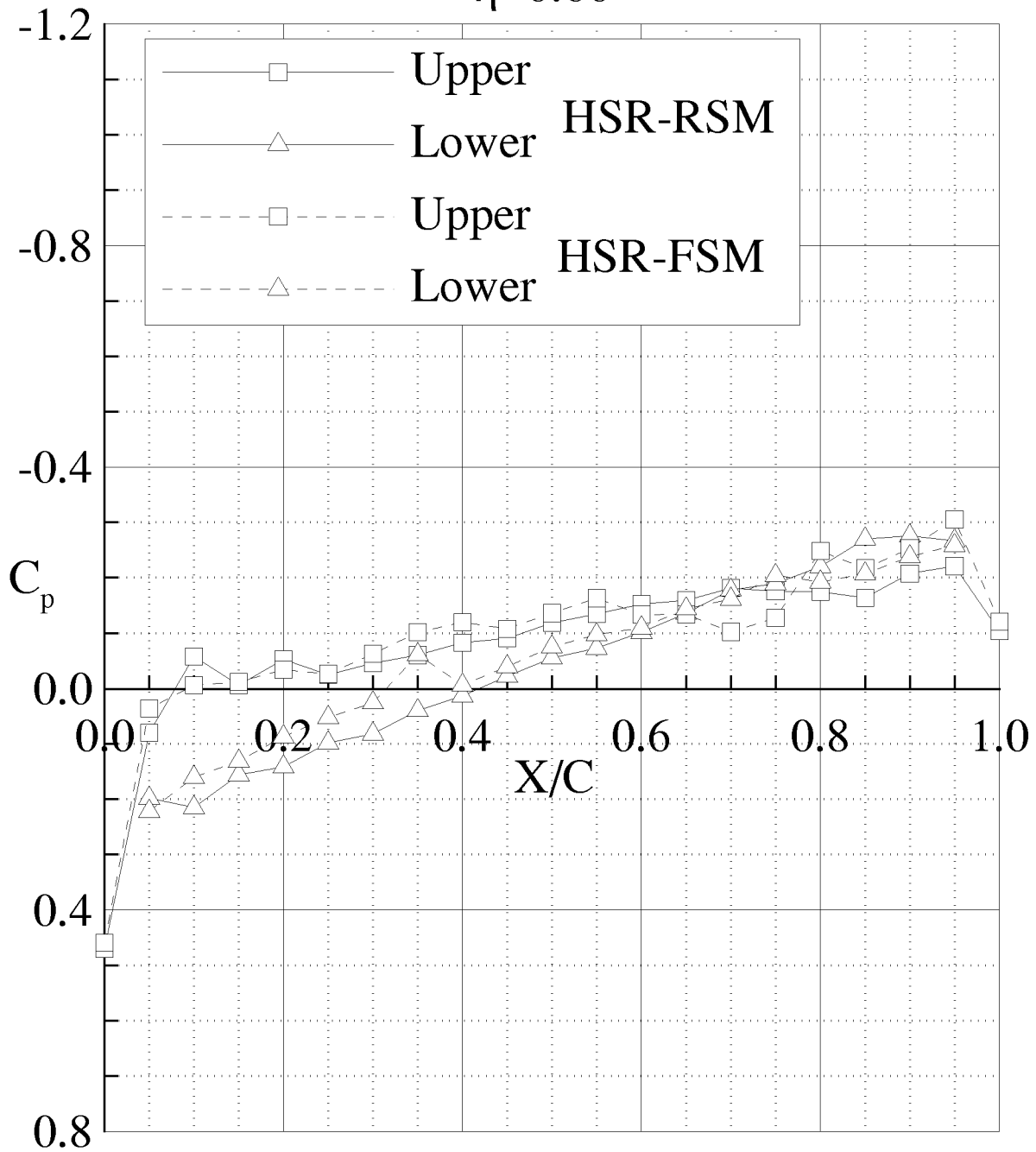


Figure 8-16 (Continued). Comparison of clean wing flexible and rigid pressure distributions at $M=1.15$,

Rigid/Flexible Pressure Distribution

$M=1.15$, $\alpha=2.0^\circ$, $q=150\text{psf}$.

$\eta=0.95$

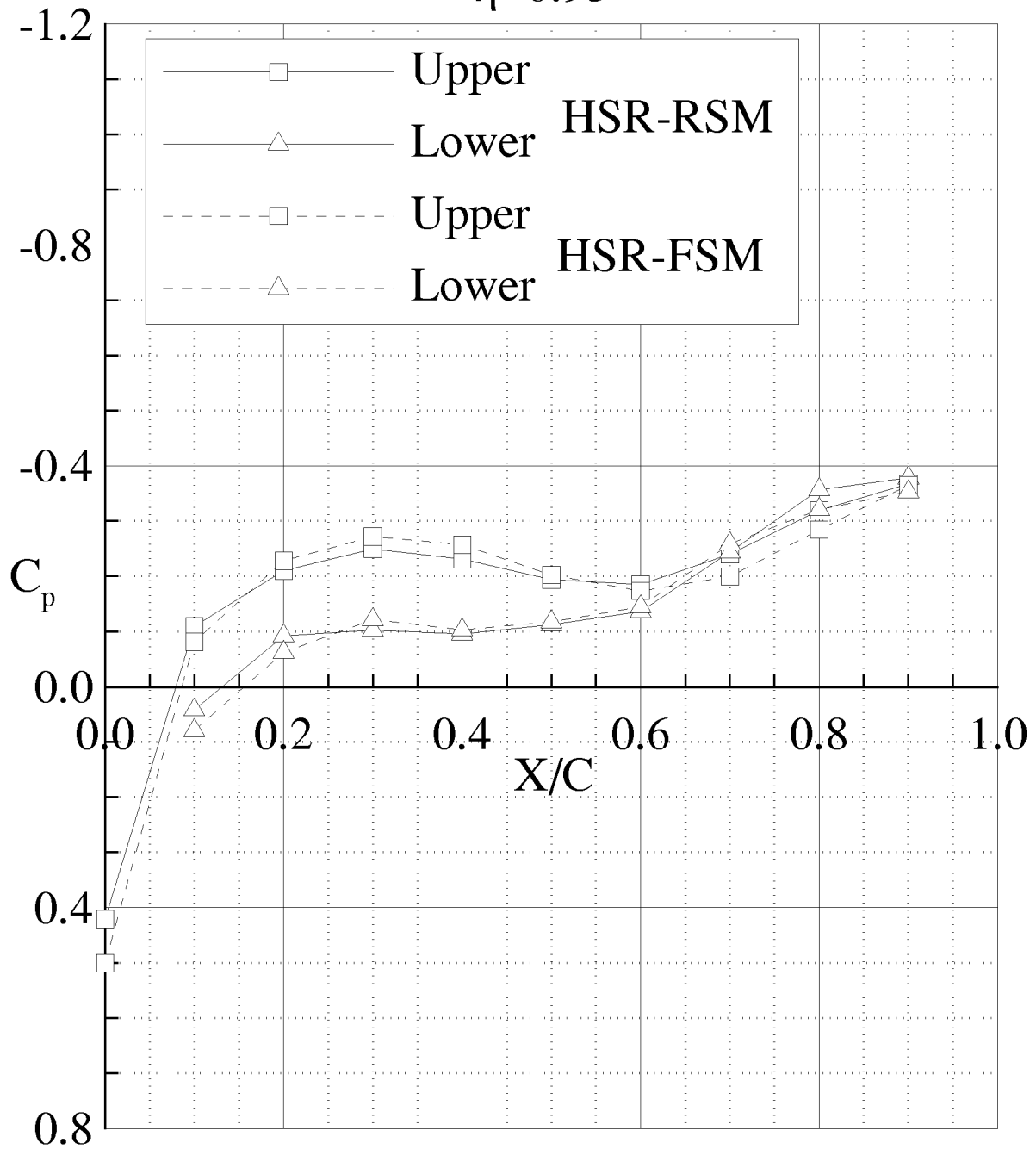


Figure 8-16 (Continued). Comparison of clean wing flexible and rigid pressure distributions at $M=1.15$,

8.4.2 Flexible/Rigid Pressure Comparison with Nacelles On

Flexible and rigid pressure distributions for the wing with nacelles at Mach 0.95, two degrees angle-of-attack, and a dynamic pressure of 150 psf are shown in Figure 8-17. As with the Mach 0.95 clean wing pressure data, the distributions at 10 and 30 percent semispan are very similar for the rigid and flexible wings. This comparison, in conjunction with the previous Mach 0.95 clean wing comparisons, answers several questions concerning the geometric fidelity of the models, and our ability to take consistent aerodynamic data in the TDT. When one considers the amount of instrumentation and the effort required to install and test these models, not to mention the geometric differences that could arise during their construction, it is remarkable that the detailed pressure data is as consistent as it is for these two wings.

At 60% span we again see the effect of flexibility as the lower surface shock is pulled forward for the flexible wing. As with the clean wing data, there is a local flow acceleration at about 80% chord on the wing upper surface which cannot be explained by standard static aeroelastic reasoning. At 95% span, the pressures compare well on the forward portion of the wing section, but significant differences in loading are observed on the aft part of the wing. As with most of the aeroelastic pressure data presented in this report, it is difficult to characterize these changes in the pressure distribution. Further computational aeroelastic analyses of this configuration will likely go a long way toward sorting out the pressure data on the outboard wing.

Rigid/Flexible Pressure Distribution

Nacelles On

$M=0.95$, $\alpha=2.0^\circ$, $q=150\text{psf}$.

$\eta=0.10$

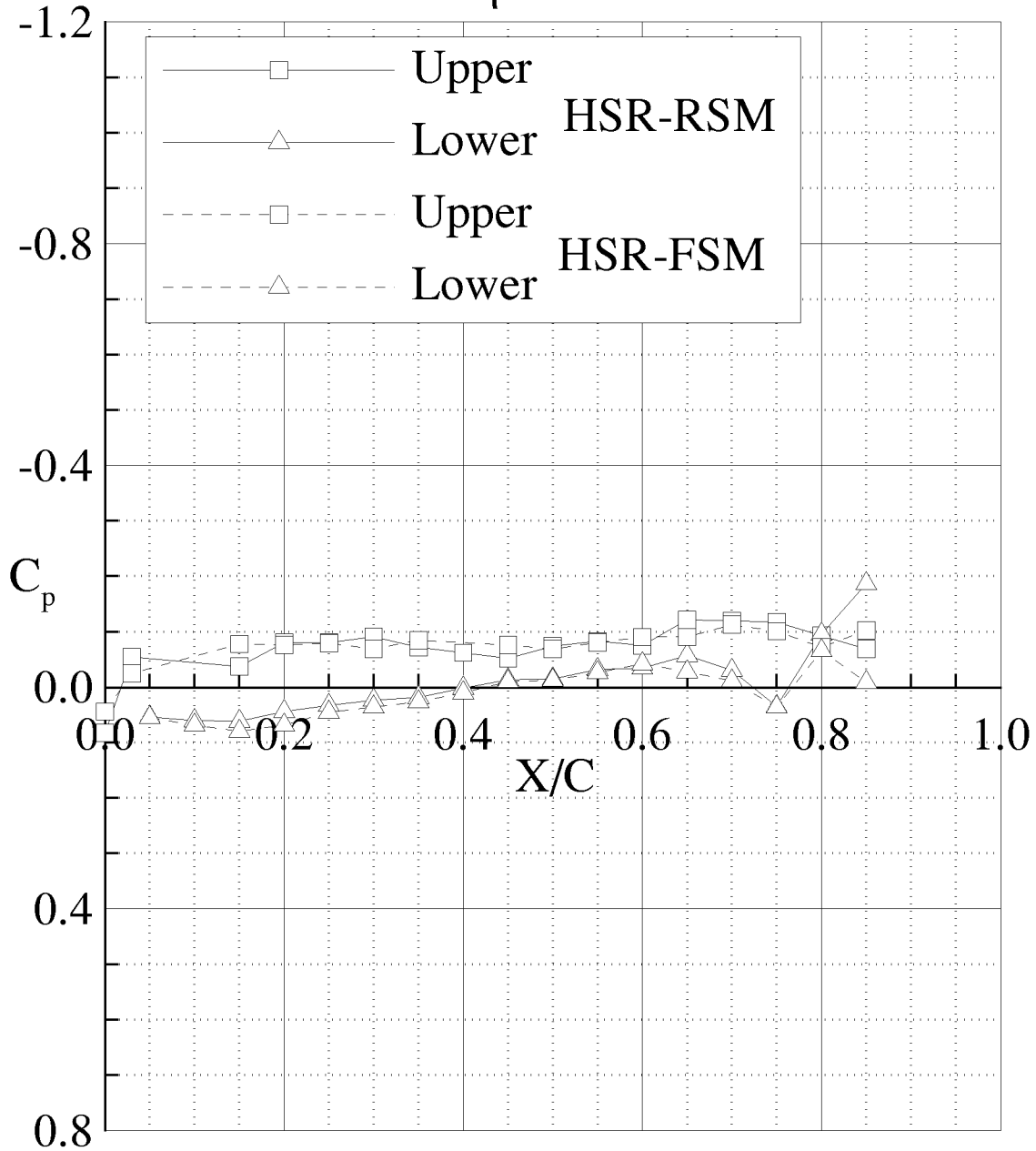


Figure 8-17. Comparison of flexible and rigid pressure distributions for wing with nacelles at $M=0.95$, $\alpha=2.0^\circ$.

Rigid/Flexible Pressure Distribution Nacelles On

$M=0.95$, $\alpha=2.0^\circ$, $q=150\text{psf}$.
 $\eta=0.30$

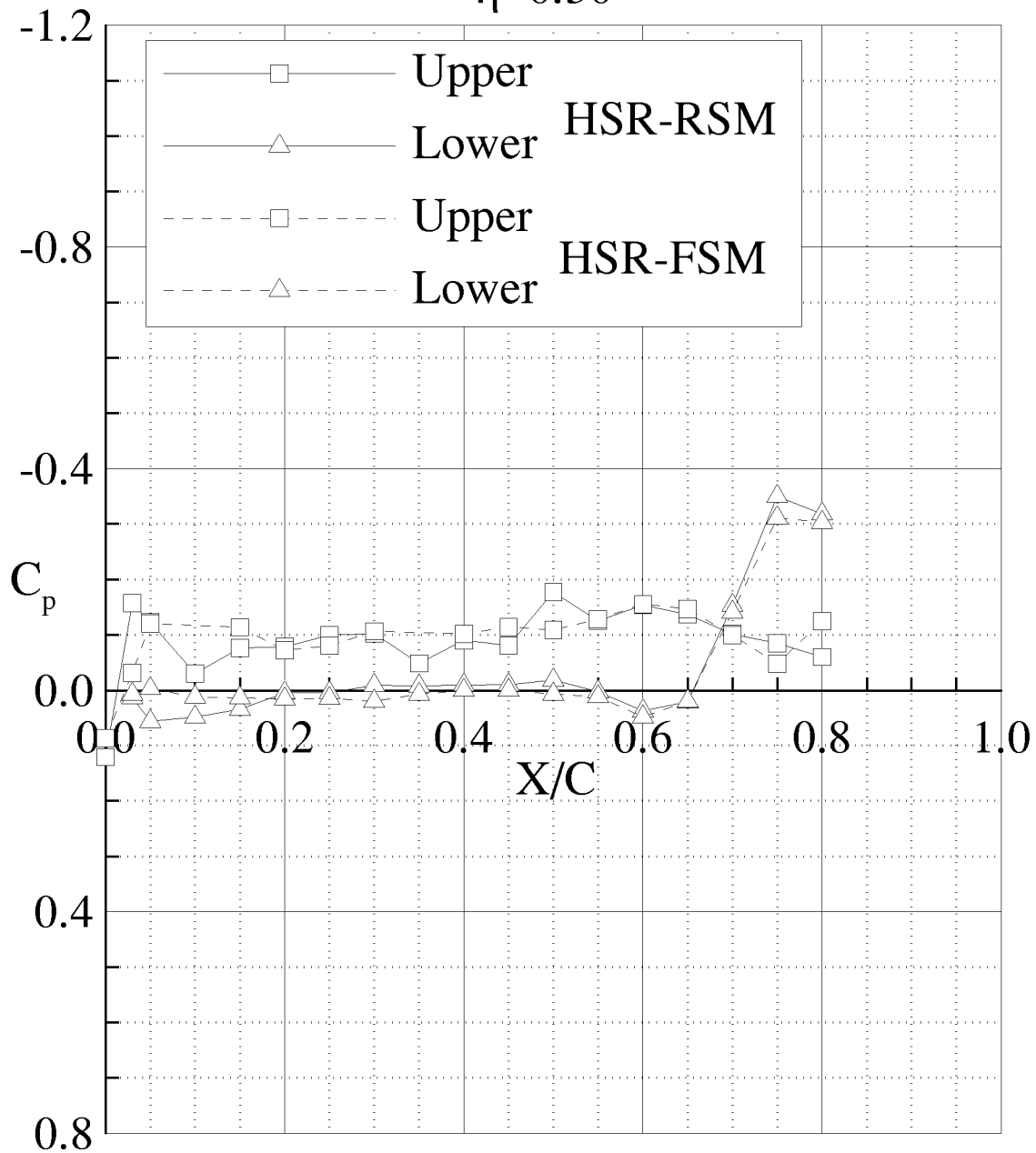


Figure 8-17 (Continued). Comparison of flexible and rigid pressure distributions for wing with nacelles at $M=0.95$, $\alpha=2.0^\circ$.

Rigid/Flexible Pressure Distribution

Nacelles On

$M=0.95$, $\alpha=2.0^\circ$, $q=150\text{psf}$.

$\eta=0.60$

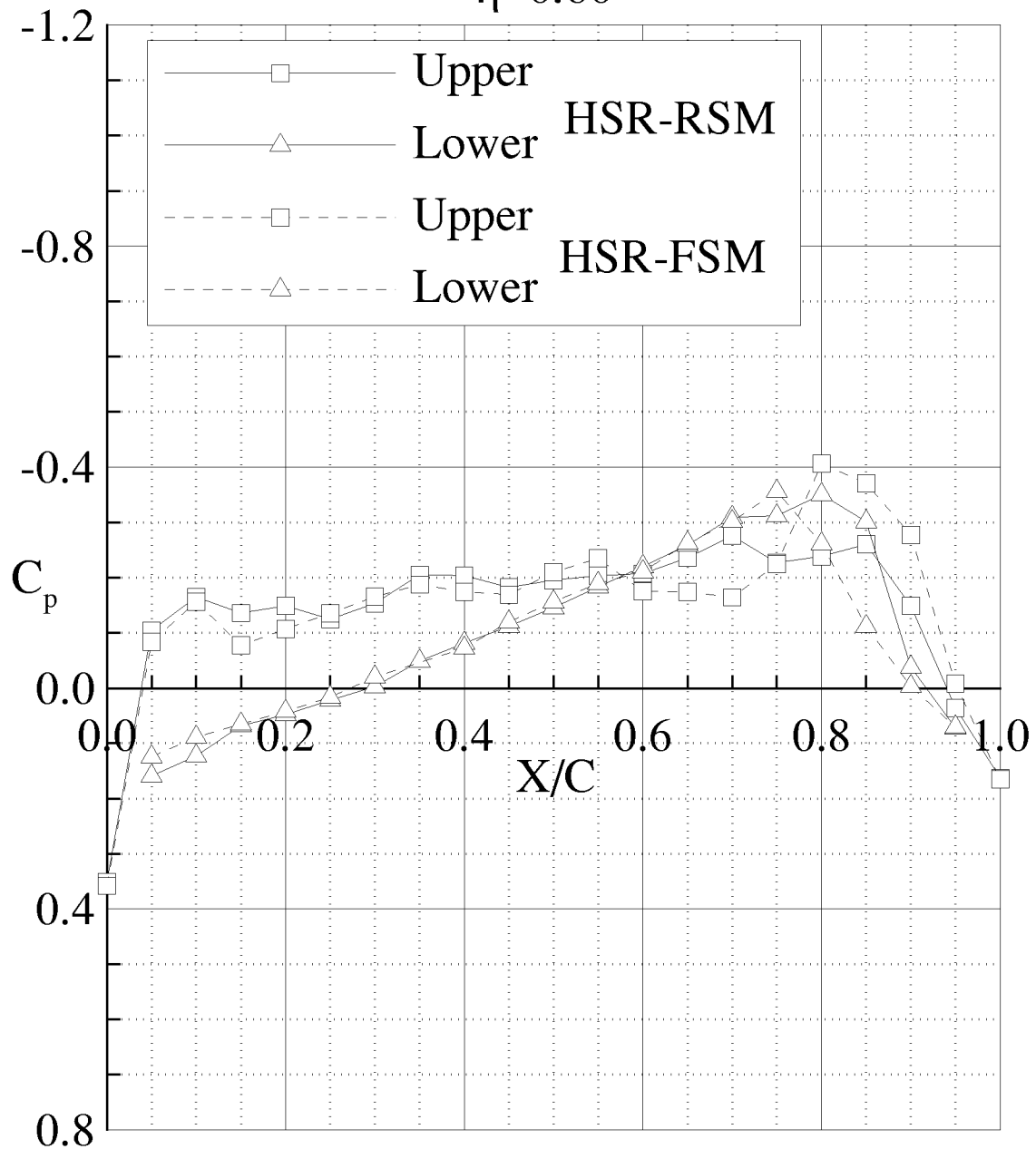


Figure 8-17 (Continued). Comparison of flexible and rigid pressure distributions for wing with nacelles at $M=0.95$, $\alpha=2.0^\circ$.

Rigid/Flexible Pressure Distribution

Nacelles On

$M=0.95$, $\alpha=2.0^\circ$, $q=150\text{psf}$.

$\eta=0.95$

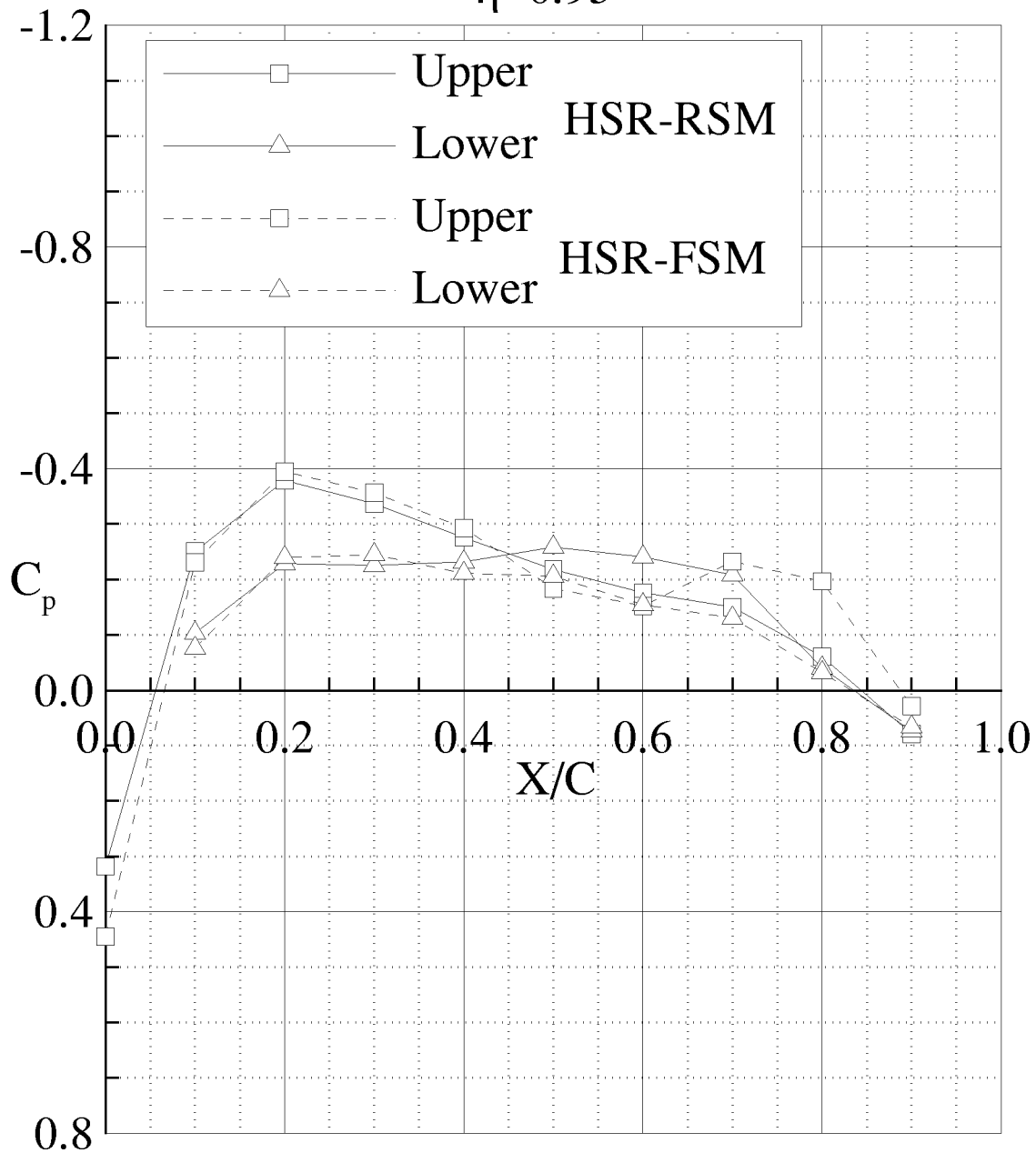


Figure 8-17 (Continued). Comparison of flexible and rigid pressure distributions for wing with nacelles at $M=0.95$, $\alpha=2.0^\circ$.

8.5 Aerodynamic Test Data Summary

In this section, the data were examined for overall consistency and adherence to established aerodynamic and static aeroelastic trends. The variation of the data with angle-of-attack and Mach number has been shown to be reasonable. The lift data is linear with angle-of-attack at low to moderate lift coefficients as are the pitching moment data. The drag is nearly quadratic with lift. Similar aerodynamic characteristics are observed with control surface deflection. The variation of the angle-of-attack polar data with Mach number is somewhat different than that for the rigid wing, as it appears that the structural flexibility tends to reduce the variation in lift curve slope as Mach number is varied. The pitching moment slope varies with Mach number as the center-of-pressure moves aft, but this variation also appears to be reduced for the flexible wing as compared to the rigid wing. Like the rigid wing case, the flap deflection data show a wide range of control surface effectiveness with variation of Mach number due to shock interactions with the control surfaces.

Due to model safety considerations, the dynamic pressures during this experiment were limited to a maximum of 150 psf. Comparisons of 100 psf and 150 psf force data showed only minor differences due to static aeroelasticity. As expected the wing appears to wash out under aerodynamic load as evidenced by a slightly lower flexible wing lift curve slope and a slightly higher pitching moment curve slope at the 150 psf condition.

Comparisons of the rigid and flexible lift and pitching moment curve slopes as a function of Mach number, as well as the drag coefficient at constant lift coefficient as a function of Mach number, provide a great deal of insight into how static aeroelasticity impacts the performance of this wing. Structural flexibility tends to smooth out the variation in the lift and pitching moment slopes that is observed in the rigid model data. Flexibility generally decreases the lift curve slope and increases the pitching moment slope. The impact of flexibility on these components is also noticeably different for subsonic and supersonic flow. The drag coefficient for the flexible wing is reduced at subsonic speeds and is nearly the same as the rigid wing at supersonic speeds. However, these data should be further trimmed for changes in lift and pitching moment before meaningful conclusions can be made concerning the impact of structural flexibility on the performance of the overall vehicle.

It is more difficult to draw quantitative conclusions as to the effect of structural flexibility by comparing rigid and flexible pressure distributions. The angles-of-attack at which pressure data were acquired do not produce enough aerodynamic load to confidently separate aeroelastic effects from scatter in the pressure data. The 60% span station seems to be the most promising station for isolating and studying static aeroelastic effects. At this station, shock movement due to static aeroelasticity can be clearly identified in the transonic data. However, there is also an anomaly in the pressures on the upper surface of the wing which cannot be readily characterized. At 95% span, the flow is highly three-dimensional, and typical aeroelastic behavior for a washout wing is difficult to identify at this station.

The inboard stations on the flexible wing should not deform significantly, and this is verified by excellent agreement between the rigid and flexible pressure distributions at Mach 0.95. These pressure distributions represent data taken from different wind tunnel tests on two geometrically similar models constructed of different materials with drastically different structural properties. Though these comparisons do not present particularly exciting aerodynamic data, they serve as a testament to the hard work and attention to detail that has been expended by everyone involved in this effort.

Comparisons of the supersonic rigid and flexible pressure distributions raise more questions than they answer. It is clear that further analysis of the supersonic pressure data is required before the aerodynamic and structural mechanisms interacting at these conditions can be understood. Expanded computational aeroelastic analyses at both transonic and supersonic speeds could prove to be very valuable in analyzing the flow about the HSR-FSM.

9.0 Conclusions and Recommendations

The following discussion highlights the major points of interest for the analytical model development, aerodynamics and flutter phases of the test program. Lessons learned and recommendations are included.

9.1 Finite Element Modeling and Pretest Experiments and Analyses

Because of the planned TDT shut down and a mishap leading to reconstruction of the HSR Rigid Semispan Model, there was very little time to do as thorough a job as desired in many of the pretest activities. Hopefully, in future programs, more realistic allowances of manpower and time along with more flexibility in the TDT schedule will be possible. Following is a list of specific recommendations based on the FSM experience.

- a. Where composite materials are involved, develop strategies for accurately determining the effective dynamic stiffnesses as opposed to relying on conventional material coupon tests. Where possible, test structural components for stiffness prior to assembling with other components.
- b. During model fabrication, document the weight and specific location of any material or items added or removed from the model and reweigh and determine the center of gravity for the entire model when any change is made.
- c. Constantly maintain a finite element model which corresponds directly, and as accurately as possible, with the physical model in fabrication.
- d. Afford pre-tunnel testing (static loads, vibration etc.) the same priority as fabrication and wind-tunnel testing. Correlate test and analysis data, and resolve unexplained differences prior to dismantling test fixtures. Thoroughly model and test all supporting structures (stings, balances, turntables etc.) and investigate structural boundary conditions.

9.2 Aerodynamics

Transonic Dynamics Tunnel Test 521 of the HSR Flexible Semispan Model has provided a supplemental set of high quality force and pressure measurements for use in conjunction with the data taken on the HSR Rigid Semispan Model during TDT Test 520. Both of these data sets should prove invaluable in the validation of steady and unsteady computational aeroelasticity methods. Pressure and force data were acquired for a structurally flexible clean wing and wing with nacelles, as well as unsteady aeroelastic data excited by oscillating the control surfaces. Unsteady aeroelastic pressure data near the wing's flutter boundary were also collected, and the primary objectives of the test were met. From a CFD code correlation standpoint, detailed wing and fuselage pressure data were acquired which can be compared directly with pressure distributions computed by CFD analyses. Loads data from a five component force balance were acquired for each set of pressure distributions so that integrated CFD loads can be compared with accurately measured experimental loads. The test setup was carefully configured to isolate the wing loads from the fuselage load so that the highly nonlinear flow about the fuselage/wind tunnel wall combination would not complicate the process of comparing the experimental loads with the more idealistic loads computed by CFD methods. Even with these precautions, one should be careful to

consider the influence of the wind tunnel walls and blockage when comparing these data with analytical results. In particular, the build up of the boundary layer on the sidewall of the tunnel should be examined and an assessment of its impact on the experimental data should be formulated. Since the model was not tested with a splitter plate, the boundary layer along TDT east wall could have had a significant impact on the aerodynamic data.

Each data point acquired in the TDT represents a unique set of flow conditions and configuration. The loads data were reduced and organized into typical aerodynamic polar form following the test. The lift and moment curves were approximated using a linear least squares fit, and the drag as a function of lift was fit using a second order curve. Parameters such as lift curve slope, minimum drag, etc. can be extracted from these curve fits. Higher order fits of the data were also investigated, but these fits produced less consistent data when certain parameters such as lift curve slope were plotted against Mach number. All of the loads data were tabulated, plotted, written to a CD-ROM volume and distributed to the HSR industry partners.

Unsteady wing pressure data and steady fuselage pressure data were acquired, reduced, written in tabular form and plotted on-line during the test. The tabular pressure data and plots have also been accumulated into a CD-ROM volume and distributed. The tabulated data were written in an ASCII formatted channel statistics file which can be easily read and post processed. The steady fuselage pressure data are organized into rows of pressures along constant fuselage sections, while the wing pressures are organized into chordwise rows at four constant span stations. In addition to time averaged wing pressures, unsteady pressure measurements were also made for cases where the trailing edge control surface was oscillated. ASCII files of these time histories were included in the previously delivered data package.

The primary objective of this test was to acquire static and dynamic aeroelastic data for use in validating advanced aeroelastic analysis methods. The force and pressure data presented in this document verify that this objective has been met. However, the data presented here has much greater potential for application than simply code validation. A number of challenging issues were raised that very likely can only be solved through a synergistic application of theoretical and experimental analyses. As for the HSR-RSM, there is great potential for computational methods to be used to assist in resolving discrepancies and providing physical insight into many of the aeroelastic characteristics observed during this test. The HSR-FSM is an extremely complex three-dimensional aerodynamic surface that challenges the conventional interpretation of the experimental data. Computational methods are well-positioned for assisting us in the interpretation of these data, and they should be employed in this role, not simply in the context of code validation and calibration. A more thorough understanding of the aerodynamic and aeroelastic phenomena present on this wing will prove invaluable in the analysis and evaluation of future high speed transport concepts.

Finally, the impact of static aeroelastic effects on the aerodynamic performance of this vehicle should not be overlooked. The experimental loads data presented in this report indicate that static aeroelasticity significantly affects the aerodynamic forces and moments on this wing. At subsonic speeds, aeroelastic deflection of the FSM reduces the wing's untrimmed drag at constant lift coefficient as compared to the rigid wing. This characteristic could be exploited in the full-scale vehicle design to improve aerodynamic performance in this flight regime. These experimental results serve as an excellent springboard for further computational and experimental studies of the impact of static aeroelasticity on the aerodynamic performance of HSR concepts.

9.3 Flutter

Although the FSM was destroyed by transonic flutter, the test produced significant worthwhile data which could well serve the HSR program. Wind-tunnel data (including force, pressure and dynamic response) indicate a narrow Mach number range around 0.98 in which the wing clearly exhibits transonic flow. That is, there is evidence of shocks, buffet, or other nonlinear phenomenon in this range. Mach 0.98 is where the model was destroyed due to flutter. The only other flutter point (except for a case where the trailing edge was loose), was identified at Mach 0.945.

Unfortunately, subsonic flutter points could not be obtained. The pretest linear flutter analysis predicted subsonic flutter at conditions substantially lower in q than those shown flutter free in the test. Post-test analysis, updated with experimental frequencies and damping, indicate that the flutter mechanism is a weak hump mode which grows weaker and disappears at lower Mach numbers. In that sense, it may be consistent with what was observed in the TDT. With the ready availability of the FSM data and models, it may prove worthwhile to perform a higher-order nonlinear flutter analysis for comparison with the transonic flutter results.

The FSM test was performed to obtain steady and unsteady aerodynamic pressures as well as loads, static aeroelasticity and flutter data. The wing contained a great deal of instrumentation including tubing, wires and skin pressure orifices and transducers. A fuselage-like structure was mounted on a strut and balance system which was in turn mounted to a retractable turntable. The effects of the fuselage (aerodynamic and structural) and mounting system (structural) on flutter were never fully understood. For the purpose of correlating experimental and analytical flutter for semispan models, success is more likely when a splitter plate and a simple, very rigid mounting arrangement are used. Unfortunately, given the program objectives, schedule and the inherent risk of flutter testing, this was not practical as a first step for the FSM. For future activities, it is recommended that the HSR team carefully consider costs and benefits for developing separate but simpler models for specific objectives.

In order to proceed with an FSM-like program, it is often necessary to assume early in the design phase that certain unknowns or potential problems will be resolved in due time. However, in the case of the FSM, we were often very late in dealing with these issues which in turn led to less than desirable resolutions. For example, it was assumed that the HSR Rigid Semispan Model (RSM) design could be re-scaled in stiffness and mass to allow flutter in the TDT. This turned out to be extremely difficult because, for the FSM, the stressed-skin concept required skin material properties that may not exist. If adequate materials do exist, we did not identify them. Where stressed-skin designs are required, as opposed to a design which carries loads through internal beam or plate-like structural members, careful study of available skin materials should be conducted early in the program. This involves understanding the “dynamic” moduli and nonlinear characteristics of the material, and not assuming that published properties or traditional coupon test data are sufficient for flutter model construction.

10.0 References

1. Lahey, R.S.; Miller, M. P. and Reymond, M.: “MSC/NASTRAN Reference Manual, Version 68,” The MacNeal-Schwendler Corporation, 1994.
2. Structural Dynamics Research Corp.: “Exploring I-DEAS Test” I-DEAS Master Series, Release 2, 1994
3. Batina, J. T.: “Efficient Algorithm for Solution of the Unsteady Transonic Small-Disturbance Equation,” *Journal of Aircraft*, vol. 25, pp. 598—605, July 1988.
4. Adams, William M. Jr.; Tiffany, Sherwood H.; Newsom, Jerry R.; Peele, Ellwood L.: “STABCAR—A Program for Finding Characteristic Roots of Systems Having Transcendental Stability Matrices”, NASA TP 2165, June, 1984.

REPORT DOCUMENTATION PAGE			Form Approved OMB No. 07704-0188	
Public reporting burden for this collection of information is estimated to average 1 hour per response, including the time for reviewing instructions, searching existing data sources, gathering and maintaining the data needed, and completing and reviewing the collection of information. Send comments regarding this burden estimate or any other aspect of this collection of information, including suggestions for reducing this burden, to Washington Headquarters Services, Directorate for Information Operations and Reports, 1215 Jefferson Davis Highway, Suite 1204, Arlington, VA 22202-4302, and to the Office of Management and Budget, Paperwork Reduction Project (0704-0188), Washington, DC 20503.				
1. AGENCY USE ONLY (Leave blank)	2. REPORT DATE September 1999	3. REPORT TYPE AND DATES COVERED Contractor Report		
4. TITLE AND SUBTITLE Development, Analysis and Testing of the High Speed Research Flexible Semispan Model		5. FUNDING NUMBERS 537-06-36-20 NAS1-96014		
6. AUTHOR(S) David M. Schuster, Charles V. Spain, David L. Turnock, Russ D. Rausch, M-Nabil Hamouda, William A. Vogler, Alan E. Stockwell				
7. PERFORMING ORGANIZATION NAME(S) AND ADDRESS(ES) Lockheed Martin Engineering and Sciences Mail Stop 371 Hampton, VA 23681-2199		8. PERFORMING ORGANIZATION REPORT NUMBER		
9. SPONSORING/MONITORING AGENCY NAME(S) AND ADDRESS(ES) National Aeronautics and Space Administration Langley Research Center Hampton, VA 23681-2199		10. SPONSORING/MONITORING AGENCY REPORT NUMBER NASA/CR-1999-209556		
11. SUPPLEMENTARY NOTES Langley Technical Monitor: Thomas E. Noll				
12a. DISTRIBUTION/AVAILABILITY STATEMENT Unclassified-Unlimited Subject Category 02 Availability: NASA CASI (301) 621-0390		12b. DISTRIBUTION CODE		
13. ABSTRACT (Maximum 200 words) This report presents the work performed by Lockheed Martin Engineering and Sciences (LMES) in support of the High Speed Research (HSR) Flexible Semispan Model (FSM) wind-tunnel test. The test was conducted in order to assess the aerodynamic and aeroelastic character of a flexible high speed civil transport wing. Data was acquired for the purpose of code validation and trend evaluation for this type of wing. The report describes a number of activities in preparing for and conducting the wind-tunnel test. These included coordination of the design and fabrication, development of analytical models, analysis/hardware correlation, performance of laboratory tests, monitoring of model safety issues, and wind-tunnel data acquisition and reduction. Descriptions and relevant evaluations associated with the pretest data are given in sections 1 through 6, followed by pre- and post-test flutter analysis in section 7, and the results of the aerodynamics/loads test in section 8. Finally, section 9 provides some recommendations based on lessons learned throughout the FSM program				
14. SUBJECT TERMS Aerodynamic characteristics; Supersonic transport; Aircraft stability and control; Aeroelasticity			15. NUMBER OF PAGES 123	
			16. PRICE CODE A06	
17. SECURITY CLASSIFICATION OF REPORT Unclassified	18. SECURITY CLASSIFICATION OF THIS PAGE Unclassified	19. SECURITY CLASSIFICATION OF ABSTRACT Unclassified	20. LIMITATION OF ABSTRACT UL	